UCLA
UCLA Electronic Theses and Dissertations

Title
Equilibrium & Nonequilibrium Fluctuation Effects in Biopolymer Networks

Permalink
https://escholarship.org/uc/item/6v400993

Author
Kachan, Devin

Publication Date
2014

Peer reviewed|Thesis/dissertation

eScholarship.org Powered by the California Digital Library
University of California

University of California

Los Angeles

Equilibrium & Nonequilibrium Fluctuation Effects in Biopolymer Networks

A dissertation submitted in partial satisfaction

of the requirements for the degree

Doctor of Philosophy in Physics

by

Devin Michael Kachan

2014

© Copyright by
Devin Michael Kachan
2014

Abstract of the Dissertation

Equilibrium & Nonequilibrium Fluctuation Effects in Biopolymer Networks

by

Devin Michael Kachan

Doctor of Philosophy in Physics

University of California, Los Angeles, 2014

Professor Alexander Levine, Chair

Fluctuation-induced interactions are an important organizing principle in a variety of soft matter systems. In this dissertation, I explore the role of both thermal and active fluctuations within cross-linked polymer networks. The systems I study are in large part inspired by the amazing physics found within the cytoskeleton of eukaryotic cells. I first predict and verify the existence of a thermal Casimir force between cross-linkers bound to a semi-flexible polymer. The calculation is complicated by the appearance of second order derivatives in the bending Hamiltonian for such polymers, which requires a careful evaluation of the the path integral formulation of the partition function in order to arrive at the physically correct continuum limit and properly address ultraviolet divergences. I find that cross linkers interact along a filament with an attractive logarithmic potential proportional to thermal energy. The proportionality constant depends on whether and how the cross linkers constrain the relative angle between the two filaments to which they are bound.

The interaction has important implications for the synthesis of biopolymer bundles within cells. I model the cross-linkers as existing in two phases: bound to the bundle and free in solution. When the cross-linkers are bound, they behave as a one-dimensional gas of particles interacting with the Casimir force, while the

free phase is a simple ideal gas. Demanding equilibrium between the two phases, I find a discontinuous transition between a sparsely and a densely bound bundle. This discontinuous *condensation* transition induced by the long-ranged nature of the Casimir interaction allows for a similarly abrupt structural transition in semiflexible filament networks between a low cross linker density isotropic phase and a higher cross link density bundle network. This work is supported by the results of finite element Brownian dynamics simulations of semiflexible filaments and transient cross linkers. I speculate that cells take advantage of this equilibrium effect by tuning near the transition point, where small changes in free cross-linker density will affect large structural rearrangements between free filament networks and networks of bundles.

Cells are naturally found far from equilibrium, where the active influx of energy from ATP consumption controls the dynamics. Motor proteins actively generate forces within biopolymer networks, and one may ask how these differ from the random stresses characteristic of equilibrium fluctuations. Besides the trivial observation that the magnitude is independent of temperature, I find that the processive nature of the motors creates a temporally correlated, or *colored*, noise spectrum. I model the network with a nonlinear scalar elastic theory in the presence of active driving, and study the long distance and large scale properties of the system with renormalization group techniques. I find that there is a new critical point associated with diverging correlation time, and that the colored noise produces novel frequency dependence in the renormalized transport coefficients.

Finally, I study marginally elastic solids which have vanishing shear modulus due to the presence of *soft modes*, modes with zero deformation cost. Although network coordination is a useful metric for determining the mechanical response of random spring networks in mechanical equilibrium, it is insufficient for describing networks under external stress. In particular, under-constrained networks which are fluid-like at zero load will dynamically stiffen at a critical strain, as observed in

numerical simulations and experimentally in many biopolymer networks. Drawing upon analogies to the stress induced unjamming of emulsions, I develop a kinetic theory to explain the rigidity transition in spring and filament networks. Describing the dynamic evolution of non-affine deformation via a simple mechanistic picture, I recover the emergent nonlinear strain-stiffening behavior and compare this behavior to the yield stress flow seen in soft glassy fluids. I extend this theory to account for coordination number inhomogeneities and predict a breakdown of universal scaling near the critical point at sufficiently high disorder, and discuss the utility for this type of model in describing biopolymer networks.

The dissertation of Devin Michael Kachan is approved.

Robijn Bruinsma

Dolores Bozovic

William Gelbart

Alexander Levine, Committee Chair

University of California, Los Angeles

2014

To my mother

Table of Contents

List of Figures

Acknowledgments

I would like to thank my advisor for his constant guidance, relaxed nature, and most importantly for the vast array of knowledge he imparted during my time at UCLA. I am fortunate to have been awarded the GMF to continue our work. Fight on.

Thank you Christian for choosing to be a physicist. The office might have been uninhabitable otherwise, and I probably would have given up without the daily jokes, banter, and genuine interest in the mathematical description of the world around us.

To Art, thank you for being an authentic scientist in a sea of imposters, reminding me of why I left the midwest, and of course for introducing me to the conservatory.

I must finally thank Jenny for encouraging me to take the Comp when it looked like all was lost...I made it through and I owe that to you.

Chapter 2 is a partial reprint of material as it appears in Phys. Rev. E 2013, D. Kachan, R. Bruinsma, and A. J. Levine 2013, as well as material currently in submission. The dissertation author was the primary author on both of these publications.

Chapter 3 and 4 are, in part, material in submission and preparation for submission. The dissertation author was the primary author of this material.

Vita

2009	B.S. in Physics *magna cum laude* University of Southern California Los Angeles, California
2009-2014	Graduate Teaching Assistant University of California, Los Angeles

Publications

D. Kachan, R. Bruinsma, and A. J. Levine, *Casimir interactions in semiflexible polymers*, Phys. Rev. E, **87** , 032719, 2013.

D. Kachan, K. W. Müller, W. A. Wall, and A. J. Levine, *Discontinuous bundling transition in semiflexible polymer networks induced by Casimir interactions*, submitted.

D. Kachan, A. A. Evans *Kinetic Theory for the Rigidity Transition in Floppy Networks and the Correspondence to Jammed Emulsions*, submitted.

CHAPTER 1

Introduction

This thesis concerns both the equilibrium and non equilibrium properties of cross linked semi-flexible polymer networks, a class of soft matter system. In order to properly pose the research question, it is necessary to briefly describe the distinguishing features of soft condensed matter so as to illustrate where my research fits within this broader scope. The introduction is organized as follows: I will first discuss soft matter systems, with a focus on the forces and energy scales that are generally relevant to a physical description. Polymers and networks of polymers will be introduced along the way, with brief sections on their elasticity and ease with which their non-equilibrium states may be explored. I will then describe the often overlooked fluctuation or *Casimir* forces and review their importance within nematic liquid crystals, as well as propose their existence and role in cross linked polymer networks. Finally, as physics is an experimental science, I will introduce the cytoskeleton as an accessible realization of the physics I study.

1.1 Soft matter physics

Soft matter physics is quite literally the study of squishy matter. More precisely, it is concerned with systems governed by weak energy scales relative to the covalent bond energies typically found in hard matter systems. This means that while hard matter systems tend to be quite exotic, many household items constitute interesting soft matter systems. The mayonnaise on your sandwich and whipped cream on your ice-cream sundae are respectively examples of emulsions and foams,

both of which are active fields of research. A more progressive culinary student may be familiar with the spherification technique, where droplets of liquid, such as orange juice, are stabilized and made to resemble caviar. The process, and it's cousin reverse-spherification, relies on the formation of a calcium ion cross-linked polymer network of sodium alginate around the droplets and is a realization of the class of systems I will study in this thesis.

Soft matter physics is also ubiquitous in the study of biological systems, a point which will be discussed in more detail in Sec. 1.2. The typical cellular length scale puts many interaction energies on the order of $k_{\mathrm{B}}T$, where k_{B} is Boltzmann's constant, so that thermal fluctuations must be considered in any description. Cellular systems thus offer the soft matter physicist an opportunity to borrow mathematically from results in quantum mechanics. The analogy, although purely formal, is still of considerable interest.

The building blocks of soft matter systems include colloids, liquid crystals, polymers, and membranes, to name a few. The fundamental forces between these constituents are fairly weak when compared to their hard matter counterparts and tend to be short ranged. Electrically charged colloids in water, for example, experience a strongly screened Coulomb interaction which is only on the order of $k_{\mathrm{B}}T$, allowing competition with entropy. In the absence of a stabilizing charge the colloids will aggregate due to very short ranged Van der Waals forces which are balanced by even shorter range steric repulsion. Membranes and polymers earn the soft classification in a slightly different sense than colloids: they are *elastic*, meaning that the characteristic energy scale of excitations vanishes as the system grows. In other words, thermal fluctuations are able to excite long wavelength modes with appreciable amplitude for sufficiently large systems. In addition to elasticity, hydrodynamic couplings are often present in soft matter systems.

1.1.1 Polymers

Polymers are the main actor in this thesis and require a sufficient introduction. First, a definition: A polymer is a macromolecule composed of repeating subunits known as monomers. Polymers occur naturally in biological systems (see Sec. 1.2), and are also easily synthesized and used extensively in industrial applications. Although exotic branched configurations involving different monomers exist and are easily synthesized, I will restrict my attention to simple single monomer linear chains whose length is many times the monomer size. In this limit the chemical details of the underlying monomer cease to matter and the polymer may be modeled as a continuum object. The simplest model is the so called freely jointed or ideal chain, which ignores all bending and stretching by describing the polymer as a chain of N independent rigid rods of length l. The assumption of independent chain segments associates l with the contour length over which the chain loses orientational order. Typical values of l vary greatly between a few monomers to over a thousand, reflecting the great diversity of monomeric building blocks. Mathematically the ideal chain is equivalent to a random walk with N steps of size l and this gives the predicted scaling $R \sim \sqrt{N}l$ for the typical size of the polymer.

The ideal chain is of course an unrealistic model: Changes in orientation introduce strain into the polymer which tends to subsequently relax due to internal stresses. The simplest extension incorporating elasticity is the worm like chain model, which considers the polymer as a thin, inextensible elastic rod with bending modulus κ. The assumption of incompressibility is appropriate for most polymers because the underlying monomers are much more compliant to axial rotation than to longitudinal stretching. The bending energy of a particular chain configuration is given by

$$E = \frac{\kappa}{2} \int \mathrm{d}s \left(\frac{\mathrm{d}\hat{t}}{\mathrm{d}s} \right)^2 , \tag{1.1}$$

where $\hat{t}$ is the local tangent vector and the integral is taken along the contour length of the polymer [RC03, DE86]. The derivative $\left|\frac{\mathrm{d}\hat{t}}{\mathrm{d}s}\right|$ is simply $1/R$, where R is the local radius of curvature. The ground state configuration is perfectly straight and one may wonder how this could ever describe the highly unordered states predicted by the ideal chain. The resolution is that these systems are observed at finite temperature and, depending on the modulus κ, thermal fluctuations can severely distort the chain. A quantitative measure of orientational order at finite temperature is given by the tangent vector autocorrelation function $\langle \hat{t}(0) \cdot \hat{t}(x) \rangle$, which one can easily show is an exponentially decaying function within the worm-like chain model. The characteristic decay length, known as the persistence length, is $l_p = \beta\kappa$, where $\beta = 1/k_{\mathrm{B}}T$. This persistence length intuitively diverges at zero temperature when the polymer is expected to be straight, and grows with increasing chain stiffness. It furthermore neatly classifies polymers at a given temperature: Short polymers ($L < l_p$) are typically straight and are referred to as semi-flexible, while long polymers ($L < l_p$) are very flexible and are appropriately modeled as ideal chains. In fact, an ideal chain with segment length $l = 2l_p$ (known as the Kuhn length) will display the exact same end to end statistics as a worm-like chain of persistence length l_p.

It is reasonable to ask how the persistence length of a thin rod is related to its cross sectional dimension, and to see if these numbers allow for both flexible and semi-flexible polymers at room temperature. The bending modulus of a rod is given by $\kappa = EI$, where E is the Young's modulus and I is the area moment of inertia [LL86]. The Young's modulus has units of an energy density and since the modulus is derived from microscopic covalent bonding the characteristic scale is $E \sim nN/nm^2 \sim GPa$. For an object of radius r the area moment of inertia scales as $I \sim r^4$, giving the persistence length at room temperature $l_p \sim 100r^4/\mathrm{nm}^3$. The strong scaling with cross sectional dimension suggests that thermal fluctuations are irrelevant for majority of macroscopic objects. A human hair, for example,

would need to reach a length of $\sim$ 100 kilometers before thermal fluctuations reached an appreciable level! Typical polymers, however, have $r \sim$ nm and thus are expected to have persistence lengths on the order of micrometers. This allows different polymers to display both flexible and semi-flexible behavior at room temperature.

1.1.2 Polymer Networks

The natives of the Amazon basin were some of the first to take advantage of the remarkable properties of polymer networks: They collected sap from the hevea tree and, after letting it harden upon their feet, created the world's first rubber boots. The sap is comprised of long flexible polymers which are able to bond to one another in the presence of oxygen, a process responsible for changing the phase of the network from fluid-like sap state to a rubber which is able to support elastic stresses. Sensitive mechanical dependence on chemical composition, and more generally on the microscopic details of the system, is a general feature of networks, which is surprising given the macroscopic number of constituent polymers. For example, a network of semi-flexible polymers (created by the introduction of small molecules known as cross-linkers which bind the polymers) will display highly non-linear elastic response stemming from the asymmetric elastic response of the individual polymers to an applied longitudinal load: They can support large tensile stresses but buckle easily under compression [MKJ95]. In the presence of cross linkers, which are necessary to transmit stresses, the macroscopic network will be observed to rapidly strain stiffen and develop negative normal stresses [HLM03, CMS13] when subjected to external shear stress.

Cross-linkers allow for the formation of secondary structure within otherwise amorphous semi-flexible networks. Depending on the type of cross-linker and the concentration, polymers may order into one dimensional bundles of parallel filaments or into two dimensional lamellar structures. Naturally, the elasticity

of these objects are significantly different than the amorphous network, and in this way the cross-linkers may play a key role in determining the macroscopic mechanical properties of the network.

1.1.3 Soft Matter out of Equilibrium

An additional feature of polymer networks, and in fact nearly all soft matter, is that they may be driven out of equilibrium in a controlled fashion. Hard matter systems offer no such luxury: The characteristic energy scale of the system is also responsible for holding the constituent particles together (for example atoms in a crystal lattice), and non equilibrium forcing of this magnitude will necessarily lead to catastrophic failure of the sample! Soft matter systems have no such limitations as they are often elastic and naturally robust to fluctuations of order $k_{\mathrm{B}}T$ and can be easily driven actively at those energy scales without destroying the system. Polymers, for example, can be driven continuously out of equilibrium by stretching or compression while still retaining their microscopic integrity. While the effect of thermal fluctuations on macroscopic network elasticity has been studied extensively [GSM04], much less progress has been made towards understanding these systems in the presence of active noise. When the noise is small, the fluctuation-dissapation theorem may be used to relate non-equilibrium properties to known equilibrium ones, but the question of how to deal with systems far from equilibrium remains. Additionally, one may ask what types of noise even allow for a near equilibrium description: Certain active processes necessarily drive the system far out of equilibrium.

1.2 The cytoskeleton as a model soft matter system

Biology offers the soft matter physicist a tremendous set of ready made systems to explore. For the purposes of studying semi-flexible polymer networks in and

out of equilibrium, one could not ask for a better realization than the cytoskeleton present within nearly all eukaryotic cells, shown in Fig. 1.1. The cytoskeleton is a network of interconnected polymers responsible for providing structural integrity to the cell, as well as being essential for mitosis and for cell motility. The cytoskeleton is made up of many different polymers, but the two most prevalent and well studied are filamentous actin (often referred to simple as actin) and microtubules, both of which are easily observed *invivo* and synthesized in a controlled manner *invitro*. Actin is by far the softer of the two filaments, with a persistence length of about 17μm, whereas microtubules have l_p on the order of millimeters. This implies that only actin will experience appreciable thermal fluctuations at cellular length scales; microtubules in contrast will appear perfectly straight. Chapters two and three will focus on the role filament fluctuations play in the distribution of network cross-linkers and will be directly applicable to the actin component of the cytoskeleton. Both filaments are easily deformed, however, and serve as valid examples of networks driven out of equilibrium, which is the focus of Chapter four. Different network morphologies are observed within the cytoskeleton, including bundles and lamellar networks. These structures are made possible by the great variety of biological cross-linking proteins, and often many proteins are present at once, giving rise to incredibly complex networks. Generally speaking, cross-linkers may be categorized into two groups: bundling" and "network." Bundling cross-linkers, such as α-actinin for actin and tau proteins for microtubules, prefer to bind filaments parallel to one another and offer very little angular compliance. This naturally is responsible for bundle formation within the cytoskeleton. Network cross-linkers, conversely, either have no angular preference or bind filaments at right angles to one another, facilitating the formation of two dimensional planar structures. Examples of network linkers are filamin for actin networks and biotin-streptavidin for microtubules. The distinction between angle constraining and compliant cross-linkers will turn out to have dramatic implications on the

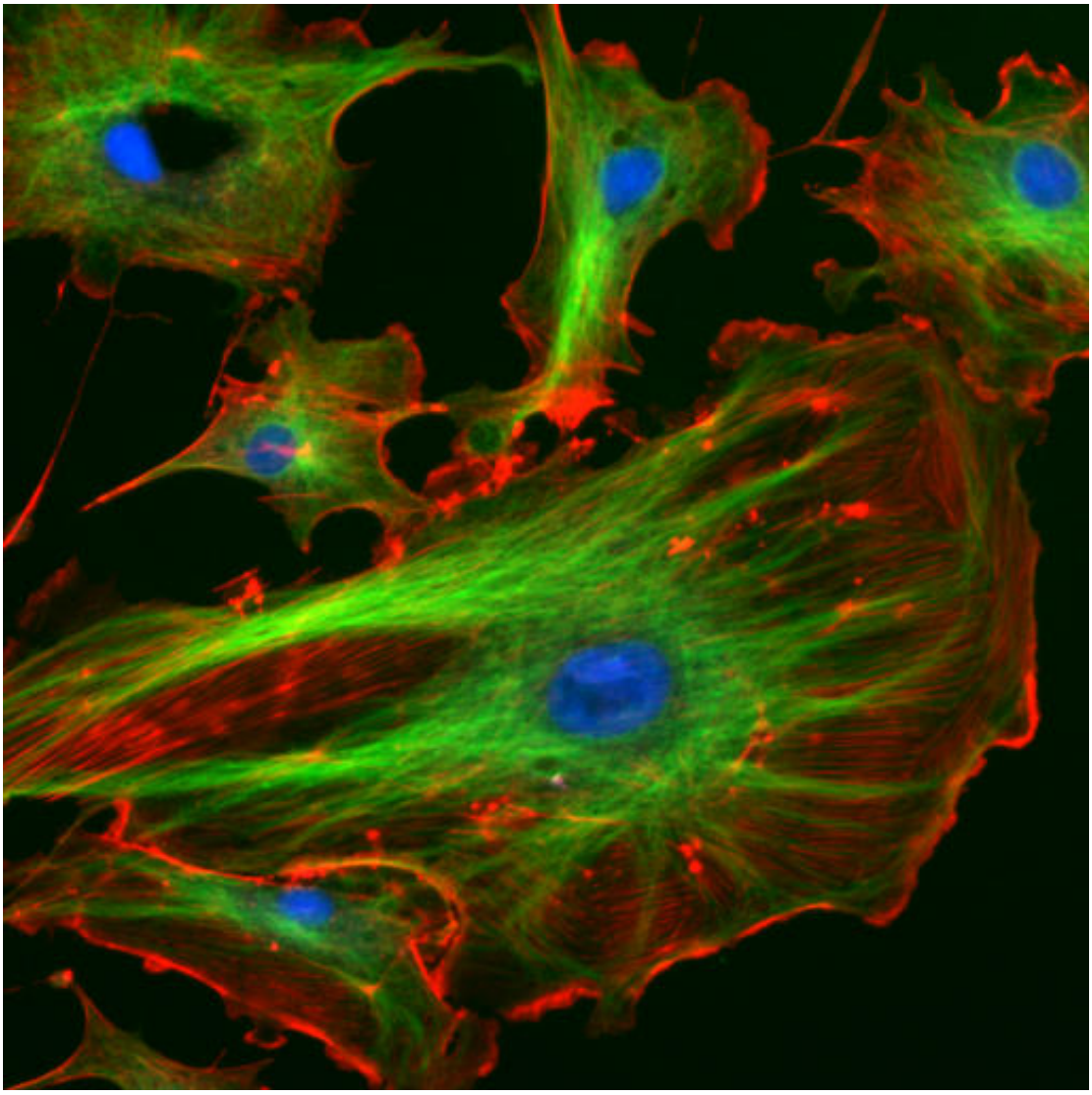

Figure 1.1: The cytoskeleton. Red: Actin filaments, Green: Microtubules, Blue: Intermediate filaments

fluctuation induced forces proposed in Chapter 2.

The living cell is, of course, strictly out of equilibrium; When that cease to be true the cell is unfortunately dead. Biopolymer networks are actively driven out of equilibrium through the presence of molecular motors such as myosin, which binds to actin, and the microtubule version kinesis. These motors play a huge role, respectively, in muscular function and cellular transport. When viewed as a mechanics problem, the motors are a form of stochastic noise which exert active forces upon the underlying network, driving it potentially very far from equilibrium.

1.3 Casimir forces

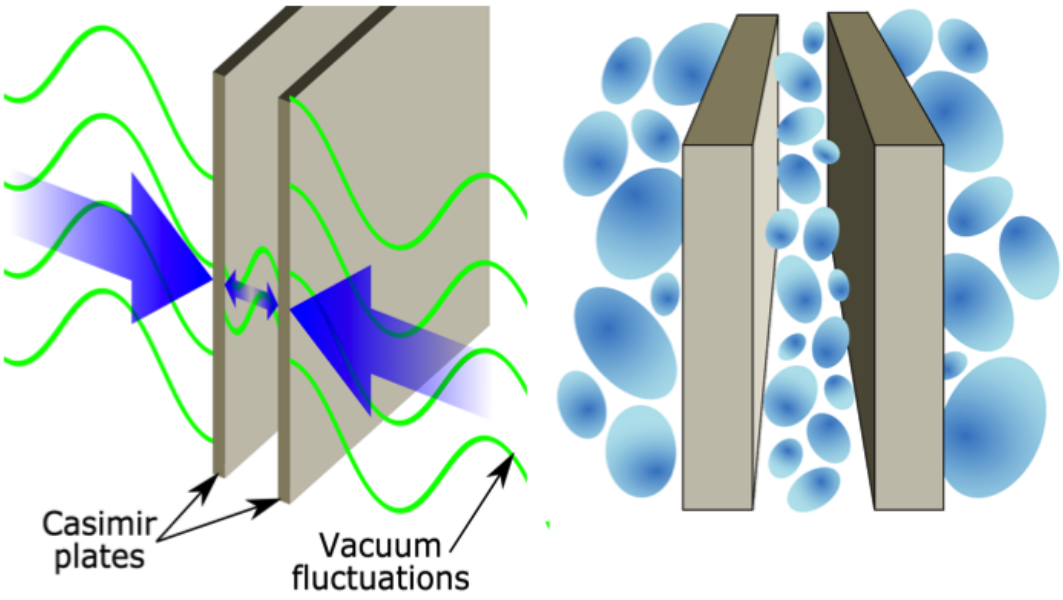

Figure 1.2: Left: Quantum Casimir effect. Right: Thermal Casimir effect – As the two plates are brought closer together, fluctuations between the plates are suppressed while the entropy of the surrounding medium increases resulting in an attractive interaction between the plates.

There is an additional class of forces known as fluctuation, or *Casimir* forces after the pioneering work of H.G. Casimir [Cas48] who studied a system of two parallel conducting plates in vacuum, as shown in Fig. 1.2. According to the classical theory the plates should not experience an electrostatic interaction since they are uncharged, however this treatment neglects the effect of the plates on the quantum vacuum fluctuations of the electromagnetic field. Because the plates are perfect conductors they impose boundary conditions which quantize the otherwise continuous vacuum fluctuation spectrum between the plates. The quantized mode spectrum, not surprisingly, depends on the distance between the plates and thus there is an effective interaction which turns out to decay as $1/D^4$, where D is the plate separation.

Casimir's discovery sparked a vast amount of research on fluctuation mediated interactions in quantum field theories at zero temperature [Wei89, DS93], but the idea of a fluctuation force is in fact much more general. Casimir type forces are present whenever an object modifies the spectrum of a background fluctuating field by imposing boundary conditions. The background fluctuations can arise from quantum mechanics, as in the original Casimir problem, or from thermal fluctuations which excite modes in systems at finite temperature. The resulting interactions are pronounced in systems with massless modes such as those associated either with broken continuous symmetries (Goldstone modes) in e.g., liquid crystals [ABD92], or at a critical point – see Refs. [Kre94, MT97, KG99]. As a specific example within soft matter physics, two plates surrounding a nematic liquid crystal will attract because of boundary conditions they impose on the fluctuating nematic order field. [ABD92].

The Casimir interaction between two plates is reminiscent of a depletion force, whereby an attractive osmotic pressure is generated by the exclusion of particles beyond certain size from the interior region, see Fig. 1.2. In analogy, the boundary conditions on the plates restrict fluctuations of a certain size, i.e. wavelength,

from existing within the plates, resulting in an effective pressure or depletion type force pushing the plates together. This analogy, while instructive, is not exact, as can be inferred from the observation that the Casimir interaction can be either attractive (as suggested by the above analogy) or *repulsive*, depending on the boundary conditions imposed on the fluctuations by the embedded objects [DLP61], whereas the depletion interaction is necessarily attractive.

Casimir forces are often obscured by stronger, direct interactions, but not always. For example, the Casimir force between membrane proteins – and other membrane inclusions – interacting through thermally excited membrane undulations are important because this interaction decays as a power law with distance whereas direct protein-protein interactions are short ranged [BGP94, ZPZ98].

Cross-linkers in semi-flexible polymer networks have only very short ranged direct interactions and thus constitute a system where fluctuation forces could be important. When they bind a polymer to a background elastic network they restrict the thermal fluctuations of the polymer, or in other words they impose boundary conditions. It is easy to imagine that when two cross-linkers are bound to the same filament they will experience a Casimir type interaction acting along the contour of the filament. This interaction is expected to be proportional to temperature since it is a direct consequence of the cross-linkers impact on the configurational entropy of the filament. Because of the lack of competing enthalpic interactions, the Casimir force is able to play a significant role in the equilibrium distribution of cross-linkers within the network, and furthermore is able to favor bundling and other higher order structure formation. The interaction also sharpens the deposition curves, or Langmuir isotherms, of a solution of cross-linkers onto semi-flexible filaments. Cells may take advantage of this increased sensitivity to use overall cross-linker concentration as a control parameter for network morphology.

1.4 Thesis Outline

In chapter 2 I will propose the Casimir force between a small number of cross-linkers joined to the same semi-flexible polymer, and calculate its form directly with different mathematical approaches. I will also present simulation based evidence for its existence and discuss implications for biological networks Chapter 3 will focus on extending the interaction to many cross-linkers with a statistical mechanical approach, and explores the implications for fine tuned bundle formation within the cytoskeleton. Finally, chapter 4 will discuss the mechanical properties of networks out of equilibrium. First I will imagine homogenous polymer networks subjected to active *correlated* noise, which is meant to model the effect of molecular motors within cytoskeletal networks. Secondly, I will present work which explains the nonlinear strain stiffening observed in biopolymer networks under external strain.

CHAPTER 2

Casimir Effect Between Cross-linkers in Semi-flexible Polymers

2.1 Introduction

Fluctuation-induced, or *Casimir* interactions been studied extensively in the limit of highly flexible polymers [DE86, RC03], and are responsible for the entropic elasticity present in rubbers and polymer melts. In this chapter I propose and verify the existence of Casimir interactions between cross-linkers in the opposite limit of *semiflexible* polymers, which have contour lengths shorter than or comparable to the thermal persistence length l_p and are naturally observed in nearly straight configurations. Figure 2.1 shows an example of two polymers held together by sliding linkers. The existence and sign of a Casimir-type force between the linkers can be understood intuitively: Imagine that one pins two points along an otherwise free filament to a background substrate. The addition of a fixed point reduces the number of conformational degrees of freedom, and hence also the entropy. Two fixed points at finite separation result in a further reduction of the number of available states over a single fixed point, and the system will therefore find it entropically favorable to place both fixed points at the same position. This argument holds at arbitrary separations and it is natural to expect the resulting Casimir interaction to be long-ranged, and in fact it is logarithmic in the separation–see Sec. 2.3.

The physical interest of this problem lies in possible applications in polymer

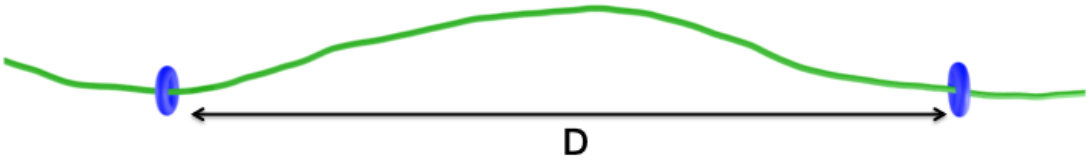

Figure 2.1: Two semiflexible polymers are linked by two sliding rings. Thermal fluctuations of polymer segments in between the rings are constrained. By reducing the separation D between the rings, degrees of freedom transferred from in between the rings to the exterior increase the entropy of the system. This generates an attractive interaction between the rings.

networks. Thermal fluctuations have long been known to play a central role for the viscoelastic properties of networks of polymers [HLM03]. In particular, the *force-extension curve* $\tau(D)$ of a polymer of fixed length connecting two points separated by a distance D is believed to determine the elastic properties of polymer network. This force-extension curve is determined largely by thermal fluctuations. There is, however, a fundamental difference between this form of entropic elasticity and the thermal Casimir effect of Fig. 2.1: if two permanent nodes of a polymer network are brought closer there is no transfer of degrees of freedom from the polymer section between the nodes to the rest of the network. When the two linkers of Fig. 2.1 are brought together, degrees of freedom are transferred from the section in between the linkers to the surrounding system. In addition, the computation of the Casimir effect typically requires the regularization of infinities associated with summations over all fluctuation modes. No such divergences appear in the calculation of entropic elasticity.

There are interesting examples of *biopolymer* networks, for example F-actin cross-linked with α-actinin, where linker proteins bind reversibly to the protein filaments, allowing them to effectively slide along the filament and sample con-

figuration space. Such proteins might exhibit a Casimir interaction due to their modification of the thermally excited transverse undulations of the filaments to which they are bound. A first objection against this idea is that, for typical biopolymer networks, the persistence length is much greater than the separation between linkers. On length scales small compared to the persistence length, thermal shape fluctuations must have a low amplitude, so the Casimir interaction is expected to be very weak. Secondly, biopolymer networks often are under tension, either intrinsic or externally applied. Tension introduces a length scale in the problem beyond which thermal fluctuation are suppressed. In this chapter, I will demonstrate that the Casimir interaction between sliding linkers on length scales smaller than the persistence length cannot be neglected, both in networks with and without tension. I will show that neither effect suppresses the Casimir interaction. Finally, we show that if the linker molecules imposes angular constraints on the filaments at the cross link, then this generates repulsive elastic stresses, which overwhelm the Casimir interaction. Thus, I propose that distinction between between flexible cross linkers and stiff ones, associated with filament bundling has important consequences for the equilibrium distribution of these molecules in semiflexible filament networks.

The chapter is outlined as follows: In Sec. 2.2 we discuss the calculation of the partition function that is required for the derivation of the Casimir force. Because of the appearance of higher-order derivatives in the Hamiltonian H, the standard method for evaluating Gaussian functional integrals by path integration is questionable. We will apply a technique introduced by H. Kleinert [Kle86] for field-theoretic problems to define the integration measure for path integrals with actions that contain higher-order derivatives. In Sec. 2.3 we compute the Casimir interaction using this functional integral technique, examine a few special cases, and review the results in the context of biopolymer networks. Finally, in Sec. 2.4 I introduce evidence supporting the existence of a Casimir force from large-scale

numerical simulations.

2.2 Partition function of a pinned semi-flexible polymer

2.2.1 System geometry & Hamiltonian

The basic building block of a cross-linked polymer network is two filaments joined by a single cross-linker. The fluctuation interaction can be probed by allowing an additional cross-linker to bind these two filaments at a separate location. Specifically, as shown in Fig. 2.1 let two cross linkers placed along the z axis and $z = 0$ and $z = D$ permanently bind two semiflexible polymers, each having bending modulus κ and thus persistence length $l_p = \beta\kappa \gg D$, where $\beta = \frac{1}{k_{\mathrm{B}}T}$ and k_{B} is Boltzmann's constant. The cross linkers fix the position and direction of the polymer at the linker locations but the length of the polymer between the linkers is not fixed. As a simplification the filaments are assumed not to interact with one another, i.e. steric interactions are neglected. In this case the filaments decouple and it is sufficient to study a single filament pinned by two cross linkers, see Fig. 2.2.

The elastic energy of the filament is given by

$$\mathcal{H}\left[\vec{h}\right] = \frac{1}{2}\int_0^L \mathrm{d}s \left[\kappa\left(\frac{d^2\vec{r}(s)}{ds^2}\right)^2 + \tau\left(\frac{d\vec{r}(s)}{ds}\right)^2\right], \tag{2.1}$$

where s is an arc length variable traversing the filament from $z = 0$ to $z = D$ and $\vec{r}(s)$ specifies the filament position. The first term gives the contribution to filament curvature while the second term accounts for a tension τ applied to the polymer. Because the polymer can freely slide through the linkers, the linkers do not absorb this tension. In principle there is also a contribution from torsional deformations but these modes are generally much stiffer and are neglected. For $D \ll l_p$ the filament will be nearly straight and the energy functional Eq. 2.1 may be expanded in the small gradient expansion in term of a displacement field $\vec{h}(z)$

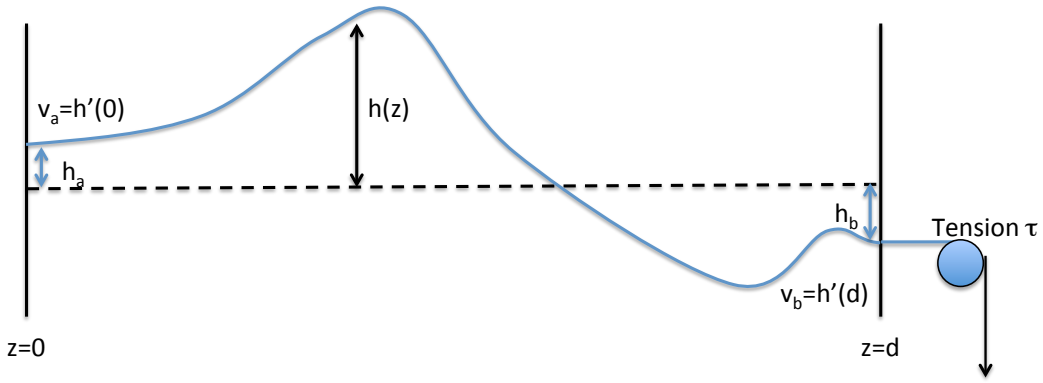

Figure 2.2: A semi rigid filament of projected length d characterized by the height field h(z). The filament has a bending rigidity κ and may be under an external tension τ, as well as being contained in a confining potential of strength k. The deformations are exaggerated for clarity–we treat stiff filaments so that the small bending approximation is appropriate.

measured from the z axis:

$$\mathcal{H}\left[\vec{h}\right] \approx \frac{1}{2}\int_0^D \mathrm{d}z \left[\kappa\left(\frac{d^2\vec{h}(z)}{dz^2}\right)^2 + \tau\left(\frac{d\vec{h}(z)}{dz}\right)^2\right], \tag{2.2}$$

Within the small gradient approximation it is clear that the two transverse polarizations $h_{x,y}(z)$ of the filament undulations decouple, so that the resulting partition sum is simply the product of two copies of the partition sum over a scalar field $h(z)$ representing one transverse mode, but still obeying the Hamiltonian Eq. 2.2. The equation may be nondimensionalized by introducing a rescaled length $z = (\beta\kappa)^{\frac{1}{3}}\tilde{z} = l_p^{\frac{1}{3}}\tilde{z}$. Finite tension introduces a length scale, which we write in terms of a wave number $q = \left(\beta\tau/l_p^{1/3}\right)^{1/2}$. We note that the rescaled length $\tilde{z}$ has physical dimensions of $\mathrm{L}^{\frac{2}{3}}$; q has dimensions of inverse $\tilde{z}$. After this change of

variables, the filament Hamiltonian reduces to

$$\mathcal{H} = \frac{1}{2}\int_0^D \mathrm{d}z \left[h''(z)^2 + q^2 h'(z)^2\right], \tag{2.3}$$

where here and unless stated otherwise we remove the tildes from all rescaled lengths and we measure energies in units of β^{-1}.

As discussed in 1.3, fluctuation forces are generated by the boundary conditions external objects generate on the fluctuating field. In the simplest version of this problem the cross linkers impose exact local boundary conditions on the displacement $h(z=0) = h_a, h(z=D) = h_b$ and direction $h'(z=0) = v_a, h'(z=D) = v_b$ of the filament, as shown in Fig. 2.2 These boundary conditions correspond to *perfect pinning* cross linkers, i.e. , ones that can provide arbitrary constraint forces and torques to perfectly fix the filament's position and slope, respectively. In any physical biopolymer system, however, the cross linking molecules have some finite elastic compliance and are of finite size and such molecules cannot precisely pin the filament at a point. The use of perfect cross linkers allows one to better isolate the role of filament fluctuations on the Casimir interaction of two cross linkers. The finite size of the cross linkers may be considered within this framework by modeling them as rings that enforce the boundary conditions only when the filament's transverse displacement becomes larger than the rings' radius–see Fig 2.1 and Sec. 2.3.5 for more details.

2.2.2 Calculation Details

2.2.2.1 Decomposition into classical and fluctuation paths

The partition function contains all the relevant statistical mechanical information of a system and is defined as the sum over all states weighted by the Boltzman factor e^{-E_n}, where E_n is the energy of the nth state (measured in units of β^{-1}). For a continuous distribution of states, appropriate for a polymer, the sum becomes

an integral over all configurations of the field

$$\mathcal{Z} = \int \mathcal{D}h e^{-\mathcal{H}[h]}, \tag{2.4}$$

and is known as a functional integral. The partition function for a filament pinned by cross-linkers will have the Hamiltonian $\mathcal{H}$ given by Eq. 2.3. Any dependence of the partition function on the distance between cross linkers, D, will be indicative of a fluctuation force between the cross linkers. The integration measure $\mathcal{D}h$ represents the sum over all configurations of the filament satisfying the given boundary conditions. The mathematical representation of such an object can be difficult and will be discussed in greater detail later.

In analogy to the standard presentation of the path integral approach to classical quantum mechanics [FH65], the height field $h(z)$ is first decomposed as a sum of the classical solution $h_{\rm cl}(z)$, which minimizes the energy, and the fluctuations $\delta h(z)$ around it, writing

$$h(z) = h_{cl}(z) + \delta h(z). \tag{2.5}$$

The stationarity condition $\frac{\delta \mathcal{H}}{\delta h} = 0$, which imposes the force balance condition for a flexible beam, requires the classical trajectory to satisfy the differential equation

$$h_{cl}'''' - q^2 h_{\rm cl}'' = 0. \tag{2.6}$$

The classical solution is required to explicitly satisfy the boundary conditions at the end points $z = 0$ and $z = D$. By choosing the appropriate coordinate system, i.e. by rotating the z axis, one may always set $h(0) = h(D) = 0$. The initial and final tangents are defined to be: $h'(0) = v_a, h'(D) = v_b$, as shown in Fig. 2.2. Because the classically solution satisfies all boundary conditions the fluctuation field $\delta h(z)$ and its first derivative are required to vanish at the endpoints, i.e. $\delta h(z)$ satisfies homogeneous boundary conditions. The general solution of Eq. 2.6 is

$$h_{cl}(z) = a \sinh qz + b \cosh qz + cz + d, \tag{2.7}$$

with undetermined constants, a, b, c, d.

Using the decomposition Eq. 2.5 and integrating by parts, one finds that the energy of a configuration separates into a classical path contribution and one from the fluctuations about that path: $\mathcal{H} = \mathcal{H}_{cl} + \mathcal{H}_{\rm fl}$. The energy associated with the classical trajectory is given solely by the boundary term:

$$\mathcal{H}_{cl} = \frac{1}{2}\left[h'_{\rm cl}h''_{\rm cl} - h'''_{\rm cl}h_{\rm cl} + q^2 h'_{\rm cl}h_{\rm cl}\right]\Big|_{h'(0)=v_a}^{h'(D)=v_b}. \tag{2.8}$$

Since the initial and final values of $h_{\rm cl}$ were chosen to be zero, only the first term makes a non-vanishing contribution to the elastic energy of the curved filament. Applying the boundary conditions to set the undetermined constants in Eq. 2.7, one finds

$$\begin{aligned} a &= \frac{1}{M}\left[(v_a - v_b)(\cosh qD - 1) - qDv_a \sinh qD\right] \\ b &= \frac{1}{M}\left[(v_b - v_a)\sinh qD + qdv_a \cosh qD - qDv_b\right] \\ c &= \frac{1}{M}\left[q(v_a + v_b)(\cosh qD - 1)\right] \\ d &= \frac{1}{M}\left[(v_a - v_b)\sinh qD + qDv_b - qDv_a \cosh qD\right], \end{aligned} \tag{2.9}$$

where $M = q[2(\cosh qD - 1) - qD\sinh qD]$ is the determinant of the boundary condition matrix. The corresponding energy is given by

$$\mathcal{H}_{cl} = \frac{1}{2}\frac{q\left(qD(v_a^2 + v_b^2)\cosh(qD) - (v_a - v_b)^2\sinh(qD) - 2qDv_a v_b\right)}{2(1 - \cosh(qD)) + qD\sinh(qD)}. \tag{2.10}$$

The above result reduces to a particularly simple form in the limit of zero tension ($q = 0$) in which case the elastic energy of the filament depends on the initial and final tangents through the expression

$$\mathcal{H}_{cl} = \frac{2l_p k_{\rm B}T}{D}\left(v_a^2 + v_b^2 + v_a v_b\right), \tag{2.11}$$

where the answer has been expressed in the original units. In response to choosing symmetric imposed tangent angles, $v_a = -v_b = \theta/2$, and defining a radius of curvature R via $\theta = D/R$, the energy minimizing filament trajectory is an arc of

a circle with radius R and the stored elastic energy is $\frac{\kappa D}{2R^2}$ (again in the original units), as is expected. This solution is shown in Fig. 2.3. Of course, for much larger bends, where the replacement of the curvature by the second derivative in the Hamiltonian is inappropriate, a more complicated solution is obtained involving elliptic functions [LL86].

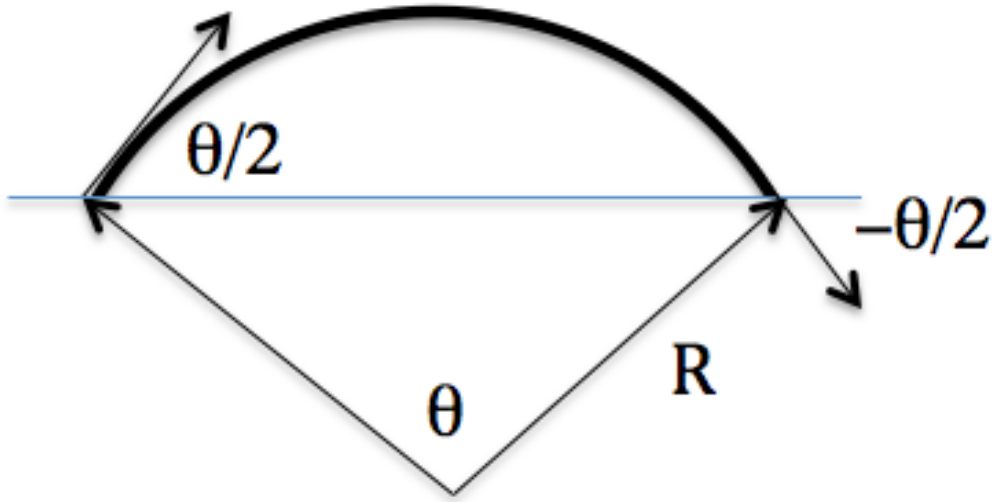

Figure 2.3: Elastic rod subject to a torque is bent into the shape of a circular arc. The radius of curvature of the arc is R and the angle subtending the arc is θ.

The energy of the fluctuation piece $\mathcal{H}_{fl}$ is simply given by

$$\mathcal{H}_{\rm fl}[\delta h] = \frac{1}{2}\int_0^D {\rm d}z\, \left[\delta h''(z)^2 + q^2 \delta h'(z)^2)\right], \tag{2.12}$$

The partition function Eq. 2.4 may now be written as a functional integral over all configurations of $\delta h(z)$ with vanishing displacement and slope at the boundaries

$$\mathcal{Z} = \mathcal{Z}_{cl}\mathcal{Z}_{fl} = e^{-\mathcal{H}_{cl}} \int \mathcal{D}\delta h(z)\, e^{-\mathcal{H}_{\rm fl}[\delta h]}. \tag{2.13}$$

The factor $\mathcal{Z}_{fl}$ depends only on the nature of the fluctuations and is aptly named the fluctuation factor in path integral literature. Section 2.2.2.3 will detail an

explicit evaluation of $\mathcal{Z}_{fl}$, but first I will explore the validity of a less formal approach to understanding the statistical properties of a pinned filament.

2.2.2.2 Naïve mode analysis of the fluctuation factor & divergences

The direct evaluation of the functional integral Eq. 2.13 is quite involved and it is reasonable to ask if there is a simpler method. Because the Hamiltonian is quadratic in the field it is straightforward to evaluate the partition function and corresponding free energy as a sum over the quantized eigenmodes. The theory requires a short distance cutoff which is parametrized by $\epsilon = \frac{D}{N+1}$, where N is the number of included modes, and in polymer systems one typically imagines this length to be related to the monomer size. For the continuum approach to be meaningful, intensive quantities, including the Casimir force defined as the derivative of the free energy with respect to D, should not depend on the precise formulation of this cutoff. On the other hand, extensive thermodynamic properties, such as the heat capacity, necessarily depend on the number of degrees of freedom and thus retain an ϵ dependence. The partition function of the segment can be evaluated by expanding the fluctuation displacement field δh into a series of harmonic modes which automatically satisfy the vanishing displacement and slope boundary conditions

$$\delta h_n = \sqrt{\frac{2}{3(N+1)}} \sum_{m=1}^{N} A_m(\cos(k_m z_n) - 1), \tag{2.14}$$

with wavenumber $k_m = 2\pi m/D$. The normalization of the harmonic modes in Eq. 2.14 has been chosen so as to set the Jacobian of the transformation to unity. The calculation of the remaining Gaussian integrals is straightforward. The answer can be inferred directly by noting that the energy stored in the mth mode in thermal equilibrium is found by equipartition to be

$$U_m = \frac{\epsilon}{4}(k_m^4 + q^2 k_m^2) A_m^2, \tag{2.15}$$

which is the energy of a harmonic oscillator having spring constant $K_m = \frac{\epsilon}{2}(k_m^4 + q^2 k_m^2)$. Since these harmonic modes are decoupled, the free energy of the N modes with spectrum $\omega(k_m) \propto \sqrt{K_m}$ is given by the sum

$$F(D) = \sum_{m=1}^{N} \ln[\Gamma\omega(k_m)] \tag{2.16}$$

of their free energies. Here Γ is a phase space factor which does not depend on D. Converting the summation to an integration, one may write

$$F(D) = \frac{D}{2\pi} \int_{2\pi/D}^{2\pi/\epsilon} \mathrm{d}k \, \ln(\Gamma\omega(k)). \tag{2.17}$$

At zero tension this reduces to

$$F(D) = D \ln(\Gamma\epsilon)^{\frac{1}{2}} \left(\frac{1}{\epsilon} - \frac{1}{D}\right) + 2D \left(\frac{1}{\epsilon}\ln(2\pi/\epsilon) - \frac{1}{D}\ln(2\pi/D) - \frac{1}{\epsilon} + \frac{1}{D}\right). \tag{2.18}$$

The free energy is formally divergent in the limit $\epsilon \to 0$ and it would appear meaningless to consider this expression in the continuum limit. Nevertheless, one is able to extract finite results by using the following procedure: Consider a filament of total length $L \gg D$, which, to avoid additional complexities associated with the choice of boundary conditions at the free ends, is assumed to be linked into a loop. Then the total free energy of the loop with two cross links is $F_T(D) = F(D) + F(L-D)$. The Casimir force $-dF_T(D)/dD$ is then $f_C(D) = f(D) - f(L-D)$, where I have introduced $f(D) = -dF(D)/dD$. Each of the two fluctuation-induced interactions between the linkers takes the form

$$f(D) = -\frac{1}{\epsilon}\ln\left(\frac{\Gamma(\epsilon)^{1/2}}{k_B T}\right) - 2\left(\frac{1}{\epsilon}\ln(2\pi/\epsilon) + \frac{1}{D} - \frac{1}{\epsilon})\right). \tag{2.19}$$

Each force is still formally divergent as $\epsilon \to 0$, however, after the subtraction of the two fluctuation-induced interactions within the loop the residual Casimir force is finite and, in the limit $\frac{L}{D} \to \infty$ is given by

$$f_C(D) \approx -\frac{2}{D}. \tag{2.20}$$

It is essential to recognize that the finite Casimir force between the two cross linkers on the loop was produced by the subtraction of the two fluctuation-induced interactions, each of which diverged in the continuum limit of $\epsilon \to 0$. This naïve mode analysis is not capable of separating the finite Casimir force from these cutoff dependent terms, which diverge in the continuum limit. Although this result is shown for the case of a filament at zero tension, the same issue appears for all finite tension. That tension, of course, can be employed as a Lagrange multiplier in order to fix the mean arc length of the filament. Controlling mean length in this way does not eliminate the divergences associated with naïve mode analysis.

Of course, physical polymers have a natural short distance cutoff related to their monomer size. By fixing ϵ the naïve mode analysis gives the free energy of a polymer of $N = D/\epsilon$ degrees of freedom. The variation of that free energy with length D (necessary to calculate the Casimir force) changes the total number of degrees of freedom making the analysis of the problem complicated. This procedure gives a Casimir force with cutoff-dependent contributions. The precise nature of the cutoff, however, should not determine the physical force between distant pinning sites on the polymer. The subtraction scheme used above masks our ignorance by removing this cutoff dependence and, although it does in fact reproduce the correct Casimir force (see Sec. 2.3 for the rigorous result), it is not inherently satisfactory. The appearance of infinities in the Casimir force calculation raises questions as to the reliability of our result, as it is far from clear that our procedure properly separates the divergent and non-divergent terms.

As mentioned, the appearance of divergences is a signature of calculations of the Casimir force [ABD92], and more broadly of path integral calculations. Additional care must be employed in taking the continuum limit in the Casimir force calculation than is generally necessary in computing other physical quantities associated with semiflexible filaments. For example, one may compute the force extension curve of such a filament and take the continuum limit without

encountering the infinities discussed above. We review that calculation briefly.

Including a finite tension on the filament, we may compute the thermal expectation values of the squared amplitudes – see Eq. 2.14 – of the various undulatory fluctuations on the filament. Using the equipartition theorem and Eq. 2.15 we immediately obtain

$$< A_m^2 >= \frac{2}{\epsilon}(k_m^4 + q^2 k_m^2)^{-1} \tag{2.21}$$

The arc length L of the filament between two points separated by D is

$$L = \int_0^D dz \sqrt{1 + h'(z)^2}, \tag{2.22}$$

where we again only consider one polarization state for the fluctuations. Using Eqs. 2.21 and 2.22 we find the mean arc length between those points to be given by

$$L/D - 1 \propto \frac{1}{D} \sum_{m=1}^{D/\epsilon} (k_m^2 + q^2)^{-1}. \tag{2.23}$$

The key observation is that the summation converges in the limit $\epsilon \to 0$. In that continuum limit, changing from summation to integration leads to the force-extension relation $(L/D-1) \propto 1/\tau^{1/2}$ for semiflexible polymers in the limit of high tensions. This is a well-known result that has been verified by micromechanical experiments [BMS94].

2.2.2.3 Direct evaluation of the fluctuation factor

Given the difficulties encountered in the naïve approach of the previous section, we now return to the direct evaluation of the path integral in $\mathcal{Z}_{fl}$ (Eq. 2.13). The natural way to compute functional integrals is to slice each path into N infinitesimal straight line segments of width ϵ–See Fig. 2.4. The paths are represented mathematically by N independent height fields δh_i, and the measure $\mathrm{D}\delta h$ may

then be defined as the product of N standard integral measures

$$\mathcal{D}\delta h = \prod_{n=1}^{N} \int_{-\infty}^{\infty} \mathrm{d}\delta h_n. \tag{2.24}$$

To specify $\mathcal{H}_{\mathrm{fl}}$ on a particular spatial slice, one must know the value of $\delta h(z)$ on both adjacent slices so that the derivatives may be evaluated. This naturally induces a dependence on the width of the slices and requires an ϵ dependent "measure factor" (see [FH65]) to be included in $\mathrm{D}\delta h$ so that the path integral is well defined in the limit $\epsilon \to 0$. The correct (insofar as it produces a finite result as $\epsilon \to 0$) measure factor is known for functionals with a single derivative, but this factor is not appropriate for Hamiltonians with higher order gradients. The statistical mechanics of a semi-flexible polymer should be well defined in the continuum limit (it's mechanical description certainly is!), and the lack of a suitable path integral representation of the partition function is disconcerting.

A related problem is the specification of the discrete form of Hamiltonians with second (or higher) order derivatives in the sliced representation. The piecewise construction naturally invites replacing $h'(z)$ by by $(h(z_{i+1}) - h(z_i))/\epsilon$, but it is unclear how to represent $h''(z)$. These terms, representing curvature energy, would be infinite at the cusps of a piece-wise linear trajectory. Replacing the curvature by a discrete second derivative avoids this divergence but that introduces additional interactions between slices that are not adjacent, with mathematically unclear consequences.

One solution, introduced by Kleinert [Kle86], is to rewrite $\mathcal{H}$ in terms of four independent canonical functions. The value of $\mathcal{H}$ on each slice will be determined by the four functions evaluated locally on that slice, with no dependence on adjacent slices, and therefore no ambiguity in defining the curvature energy. The measure in terms of these functions will therefore be independent of the slicing procedure and may easily be written down up to an overall normalization constant. The method is actually quite general, and in particular it is able to reproduce the

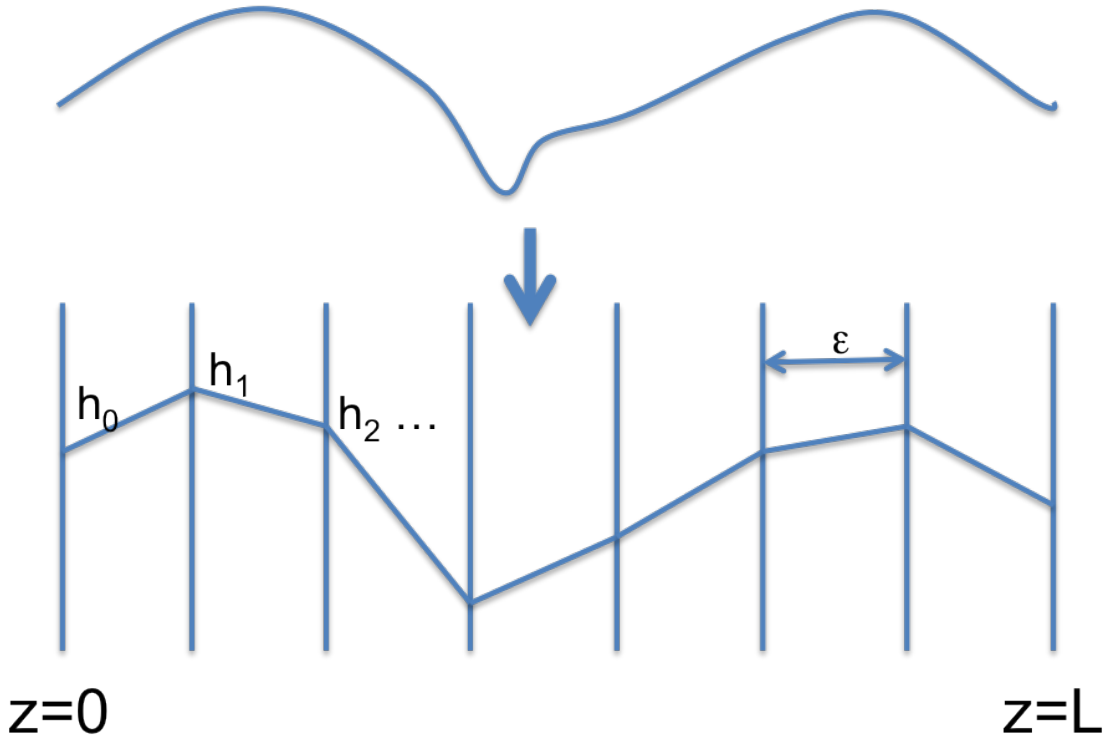

Figure 2.4: Slicing the function into a set of interpolating straight line segments is the first step towards direct evaluation of the path integrals. As the slice width $\epsilon \to 0$ the approximation is expected to approach the exact answer. While the straight lines are appropriate for functionals with first order derivatives, it is clearly problematic for higher order functionals because the derivatives will be undefined at the kinks.

"measure factor" Feynman introduced for first order gradient functionals. The next section will introduce the main idea in the context of a simple tense string (the mechanical analogue of a free particle), and also expose the reader to an explicit functional integral calculation before diving into the more complicated pinned semi-flexible polymer system.

2.2.2.4 A warmup problem: The partition function of a string

Feynman [FH65] showed the proper way to evaluate path integrals in the context of the quantum mechanical propagator for a particle with classical action $\mathcal{S}$

$$K(x_b, t_b; x_a, t_a) = \int_{a\to b} \mathcal{D}x(t)\, e^{\frac{iS}{\hbar}}. \tag{2.25}$$

The propagator K is the amplitude for the process of a free particle starting at x_a at time t_a being observed at x_b at time t_b. The simplest example is of course the free particle, described by the action

$$\mathcal{S} = \frac{1}{2}\int_{t_a}^{t_b} \mathrm{d}t\, m\dot{x}^2. \tag{2.26}$$

Aside from the factor of i which may be removed by a Wick rotation, there is mathematically no difference between the propagator of a free particle and the partition function of a string under tension

$$\mathcal{Z} = \int \mathcal{D}h(z) e^{-\mathcal{H}}, \tag{2.27}$$

where the energy functional is

$$\mathcal{H} = \frac{\beta\tau}{2}\int_0^D \mathrm{d}z\, h'(z)^2. \tag{2.28}$$

Time has been replaced by the string's arc length variable z, position by the height field h, and mass by the inverse length $\beta\tau$. For continuity with the semi-flexible polymer partition function I will outline the calculation in terms of the string system instead of the free particle. As mentioned, the basic approach Feynmann introduced was to split the interval D into $N+1$ slices of width ϵ such that $(N+1)\epsilon = D$. Supposing straight line paths between the different slices, the spatial derivative may be replaced by $h'(z) \approx (h(z_{i+1}) - h(z_i))/\epsilon$. The integration over all paths requires integrating over each discrete height field $h_i \equiv h(z_i)$ independently , so that the measure becomes

$$\mathcal{D}h = \prod_{n=1}^{N} \int_{-\infty}^{\infty} \frac{dh_n}{\Delta h}, \tag{2.29}$$

where Δh is a constant with units of length necessary to make the measure dimensionless. Since it is constant it will supply an overall prefactor to the partition function which is independent of any system parameters, and thus will not contribute physically. It is now straightforward to evaluate this discretized path integral analytically since it is a product of coupled gaussian integrals. The result is

$$\mathcal{Z} = \frac{1}{\Delta h^N \sqrt{N}} \left(\frac{2\pi\epsilon}{\beta\tau}\right)^{\frac{N-1}{2}} \exp\left\{-\frac{(h_f - h_i)^2}{2D}\right\}, \tag{2.30}$$

where h_i and h_f are the initial and final heights of the filament, respectively. We immediately come across a serious issue: There is no well defined continuum ($\epsilon \to 0$) limit to this expression! The source of the divergence is the dependence of the derivative on the slicing procedure, which couples adjacent slices. While it's possible to call upon the correspondence with the quantum mechanical free particle and invoke normalization arguments, it is more instructive for the purpose of this thesis to introduce a more general method suggested by Kleinert [Kle86]. The resolution is to evaluate an equivalent *canonical* path integral written in terms of the phase space variables q and p. To do so I introduce an auxiliary functional which is the Legendre transform of Eq. 2.28. By all rights it should be called the Hamiltonian and be labeled $\mathcal{H}$, but as $\mathcal{H}$ typically represents configurational space energy functionals within soft mater physics I will call the new functional $\mathcal{L}$. The conjugate momentum is defined with an i for convenience, $p = i\frac{\delta\mathcal{H}}{\delta h'(z)} = i\beta\tau h'$ and the new functional is defined as

$$\mathcal{L}(h,p) = \mathcal{H} + \int \mathrm{d}z\, iph' = \int \mathrm{d}z\, \frac{p^2}{2\beta\tau}. \tag{2.31}$$

The functional $\mathcal{H}$ in terms of the conjugate variables is

$$\mathcal{H}(h,p) = \int \mathrm{d}z\, \frac{p^2}{2\beta\tau} - iph'. \tag{2.32}$$

The Legendre transforms have allowed us to write the energy functional in terms of two independent functions h and p. The path integral measure is now $\mathcal{D}h\mathcal{D}p$

and the time sliced version is unambiguous: it cannot depend on the short distance cutoff since the state of the string is determined by the entirely local functions h and p. We thus find

$$\mathcal{Z} = \prod_{n=1}^{N} \int_{-\infty}^{\infty} \frac{dh_n}{\Delta h} \int_{-\infty}^{\infty} \frac{dp_n}{2\pi\Delta p} \exp\left\{ -\sum_n \left[\frac{\epsilon p_n^2}{2\beta\tau} - ip_n(h_{n+1} - h_n) \right] \right\}. \tag{2.33}$$

We may relate this to the original naïve form Eq. 2.27 by integrating out the momentum degrees of freedom to find

$$\mathcal{Z} = \prod_{n=1}^{N} \int_{-\infty}^{\infty} \frac{dh_n}{\Delta h} \sqrt{\frac{\beta\tau}{2\pi\epsilon\Delta p^2}} \exp\left\{ -\sum_n \left(\frac{\beta\tau}{2} \frac{(h_{n+1} - n_i)^2}{\epsilon} \right) \right\}, \tag{2.34}$$

which is identical to Eq. 2.27 except for an additional piece Feynmann called a *measure factor*. In his treatment this served as a fudge factor to allow for finite evaluations of path integrals, but we see that it can in fact be derived and emerges naturally in the canonical treatment of the problem. It is easy to check that this measure factor produces the ϵ dependence to precisely cancel the divergent portion of Eq. 2.30 and we arrive at an answer which is well defined in the continuum limit

$$\mathcal{Z} = \frac{1}{\Delta h^N \Delta p^N} \left(\frac{\beta\tau}{2\pi D} \right)^{\frac{1}{2}} \exp\left\{ -\frac{(h_f - h_i)^2}{2\Delta h D} \right\}, \tag{2.35}$$

which was the original aim. Note that for fixed $h_f = h_i = 0$, which may always be accomplished by a simple rotation of the system, we predict that the partition function depends on the length of the string as $\mathcal{Z} \propto D^{-1/2}$, and thus the free energy is

$$\mathcal{F} = \frac{T}{2} \log D. \tag{2.36}$$

We find that there is a fluctuation induced Casimir interaction between pinning sites on the string, with the force going as $T/2D$. This form carries over to the semi-flexible polymer system, although with a different, cross-linker dependent prefactor.

2.2.2.5 Fluctuation factor of the semi-flexible polymer

We now return to the evaluation of the semi-flexible polymer fluctuation factor, Eq. 2.13. In the spirit of the previous section, we need to replace the Hamiltonian Eq. 2.12 with a canonical version which may be evaluated locally on each spatial slice. For notational convenience we will replace δh by h in this section. We first introduce an auxiliary field, $v(z) \equiv h'(z)$, and rewrite our Hamiltonian in terms of h, v, and v'. We add a Lagrange multiplier p_0 to ensure the correct relation between h' and v and define this new functional as

$$\tilde{\mathcal{H}}[h,v] = \int_0^d \mathrm{d}z \left\{ \frac{1}{2}\left[(v'(z))^2 + (q_1^2+q_2^2)(v(z))^2 + q_1^2 q_2^2 h^2(z)\right] - ip_0(h'-v) \right\} \quad (2.37)$$

The new Hamiltonian (2.37) is equivalent to (2.3) in that both produce the same equation for the classical configuration of the filament, found by setting $\frac{\delta\tilde{\mathcal{H}}}{\delta h} = \frac{\delta\tilde{\mathcal{H}}}{\delta v} = 0$. The advantage is that our Hamiltonian now depends only on first derivatives of h and v, at the expense of the Lagrange multiplier. We next introduce the variables p and p_v which are conjugate to h and v respectively:

$$\begin{aligned} p &= i\frac{\delta\tilde{\mathcal{H}}}{\delta h'(z)} = p_0 \\ p_v &= i\frac{\delta\tilde{\mathcal{H}}}{\delta v'(z)} = iv', \end{aligned} \quad (2.38)$$

and play the role of canonical momenta. An i has been included in the definition of p and p_v in order to make subsequent integrals convergent. We now define a new functional $\mathcal{L}$ as

$$\begin{aligned} \mathcal{L}(h,v,p,p_v) &= \int \mathrm{d}z\,(iph' + ip_v v') + \tilde{\mathcal{H}} \\ &= \int \mathrm{d}z \left[ipv + \frac{1}{2}\left(\frac{p_v^2}{2} + q^2 v^2\right)\right]. \end{aligned} \quad (2.39)$$

Our Hamiltonian (2.37) in terms of the new variables is

$$\begin{aligned}\mathcal{H}[h,v,p,p_v] &= \int \mathrm{d}z\,[-iph' - ip_v v'] + \mathcal{L} \\ &= \int \mathrm{d}z\left[-ip(h'-v) - ip_v v' + \frac{1}{2}\left(p_v^2 + q^2 v^2\right)\right]. \end{aligned} \tag{2.40}$$

The fluctuation factor is

$$\begin{aligned}\mathcal{Z}_{fl} = \int \mathcal{D}h\mathcal{D}v\mathcal{D}p\mathcal{D}p_v \times \\ \exp\left\{\int \mathrm{d}z\left[ip(h'-v) + ip_v v' - \frac{1}{2}\left(p_v^2 + q^2 v^2\right)\right]\right\}.\end{aligned} \tag{2.41}$$

If one were to drop the first two terms of the argument of the exponential, the functional integral would resemble the path integral expression of the density matrix of a quantum harmonic oscillator, with p_v playing the role of the canonical momentum. It should be kept in mind that in *classical* statistical mechanics momentum integration produces the partition function of the ideal gas. The variable p_v is only a mathematical aid and should not be viewed as a physical momentum variable.

To explicitly evaluate the functional integral, slice the spatial coordinate z into $N+1$ pieces of width ϵ such that $z_n = n\epsilon$ and $(N+1)\epsilon = D$. The boundary conditions translate into the requirements

$$\begin{aligned} h_0 &= 0 & \qquad h_{N+1} &= 0 \\ v_1 &= v_a & \qquad v_{N+1} &= v_b \end{aligned} \tag{2.42}$$

There are no boundary conditions imposed on p and p_v. A piecewise linear path is now defined by the values of (h_n, v_n, p_n, p_{v_n}) at each slice, with a straight line path in four-dimensional phase space interpolating between adjacent slices. Since the phase space coordinates are independent, we recover all possible paths by integrating over each variable at each slice. The measures $\mathcal{D}h, \mathcal{D}v, \mathcal{D}p,$ and$\mathcal{D}p_v$ in

the partition function are defined to be

$$\mathcal{D}h = \prod_{n=1}^{N} \int_{-\infty}^{\infty} \frac{\mathrm{d}h_n}{\Delta h} \qquad \mathcal{D}v = \prod_{n=2}^{N} \int_{-\infty}^{\infty} \frac{\mathrm{d}v_n}{\Delta v}$$
$$\mathcal{D}p = \prod_{n=1}^{N+1} \int_{-\infty}^{\infty} \frac{\mathrm{d}p_n}{2\pi\Delta p} \qquad \mathcal{D}p_v = \prod_{n=2}^{N+1} \int_{-\infty}^{\infty} \frac{\mathrm{d}p_{v_n}}{2\pi\Delta p_v} \tag{2.43}$$

The factors $\Delta h, \Delta v, \Delta p, \text{and} \Delta p_v$ are included in the definition of the elementary volume in the four-dimensional phase space to construct a partition function that is dimensionless, just as a factor with the dimensions of $\hbar^3$ must be included in the partition function of classical systems. The phase-space factors can be combined into the term $\Delta^{-N} = \Delta h^{-N} \Delta v^{-N+1} \Delta p^{-N-1} \Delta p_v^{-N}$.

All first order derivatives in the Hamiltonian can be discretized:

$$\tilde{\mathcal{H}} = \epsilon \sum_{n=1}^{N+1} \left[-ip_n \left(\frac{h_n - h_{n-1}}{\epsilon} - v_n \right) - ip_{v_n} \left(\frac{v_n - v_{n-1}}{\epsilon} \right) + \frac{1}{2} \left(p_{v_n}^2 + q^2 v_n^2 \right) \right] \tag{2.44}$$

First, perform the Gaussian integrals over p_{v_n}. This gives one factor $(2\pi\epsilon)^{-\frac{1}{2}}$ for every n and a term $\frac{1}{2}(\frac{v_n - v_{n-1}}{\epsilon})^2$ inside the square brackets. Next, perform the integrals over p_n. This produces one delta function $\delta(h_n - h_{n-1} - \epsilon v_n)$ for every n. Finally, the integrals over v_n combined with the delta function means replacing v_n by $\frac{h_n - h_{n-1}}{\epsilon}$. Finally, a factor of $1/\epsilon$ is generated by each of the $N-2$ integrals over v_n through the δ functions. The final result is

$$\mathcal{Z}_{fl} = \frac{1}{\epsilon^{\frac{3N}{2}-1}} \left[\prod_{n=1}^{N} \int_{-\infty}^{\infty} \frac{\mathrm{d}h_n}{\Delta} \right] \delta\left(h_N - \epsilon v_b\right) \delta\left(h_1 - \epsilon v_a\right) e^{-\mathcal{H}}, \tag{2.45}$$

where the Hamiltonian is given by

$$\mathcal{H} = \frac{\epsilon}{2} \sum_{n=1}^{N} \left[\left(\nabla \bar{\nabla} h_n \right)^2 + q^2 \left(\nabla h_n \right)^2 \right]. \tag{2.46}$$

Here, ∇ and $\bar{\nabla}$, are the forward and backward lattice derivatives:

$$\nabla h(z) = \frac{h(z+\epsilon) - h(z)}{\epsilon}$$
$$\bar{\nabla} h(z) = \frac{h(z) - h(z-\epsilon)}{\epsilon}. \tag{2.47}$$

Note that $h(z)$ in the functional integral is here allowed to have a slope at the end points that differs from the imposed boundary condition with the boundary condition enforced by the two delta functions. Furthermore, Eq. 2.45 implies that $\epsilon^{-3N/2+1}$ is the correct "measure factor" for the semi-flexible polymer Hamiltonian. To explicitly compute $\mathcal{Z}_{fl}$, it is convenient to leave the integral over p_1 and p_{N+1} in place. We begin by expanding the displacement in a sine series:

$$h(z) = \sqrt{\frac{2}{N+1}} \sum_{m=1}^{N} A_m \sin k_m z, \tag{2.48}$$

with $k_m = \frac{m\pi}{D}$. This decomposition differs from that of the naïve mode analysis in that the sine series imposes only the zero displacement boundary conditions $h_0 = h_{N+1} = 0$ at the ends, but does not constrain the angles there. The remaining boundary conditions on the angles are imposed afterwards through the integral over p_1 and p_{N+1}. The fluctuation Hamiltonian is

$$\mathcal{H}_{fl} = \frac{\epsilon}{2} \sum_{m=1}^{N} (Q_m^4 + Q_m^2 q^2) A_m^2. \tag{2.49}$$

Here

$$Q_m^2 \;=\; \frac{2 - 2\cos(k_m \epsilon)}{\epsilon^2} \tag{2.50}$$

is the mode dispersion relation of a linear chain. Eq. 2.48 is an orthogonal transformation with unit Jacobian. Finally, we express the height fields h_1 and h_N in $\exp\{ip_1 h_1 - ip_{N+1} h_N\}$ in terms of the sine series:

$$\begin{aligned} \exp\{ip_1 h_1 - ip_{N+1} h_N\} \;&=\; \exp\left\{ i\sqrt{\frac{2}{N+1}} \left[(p_1 - p_{N+1}) \sum_{m\,\mathrm{odd}}^{N} A_m \sin(k_m \epsilon) \right.\right. \\ &+ \left.\left. (p_1 + p_{N+1}) \sum_{m\,\mathrm{even}}^{N} A_m \sin(k_m \epsilon) \right] \right\}. \end{aligned} \tag{2.51}$$

The functional integral over the fluctuations, after the change of variables, is then

$$\begin{aligned}
\mathcal{Z}_{fl} &= \epsilon\Delta^{-N}\prod_{m=1}^{N}\left[\int_{-\infty}^{\infty}\frac{\mathrm{d}A_m}{\sqrt{2\pi\epsilon}\,\epsilon}\right]\int_{-\infty}^{\infty}\frac{\mathrm{d}p_1}{2\pi}\int_{-\infty}^{\infty}\frac{\mathrm{d}p_{N+1}}{2\pi} \\
&\times \exp\left\{i\sqrt{\frac{2}{N+1}}\left[(p_1-p_{N+1})\sum_{m\,\mathrm{odd}}^{N}A_m\sin(k_m\epsilon)\right.\right. \\
&+ \left.\left.(p_1+p_{N+1})\sum_{m\,\mathrm{even}}^{N}A_m\sin(k_m\epsilon)\right]\right\} \\
&\times \exp\left\{\frac{\epsilon}{2}\sum_{m=1}^{N}(Q_m^2+q^2)^2A_m^2\right\}. \qquad (2.52)
\end{aligned}$$

The integrals over the mode amplitudes A_m are Gaussian. Evaluation produces the product of a prefactor

$$\prod_{m=1}^{N}(\epsilon^2Q_m^2+\epsilon^2q^2)^{-1} \qquad (2.53)$$

that includes a factor $\frac{1}{\sqrt{2\pi\epsilon}\,\epsilon}$, and a piece which depends on p_1 and p_{N+1}:

$$\begin{aligned}
\int_{-\infty}^{\infty}\frac{\mathrm{d}p_1}{2\pi}\int_{-\infty}^{\infty}\frac{\mathrm{d}p_{N+1}}{2\pi}\exp\left\{-\frac{1}{(N+1)\epsilon}\left[(p_1-p_{N+1})^2\Sigma_o\right.\right. \\
\left.\left.+\,(p_1+p_{N+1})^2\Sigma_e\right]\right\}. \qquad (2.54)
\end{aligned}$$

where

$$\Sigma_o^e = \sum_{\substack{m\,\mathrm{even}\\ m\,\mathrm{odd}}}^{N}\frac{\sin^2(k_m\epsilon)}{(Q_m^2+q^2)^2}. \qquad (2.55)$$

The infinite product (Eq. 2.53) and the sums Σ_o^e can be evaluated in the limit $N\to\infty$ giving

$$\begin{aligned}
\Sigma_e &= \frac{\epsilon^2 D}{8q}\coth\left(\frac{qD}{2}\right) \\
\Sigma_o &= \frac{\epsilon^2 D}{8q}\tanh\left(\frac{qD}{2}\right)
\end{aligned} \qquad (2.56)$$

(see Refs. [Kle10] and [GR94]). The remaining momenta integrals (Eq. 2.54) are Gaussian. After evaluation and combination with Eq. 2.53, the fluctuation

contribution to the partition function is

$$\mathcal{Z}_{\rm fl} = \frac{1}{2\pi\Delta^N}\frac{q^2}{\sqrt{2(1-\cosh qD)+qD\sinh qD}}. \tag{2.57}$$

2.2.2.6 Partition function

The final result for the pinned semi-flexible polymer functional integral is found simply by multiplying the classical contribution with Eq. 2.57

$$\mathcal{Z} = e^{-\mathcal{H}_{cl}}\frac{1}{2\pi\Delta^N}\frac{q^2}{\sqrt{2(1-\cosh qD)+qD\sinh qD}}, \tag{2.58}$$

, where $\mathcal{H}_{cl}$ is given by Eq. 2.10. This function does *not* depend on the short distance cutoff and provides the appropriate statistical description of the filament in the continuum limit. In particular, it correctly extracts the fluctuation induced Casimir interaction valid at length scales much larger than the monomer size. This description will naturally fail, however, if one is interested in statistical properties of the polymer viewed as a chain of individual particles. In that limit, there is nothing unphysical about the dependence of the free energy on the microscopic cutoff. In fact, $-T\frac{\partial^2\mathcal{F}}{\partial T^2}$, where $\mathcal{F}$ is the Helmholtz free energy, must equal the Dulong-Petit heat capacity $\frac{N}{2}k_{\rm B}$ in the limit of large N according to classical statistical mechanics. To recover this result, one must reinsert the cutoff dependence into the partition function through the semi-flexible filament measure factor:

$$\mathcal{Z}_{discrete} = e^{-\mathcal{H}_{cl}}\frac{\epsilon}{2\pi(\epsilon^{3/2}\Delta)^N}\frac{q^2}{\sqrt{2(1-\cosh qD)+qD\sinh qD}}, \tag{2.59}$$

The free energy of the discrete polymer equals

$$\frac{\mathcal{F}}{k_{\rm B}T} = \mathcal{H}_{cl} - \ln\left(\frac{q^2}{\sqrt{2(1-\cosh qD)+qD\sinh qD}}\right) + N\ln\sqrt{\frac{\Delta^2\epsilon^3}{k_{\rm B}T}} - \ln(\epsilon/2\pi). \tag{2.60}$$

The first term, the classical Hamiltonian, is the elastic energy of the polymer in the absence of thermal fluctuations. It is, of course, independent of the microscopic cutoff. The second term is also independent of the short distance cutoff and it

will be the source of the Casimir force. The third term, which depends explicitly on the cutoff, is extensive in the number N of microscopic degrees of freedom and dominates in the large N limit. Now, the finite and divergent terms are cleanly segregated in the free energy: the dependence on the small distance cutoff – which stands for dependency on microscopic variables – only appears in the free energy per monomer. The third term (with the explicit temperature dependence restored) ensures that the Dulong-Petit relation holds even as ϵ is taken to zero.

2.2.3 A note on the importance of the embedding space

It is worth commenting that it is necessary for the cross-linkers to pin the polymer to an embedding space for the boundary conditions to make sense. In biological systems, this may be accomplished by pinning the filament to an otherwise static background elastic network. One can show that cross-linkers bound to an otherwise free filament will not experience an interaction. This is not immediately obvious because the cross-linkers will locally modify the mechanical properties of the polymer by making it stiffer, and these so called rigid inclusions have been shown to interact with one another in membrane systems. Nevertheless, I will show that polymers differ from their two dimensional cousins in this respect. Consider a free semiflexible filament fluctuating in the plane with two linkers attached. The Hamiltonian for the filament, parameterized by the angle of the local tangent with respect to a reference direction $\theta(s)$ as function of arc length, is given in the usual form,

$$\mathcal{H}\left(\{\theta(s)\}\right) = \frac{1}{2}\int_0^L \mathrm{d}s\,\kappa(s)\left(\frac{d\theta}{ds}\right)^2. \tag{2.61}$$

The role of the attached linkers is to modify the local bending stiffness of the filament $\kappa(s)$; the filament has one bending modulus at the linkers' locations and another elsewhere. The partition function for such a system may be written as

$$\mathcal{Z} = \int \mathcal{D}\theta\, e^{-\beta\mathcal{H}(\{\theta(s)\})}. \tag{2.62}$$

The above partition function is that of the one-dimensional nonlinear σ model, but with a nonuniform stiffness. The functional integration should respect the restriction of $\theta(s)$ to the unit circle: $0 \leq \theta < 2\pi$. In the case of interest where the entire chain segment is much shorter than a persistence length, the partition sum is dominated by a small range of tangent angles so that this constraint can neglected. Having done so, we perform the functional integral over $\theta(s)$ treating it as a Gaussian variable. In the non-linear sigma model, this is known as the spin-wave approximation. Discretizing the functional integral again in chain segments of length ϵ, and assuming periodic boundary conditions, we obtain

$$\mathcal{Z} = \left[\prod_{n=1}^{N} \int_{-\infty}^{\infty} \frac{\mathrm{d}\theta_n}{\Delta}\right] \exp\left\{-\frac{1}{2\epsilon} \sum_{n=1}^{N} \beta\kappa_n \left(\theta_{n+1} - \theta_n\right)^2\right\}, \tag{2.63}$$

with $\theta_{N+1} = \theta_1$. Since there are no higher-order derivatives, there are no ambiguities of the kind previously discussed in the evaluation of the functional integral. Introducing the difference variable $y_n = \theta_{n+1} - \theta_n$ and performing the Gaussian integrals we arrive at

$$\mathcal{Z} \propto \prod_{n=1}^{N} \frac{1}{\sqrt{\beta\kappa_n}}. \tag{2.64}$$

It is evident from this expression that the partition function does *not* depend on the separation of the two beads on the filament because the product is insensitive to the ordering of the κ_i. There is no fluctuation-mediated interaction between the beads within the spin-wave approximation. To generate a fluctuation force it is necessary to place the system in an embedding space where displacement and slope boundary conditions are meaningful quantities.

2.3 Cross-Linker Interaction Potential

We can now use the results of the previous section to infer the effective interaction between transient cross-linking molecules. We start with the case of zero tension

where the partition function Eq. 2.58 reduces to

$$\mathcal{Z} = \frac{C}{D^2} e^{-\frac{2}{D}\left(v_a^2 + v_b^2 + v_a v_b\right)}, \tag{2.65}$$

where C is a constant which is independent of D and the boundary conditions, and thus plays no role in the Casimir force. The free energy, modulo this overall constant, is

$$\begin{aligned} \mathcal{F} &= -k_{\mathrm{B}} T \log \mathcal{Z} \\ &= k_{\mathrm{B}} T \left(2 \log \tilde{D} + \frac{2}{\tilde{D}} \left(\tilde{v}_a^2 + \tilde{v}_b^2 + \tilde{v}_a \tilde{v}_b \right) \right). \end{aligned} \tag{2.66}$$

The tildes have been reinserted here as a reminder: $\tilde{D} = l_p^{-\frac{1}{3}} D, \tilde{v} = l_p^{\frac{1}{3}} v$. The force between the linkers is computed, as before, by connecting the ends of the chain into a loop of length L and computing the derivative of the total energy with respect to D. This produces

$$f(D) \approx -\frac{2 k_B T}{D} + 2\kappa \frac{v_a^2 + v_b^2 + v_a v_b}{D^2}. \tag{2.67}$$

assuming again $L \gg D$. The first term has the form of the Casimir interaction that we obtained earlier. The second term is the elastic energy of the section of the chain between the linkers. The combined expression has a stable minimum at $f(D^*) = 0$ with a separation $D^* = l_p(v_a^2 + v_b^2 + v_a v_b)$ that is of the order of the persistence length. Figure 2.5 shows the Casimir force for different fixed values of the slopes.

The attractive Casimir interaction has a universal character: it is independent of both the small distance cutoff and the persistence length, although the persistence length partially determines the validity of the perfect pinning boundary condition–See Sec. 2.3.5. To estimate the magnitude of this force in typical biopolymer systems, we note that a separation of a ten nanometers, the attractive force is on the order picoNewtons, the typical force scale of motor proteins. The work required to separate the two cross links from 100nm to one micron is $\sim 9 k_{\mathrm{B}} T$.

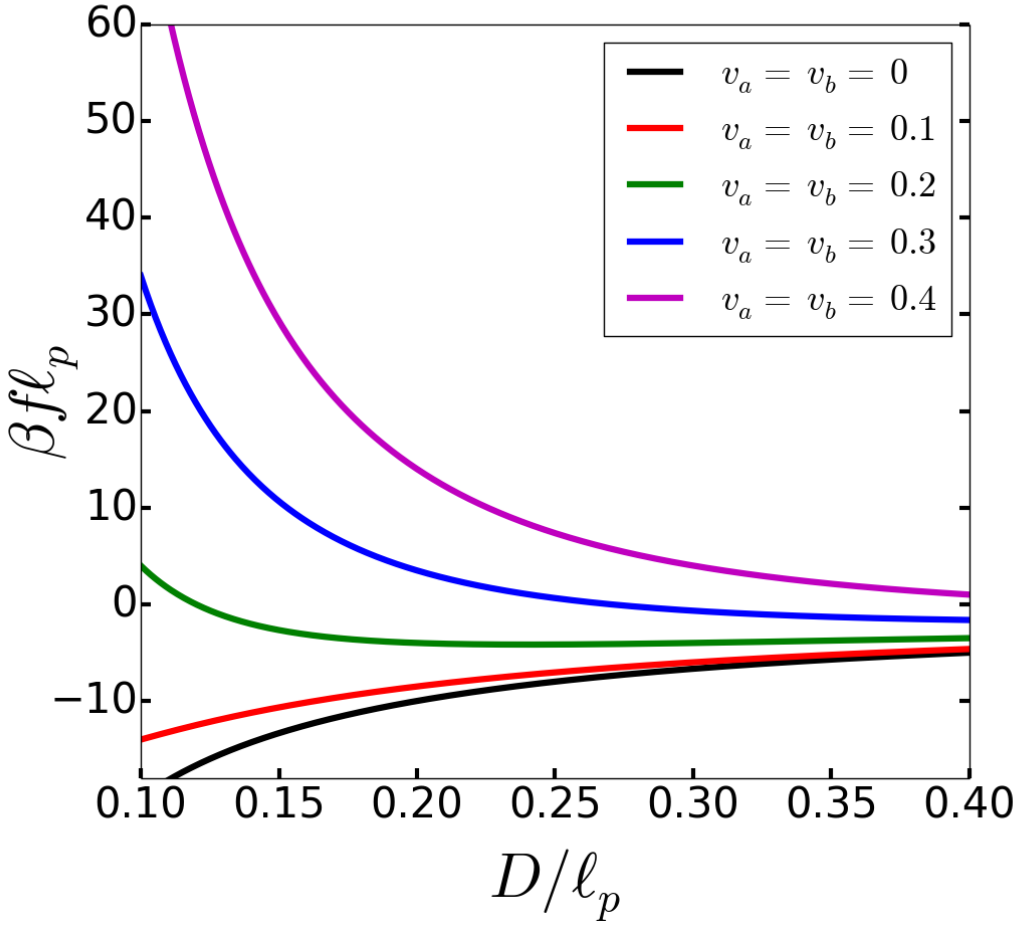

Figure 2.5: The Casimir force for cross-linkers which fix the slope of the filament. At small distances the repulsive elastic interaction always overwhelms the attractive fluctuation force.

One must now specify how the transient cross-linker molecules impose angular restrictions on the filaments to which they are bound. There are two particular cases of interest related to cross linked F-actin networks. Some linkers that promote filament bundling, such as α-actinin, have a strong preference for parallel filaments, but others, such as the network-forming filamin cross linkers do not appear to generate strong angular constraints. It is simple to examine both cases if the linker molecules apply a *harmonic* restoring torque on the two filaments towards parallel alignment. In that case, two final Gaussian integrals remain to be done to perform a thermal average of the classical partition function over different linker angles:

$$\begin{aligned} \mathcal{Z}_{\rm cl} &= \int_{-\infty}^{\infty} \frac{{\rm d}v_a}{\Delta v_a}\frac{{\rm d}v_b}{\Delta v_b} \exp\left\{-\frac{2l_p}{D}\left(v_a^2+v_b^2+v_a v_b\right)\right\} \\ &\quad \times \exp\left\{-\frac{\beta\gamma}{2}\left(v_a^2+v_b^2\right)\right\}, \end{aligned} \tag{2.68}$$

where γ is a measure of the angular rigidity of the linker. The associated free energy is

$$\frac{\mathcal{F}_{cl}(D)}{k_{\rm B}T} = \frac{1}{2}\log\left[\frac{1}{2}(l_p/D)^2\left(12+8\beta\gamma D/l_p+(\beta\gamma D/l_p)^2\right)\right]$$

This expression must replace the second term in Eq. 2.66. We will examine this expression in the limits of weak and strong angular stiffness in the following sections.

2.3.1 Network Linkers

For the case that the linker molecule have little or no angular preference, we take the limit of $\beta\gamma \ll l_p/D$ and find the total force to be

$$f(D) \approx -\frac{k_B T}{D}. \tag{2.69}$$

The thermal average over the repulsive "classical" interaction simply cancelled one half of the Casimir force. The net force remains attractive as long as $\beta\gamma \ll l_p/D$.

For very large separations, this condition fails. The attraction starts to increase even more and is better described by the opposite limit of bundling linkers, which have a strong angular preference. Relaxing the angle condition in going from the result given by Eq. 2.67 to the one given by Eq. 2.69 removes precisely half of the interaction strength. One may view the attraction in Eq. 2.67 as arising in equal parts from the restriction of two separate degrees of freedom, the position and slopes of the filament at the pinning sites. Alternatively, if one were to consider the unphysical case of cross linkers which pin the slopes but not the positions of the filaments, one should expect the same result as in Eq. 2.69. More importantly, one may consider the case of cross linkers with no angular preference and some intrinsic elastic compliance, modeled by a harmonic spring with spring constant k. Based on our results for the cross linkers that generate a harmonic potential with curvature γ for the filament slope, we expect that the prefactor of unity in Eq. 2.69 would be reduced monotonically for elastically compliant cross linkers, and go to zero as $k \to 0$.

2.3.2 Bundling linkers

For the case that the linker molecule have a strong angular preference for parallel alignment, we should take the opposite limit of $\beta\gamma >> l_p/D$. This gives

$$f(D) \approx -2\frac{k_B T}{D}(1 - 2\frac{k_{\rm B} T l_p}{\gamma D} + ...) \tag{2.70}$$

for the total force–Please see Fig. 2.6 for plots with different values of γ. The repulsive interaction amounts to a small reduction of the Casimir force. The Casimir force is thus roughly twice stronger for bundle linkers than for network linkers. In the limit $\gamma \to \infty$ the final result for the Casimir force obtained from the correct evaluation of the path integral is identical to that obtained by the naïve approach and subtraction scheme discussed in section IIB. The naïve approach to the calculation of the free energy of the pinned filament introduces errors in its

dependence upon the small distance cutoff ϵ. However, by taking a derivative with respect to the inter cross linker spacing and subtracting the remaining formally divergent part of the resultant force as described after Eq. 2.19, one can mask the deficiencies of the naïve approach. Other derivatives of the free energy, such as the specific heat, still retain the unphysical dependence of the naïve free energy upon ϵ, as discussed after Eq. 2.60.

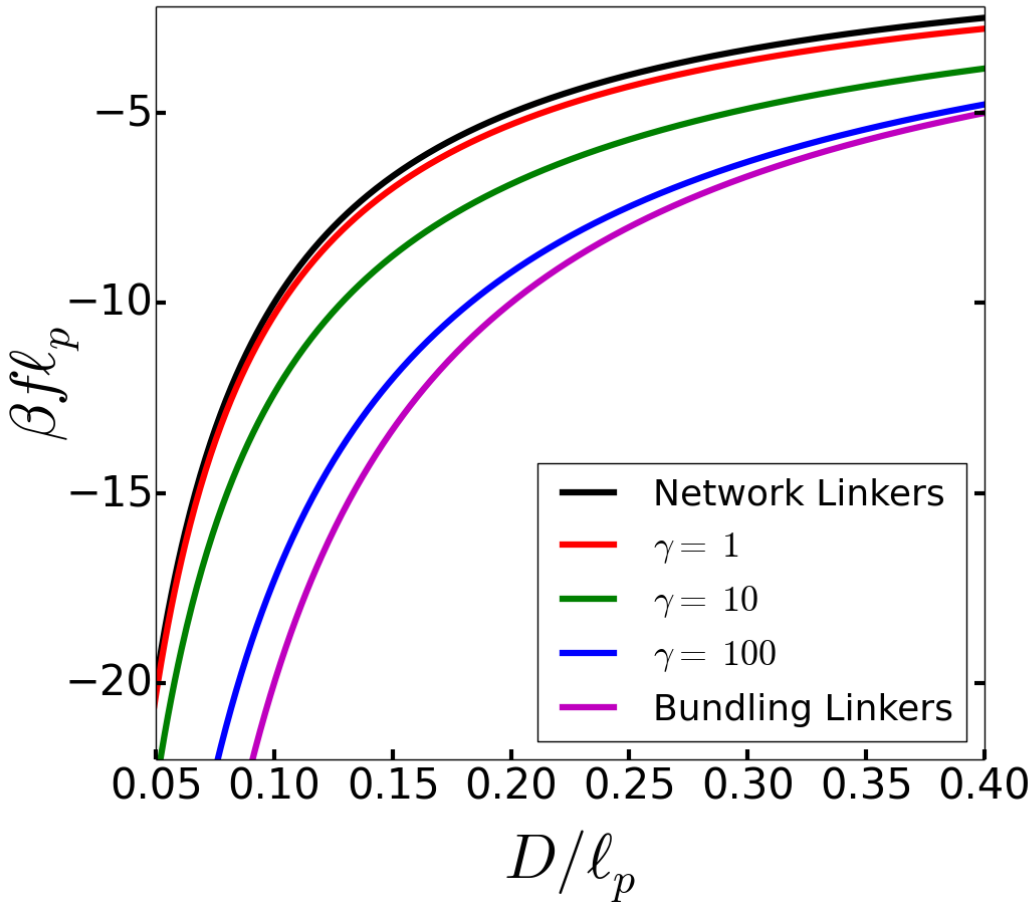

Figure 2.6: As the angular stiffness γ is increased the Casimir force transitions from a network cross-linker into one which prefers bundling filaments.

2.3.3 The effect of tension

Next, consider the case of nonzero filament tension. Rewriting the earlier results in terms of the unscaled variables, introducing the dimensionless quantity $d \equiv \sqrt{\frac{\beta\tau}{l_p}}D = \sqrt{\frac{\tau}{\kappa}}D$, and further setting the slopes $v_a = v_b = 0$ to focus on the fluctuation contribution ($\mathcal{H}_{cl} = 0$), we find the free energy

$$\mathcal{F} = -k_{\mathrm{B}}T\left[\log\left(\frac{1}{D^2}\right) + \log\left(W(d)\right)\right] + C, \tag{2.71}$$

where

$$W(d) = \frac{d^2}{\sqrt{2(1-\cosh(d)) + d\sinh(d)}} \tag{2.72}$$

is a scale function. The function $f(d)$ contains the entire correction to the free energy due to tension, which enters only through the length $\sqrt{\frac{\kappa}{\tau}}$. The force between the two linker molecules, obtained as before, is

$$f(D) = k_{\mathrm{B}}T\left(-\frac{2}{D} + \sqrt{\frac{\tau}{\kappa}}\left(\frac{W'(d)}{W(d)} + \frac{1}{2}\right)\right). \tag{2.73}$$

The factor $1/2$ in the second term is the contribution to the force due to filament fluctuations of chain material that is not between the two linkers. The second term is strictly positive so that the inclusion of tension weakens fluctuation attraction. For $d \gg 1$, $\frac{W'(d)}{W(d)} \approx -\frac{1}{2} + \frac{3}{2d}$. In that case, the total force is $f(D) \approx -k_{\mathrm{B}}T\frac{1}{2D}$. The tension-induced fluctuation repulsion thus cancels $3/2$ of the tension-free Casimir force. Figure 2.7 shows resulting force for different values of d.

For $d \ll 1$ on the other hand, the second term contributes a repulsive force that is independent of D and equal to $\frac{k_{\mathrm{B}}T}{2}\sqrt{\frac{\beta\tau}{l_p}}$ but this is small compared to the tension-free fluctuation attraction. For distances small compared to the "tension scale" $1/q$ the full Casimir attraction is recovered. In summary, the Casimir force is not suppressed by tension for the case of bundle linkers with strongly preferred alignment. If slope fluctuations are included one finds a reduction of $k_{\mathrm{B}}T\frac{1}{D}$ in the attractive force for $d << 1$ again illustrating that tension has no effect for distances less than the tension scale. For large distances the slope fluctuations

are strongly suppressed and do not weaken the Casimir attraction. We plot the Casimir force between cross linkers of the bundling and network types and explore the effect of tension applied to the filament in Fig. 2.8.

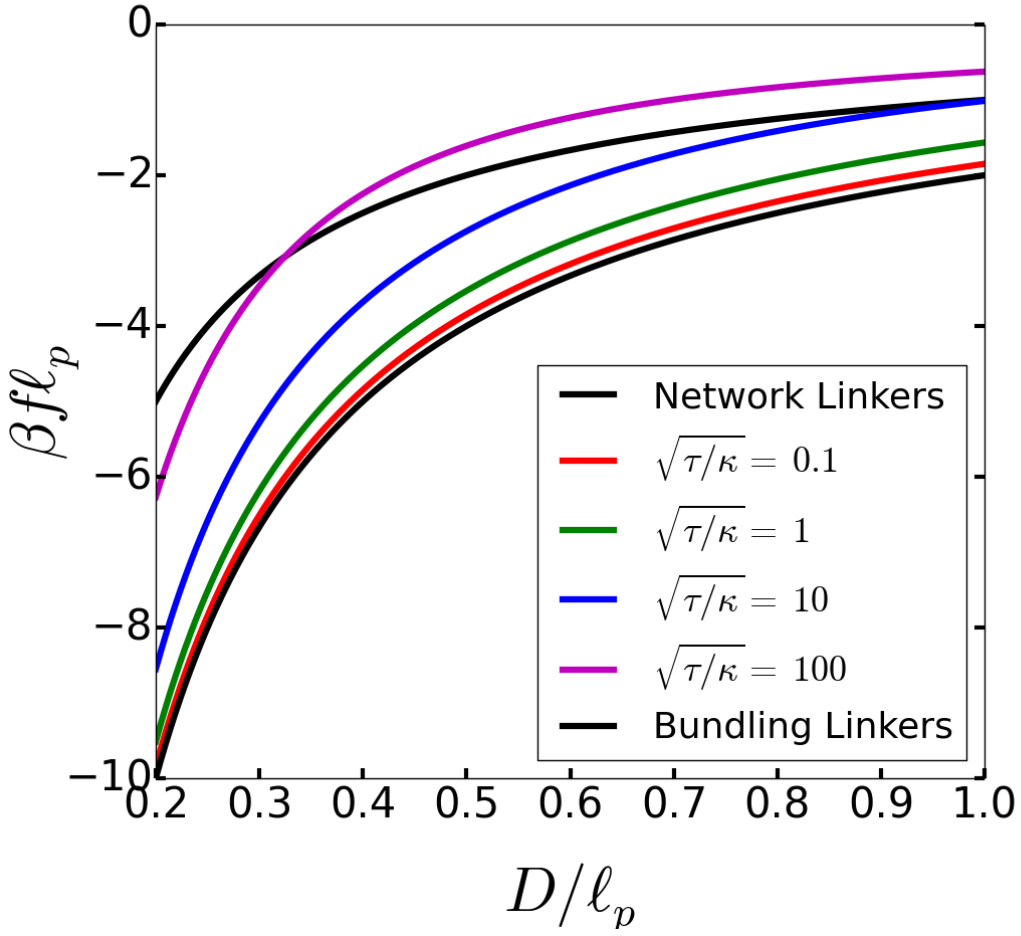

Figure 2.7: For separations greater than the characteristic tension length scale $\sqrt{\kappa/\tau}$ the Casimir force is weakened. At small separations, neglecting any elastic repulsion due to preferred tangent angles, all curves with finite tension collapse onto the bundling linker result.

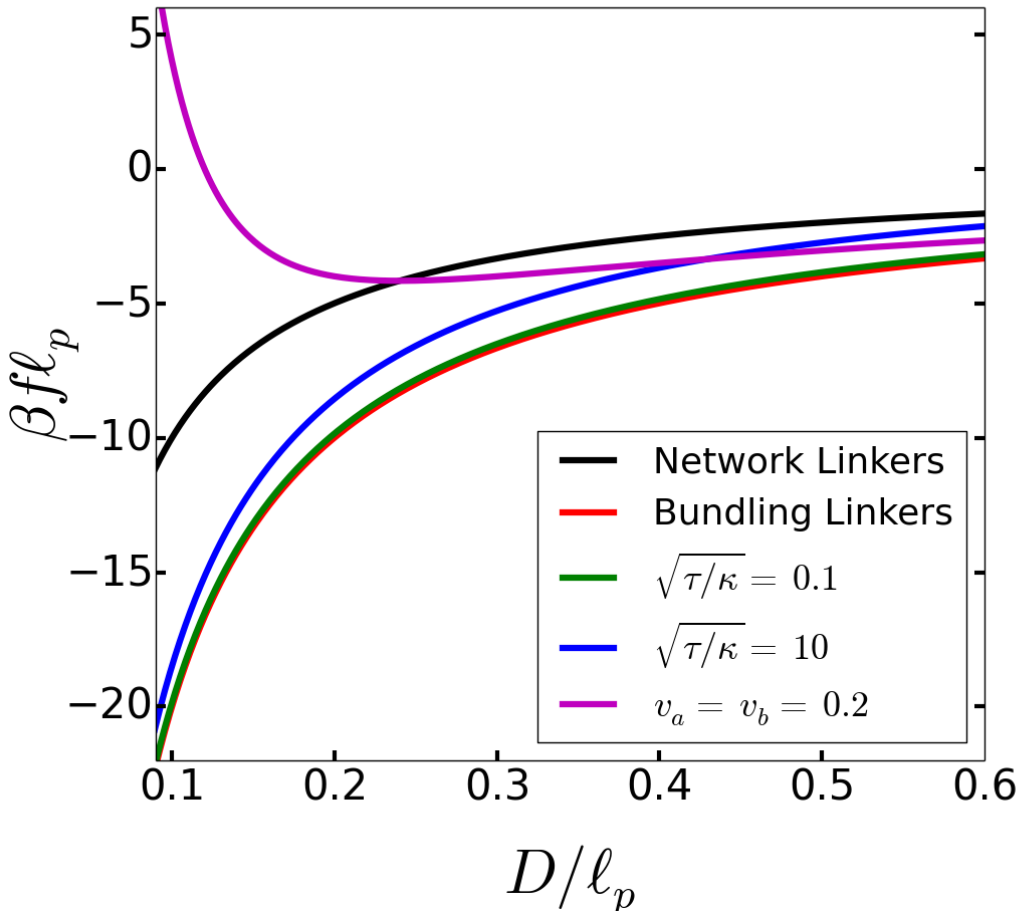

Figure 2.8: The Casimir force versus cross linker separation for a filament fluctuating in one transverse dimension. We compare the interaction in the tension-free case for *network cross linkers*, which do not constrain the filament crossing angles (black), and angle-constraining *bundle cross linkers* (red) with zero preferred slope. When the bundle cross linkers enforce filament slopes that introduce a nonzero mean torque (magenta), the interaction becomes repulsive at short distances due to the forced bending of the filament. The effect of finite tension is explored for the case of fixed tangent angles of zero at the cross links. Increased tension reduces the attractive interaction at lengths greater than $\sqrt{\kappa/\tau}$, as can be seen by comparing the low tension (green) and high tension (blue) results.

2.3.4 Three cross-linker interaction

Consider three sliding linkers on a fluctuating filament as shown in Fig. 2.9. The classical and Casimir contributions to the free energy in a tensionless filament in the scaled units are

$$\mathcal{F} = 2k_{\mathrm{B}}T\left(\log\tilde{D} + \log(\tilde{L}-\tilde{D}) + \frac{\tilde{v}_a^2+\tilde{v}_b^2+\tilde{v}_a\tilde{v}_b}{\tilde{D}} + \frac{\tilde{v}_b^2+\tilde{v}_c^2+\tilde{v}_b\tilde{v}_c}{\tilde{L}-\tilde{D}}\right), \qquad (2.74)$$

If one assumes the linkers have no angular preference then the $\tilde{v}_i$ may be integrated

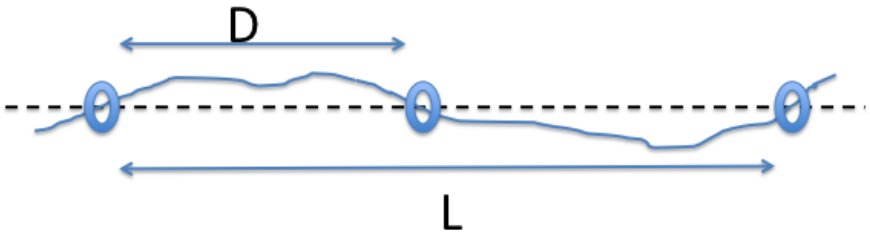

Figure 2.9: Three interacting sliding linkers on a single fluctuating filament

out and one finds the interaction free energy

$$\mathcal{F} = k_{\mathrm{B}}T\left(\log\tilde{D} + \log(\tilde{L}-\tilde{D}) + \frac{1}{2}\log\tilde{L}\right) \qquad (2.75)$$

The Casimir force on the middle linker is

$$f = -k_{\mathrm{B}}T\left(\frac{1}{D} - \frac{1}{(L-D)}\right) \qquad (2.76)$$

The force on the leftmost linker is

$$f = -k_{\mathrm{B}}T\left(\frac{1}{D} + \frac{1}{2L}\right) \qquad (2.77)$$

As we let $D \to L$ corresponding to a single linker interacting with a cluster of two linkers we see the force goes to $-\frac{3k_{\mathrm{B}}T}{2\tilde{L}}$. This result highlights the fact that tight clusters must eliminate fluctuations and therefore force the slopes to be identically zero at the edges of the cluster. Fluctuating slopes generate repulsive forces of strength $-\frac{k_{\mathrm{B}}T}{2\tilde{L}}$ so the elimination of such fluctuations increases the overall strength of the attraction. We see that an individual linker will be preferentially attracted to clusters over solitary linkers. This result holds for the interaction of a single linker with any size cluster up to correction of order $\frac{a}{L}$, where a is the mean spacing within a cluster and L is the separation of the single linker with the cluster. We may also deduce that two clusters will interact with the full fluctuation force $-\frac{2k_{\mathrm{B}}T}{\tilde{L}}$ since there are no slope fluctuations at either end.

2.3.5 Applicability to Biological Systems

For the Casimir effect to be operative between two physical cross linkers, one must be sure that the scale of transverse undulations at a location on the filament without a cross linker is *larger* than the ring radius. Larger rings would have no effect on the filament's fluctuation spectrum and thus generate no Casimir interaction.

The magnitude of the thermally generated undulations is easily estimated. For simplicity tension is neglected and only one transverse direction is considered so that the energy of a given configuration is given by

$$\mathcal{H} = \frac{\kappa}{2}\int_0^D \mathrm{d}z\,[h''(z)]^2. \tag{2.78}$$

The boundary conditions are chosen to represent a bound linker restricting fluctuations at $z = 0$, specifically hinged at $z = 0$ and free at $z = D$, i.e. $h(0) = h'(0) = 0$ and $h''(D) = h'''(D) = 0$, where primes denote differentiation with respect to z. The aim is to determine the characteristic fluctuations a distance

l from $z = 0$ and compare this with the relevant cross linker length scales. For these boundary conditions we may integrate by parts with no surface terms to find

$$\mathcal{H} = \frac{\kappa}{2} \int_0^D \mathrm{d}z \, h \, \partial_z^4 h. \tag{2.79}$$

To determine the thermal expectation value of the filament's transverse displacement at $z = l$ it is convenient to decompose those displacements into eigenfunctions of the ∂_z^4 operator with the boundary conditions imposed above. The appropriate eigenfunctions are

$$h_n = c_n \left[\sin(k_n z) + \frac{\sin(k_n D)}{\sinh(k_n D)} \sinh(k_n z) \right], \tag{2.80}$$

with corresponding eigenvalues k_n^4, where k_n are the solutions of the transcendental equation

$$\tan(k_n D) = \tanh(k_n D), \tag{2.81}$$

and c_n is a normalization constant chosen so that

$$\int_0^D \mathrm{d}z \, h_n^2(z) = 1. \tag{2.82}$$

The analysis is further simplified by considering only the first mode, $n = 1$. Since the mean square amplitudes of each mode are positive definite quantities that add to the quantity of interest $\langle h^2(l) \rangle$, this result provides a conservative *underestimate* of the rms fluctuations of the filament. From the equipartition theorem

$$\frac{\kappa}{2} \langle A_1^2 \rangle k_1^4 = \frac{k_\mathrm{B} T}{2}, \tag{2.83}$$

where A_1 is the amplitude of the first mode. The local height fluctuations are then given by

$$\langle h^2(l) \rangle = \frac{k_\mathrm{B} T}{\kappa k_1^4(D)} h_1^2(l; D) \ + \cdots, \tag{2.84}$$

where we note explicitly the dependence of the eigenfunction and eigenvalue on the filament's length D. The ellipses represent positive terms associated with the neglected modes. The eigenfunction scales as $h_1(l; D) \sim D^{-1/2} k_1 l$ due to the

normalization factor c_1 of the eigenfunction and its dependence on l for small l. The eigenvalues scale as $k_1 \sim D^{-1}$, so $h_1(l;D) \sim L^{-3/2}l$. Combining this with Eq. 2.84 and recalling that $l_p = \kappa/k_{\mathrm{B}}T$, one finds

$$\langle h^2(l)\rangle \sim \frac{l^2 D}{l_p}. \tag{2.85}$$

The rms fluctuations are then estimated to be $\sqrt{\langle h^2(l)\rangle} \sim l\sqrt{D/l_p}$. To put this in a biological context imagine that the filament is a 1μm F-Actin polymer, which has $l_p \sim 10\mu$m), and has characteristic transverse fluctuations

$$\sqrt{\langle h^2(l)\rangle} = .1l. \tag{2.86}$$

At a separation of $l = 100$nm the fluctuations are approximately 10nm. If one imagines that the hinged boundary condition at $z = 0$ is due to a cross linker with no angular preference then the perfect pinning approximation should be reasonable at a separation of 100nm since a physical cross linker should be capable of constraining fluctuations of order 10 nm. Assuming cross linkers can affect fluctuations on the scale of 1nm, one arrives at an estimate of 10nm for the lower bound of validity of the approximation. This result is somewhat sensitive to boundary conditions: A clamped boundary condition at $z = 0$ leads to a quadratic growth profile and would produce fluctuations of only a few nm at $l = 100$nm, and thus the approximation is only appropriate beyond that distance.

2.4 Evidence of Casimir effect from simulations

The existence of a Casimir force between cross-linkers is verified by numerical simulation of a pinned semi-flexible filament. The simulation free energy as a function of pinning site separation is difficult to measure precisely because of the macroscopic number of degrees of freedom in the system, each contributing $k_{\mathrm{B}}T$ to the total. One may easily measure the Fourier mode amplitudes, however, and compare them to a theoretical model that is equivalent to the Casimir interaction

previously derived. In Sec 2.4.1 I present the new calculation and prove the equivalence. Section 2.4.2 outlines the simulation method, and the results are stated and discussed in Sec. 2.4.3.

2.4.1 The Casimir force as a linear Fourier mode coupling

The derivation of the Casimir force in Sec. 2.2 is a direct evaluation of the partition function expressed as a path integral

$$\mathcal{Z} = \int \mathcal{D}h\, e^{-\beta \mathcal{H}[h]}, \tag{2.87}$$

where the Hamiltonian $\mathcal{H}$ is given by Eq. 2.2. The naïve approach (c.f. Sec. 2.2.2.2) represents the height field in terms of Fourier modes which enforce an $h = 0$ boundary condition at $z = 0, L$

$$h(z) = \sqrt{\frac{2}{N+1}} \sum_{n=1}^{N} A_n \sin k_n z, \tag{2.88}$$

where $k_n = \frac{n\pi}{L}$, and N is the number of included modes which will be subsequently taken to infinity. The boundary conditions represent network cross-linkers (see Sec. 2.3.1) because the initial and final tangents are thermally averaged. This transformation diagonalizes the Hamiltonian and also allows a simple form for the path integral measure(up to a multiplicative constant) $\mathcal{D}h$:

$$\begin{aligned} \mathcal{D}h &\rightarrow \prod_{n=1}^{N} \int \mathrm{d}A_n \\ \mathcal{H} &\rightarrow \frac{\kappa}{2} \sum_{n=1}^{N} k_n^4 A_n^2 + \frac{\tau}{2} \sum_{n=1}^{N} k_n^2 A_n^2, \end{aligned} \tag{2.89}$$

This method introduces the divergences discussed in 2.2.2.2 if one attempts to directly calculate the interaction between *two* crosslinkers. The divergences are due to the transfer of degrees of freedom into the bulk region of the filament outside the linkers, but this can be avoided with the introduction of a *third* linker between the original two, as shown in Fig. 2.10. It will be shown that there are no

divergences associated with the change in free energy as the middle linker is slid between the outer linkers, and that this naïve approach reproduces the Casimir interaction as well as the desired Fourier amplitude matrices. Instead of restricting ourselves to a single intermediate crosslinker we allow m linkers at positions $z = D_i$ which constrain the fluctuations and force $h(D_i) = 0$. This pinning condition is handled with a product of Dirac δ functions $\delta(h(D_1))\,\delta(h(D_2))\cdots$ written in Fourier space. The final form of the partition function is

$$\begin{aligned}\mathcal{Z} &= \prod_{n=1}^{N}\int \mathrm{d}A_n \int_{-\infty}^{\infty}\frac{\mathrm{d}p_1}{2\pi}\cdots\int_{-\infty}^{\infty}\frac{\mathrm{d}p_m}{2\pi}\exp\{-\beta\mathcal{H} \\ &+ ip_1\sum_{n=1}^{N}A_n sin\, k_n D_1 + \cdots + ip_m\sum_{n=1}^{N}A_n sin\, k_n D_m\Bigg\}. \end{aligned} \tag{2.90}$$

The integral is straightforward to evaluate since it is a product of Gaussian integrals, although there is complexity associated with a large number of additional crosslinkers. It is also clear that the Casimir interaction involves only a linear coupling between all the modes. For simplicity let $\tau = 0$ and consider only a single intermediate linker at $z = D$. Completing the square for each amplitude and performing the resulting Gaussian integrals gives

$$\mathcal{Z}(D) = \left[\prod_{n=1}^{N}\sqrt{\frac{2\pi}{\beta\kappa k_n^4}}\right]\int\frac{\mathrm{d}p}{2\pi}\exp\left\{-\left[\sum_{n=1}^{N}\frac{\sin^2 k_n D}{2\beta\kappa k_n^4}\right]p^2\right\}. \tag{2.91}$$

The prefactor diverges as $N \to \infty$, however it is independent of D and can be ignored since it will not contribute to the Casimir force. Up to a constant we thus have

$$\mathcal{Z}(D) \propto \left(\sum_{n=1}^{N}\frac{\sin^2 k_n D}{2\beta\kappa k_n^4}\right)^{-1/2}. \tag{2.92}$$

It's interesting to note that $\mathcal{Z}(D=0)$ differs from the partition function with no constraint by an infinite multiplicative constant. This of course must be the case if there is to be a Casimir force. Continuing, we obtain the free energy

$$\mathcal{F}(D) = \frac{T}{2}\log\left(\sum_{n=1}^{N}\frac{\sin^2 k_n D}{2\beta\kappa k_n^4}\right), \tag{2.93}$$

and the force

$$f(D) = -\frac{T}{2}\left(\sum_{n=1}^{N}\frac{\sin^2 k_n D}{k_n^4}\right)^{-1}\left(\sum_{n=1}^{N}\frac{2k_n \sin k_n D\cos k_n D}{k_n^4}\right). \tag{2.94}$$

Setting the length of the filament to unity we are left with

$$f(D) = -\pi T\left(\sum_{n=1}^{N}\frac{\sin^2 n\pi D}{n^4}\right)^{-1}\left(\sum_{n=1}^{N}\frac{\sin n\pi D\cos n\pi D}{n^3}\right). \tag{2.95}$$

The sums converge and we may safely take the limit $N \to \infty$. The result,

$$f(D) = \pi\, T\,\mathrm{Im}\left[\frac{\mathrm{Li}_3(e^{\imath 2\pi D}) - \mathrm{Li}_3(e^{-\imath 2\pi D})}{\mathrm{Li}_4(e^{\imath 2\pi D}) + \mathrm{Li}_4(e^{\imath 2\pi D}) - 2\mathrm{Li}_4(1)}\right], \tag{2.96}$$

is equivalent to the force calculated using the 3 body Casimir interaction, Eq. 2.76 (recalling $L = 1$):

$$f(D) = -T\left(\frac{1}{D} - \frac{1}{1-D}\right). \tag{2.97}$$

To calculate mode amplitude correlations it is convenient to turn the partition function into a generating function $\mathcal{Z}(\mathbf{J})$ by including a source term $\sum A_i J_i$ in the exponent of Eq. 2.90. Correlation functions are now simple to calculate, for example the two point function takes the form

$$\langle A_i A_j\rangle = \frac{\left.\frac{\partial \mathcal{Z}}{\partial J_i \partial J_j}\right|_{J=0}}{\mathcal{Z}(J=0)}. \tag{2.98}$$

The integrals are easily evaluated, and explicitly in the case $m = 1$ we find the correlation function

$$\langle A_i A_j\rangle(D) = \frac{\delta_{i,j}}{\beta(\kappa k_i^4 + \tau k_i^2)} - \frac{\frac{\sin k_i D}{\kappa k_i^4+\tau k_i^2}\frac{\sin k_j D}{\kappa k_j^4+\tau k_j^2}}{\beta\sum_{n=1}^{N}\frac{\sin^2 k_n D}{\kappa k_n^4+\tau k_m^2}}. \tag{2.99}$$

If $D = 0$ or $D = L$, representing the intermediate linker positioned at either edge, the standard equipartition result emerges. Apart from those two cases, the pinning condition modifies the shape and eigenvalues of the normal modes of the filament. This linear coupling of the Fourier modes completely defines the Casimir

interaction. The simulations will also study the case $m = 2$ and I quote the result here for the case of zero tension, $\tau = 0$, and two pinning sites at D_1 and D_2

$$\begin{aligned}
\langle A_i A_j \rangle (D_1, D_2) &= \frac{\delta_{i,j}}{\beta(\kappa k_i^4)} - \frac{1}{4A(D_1,D_1)A(D_2,D_2) - A(D_1,D_2)} \\
&\times \left[8A(D_1,D_1)B(i,D_2)B(j,D_2) \right. \\
&+ 8A(D_2,D_2)B(i,D_1)B(j,D_1) \\
&- \left. 4A(D_1,D_2)\left(B(i,D_2)B(j,D_1) + B(i,D_1)B(j,D_2)\right)\right],
\end{aligned} \tag{2.100}$$

where

$$\begin{aligned}
A(D_1, D_2) &= \frac{1}{2\beta\kappa} \sum_{n=0}^{N} \frac{\sin k_n D_1 \sin k_n D_2}{k_n^4} \\
B(i, D) &= \frac{\sin k_i D}{2\beta\kappa k_i^4}.
\end{aligned} \tag{2.101}$$

2.4.2 Simulation Details

2.4.2.1 Brownian dynamics simulations with finite beam elements

Simulations were carried out discretizing the filament with geometrically exact, nonlinear Timoshenko beam elements [JC99, Cri03, Rom04], which account for axial, torsional, bending, and shear deformation. Viscous drag is accounted for by

$$\boldsymbol{f}_{visc} = \boldsymbol{c}_t \dot{\boldsymbol{x}}, \quad \boldsymbol{m}_{visc} = \boldsymbol{c}_r \dot{\boldsymbol{\theta}} \tag{2.102}$$

with translational and rotational damping tensors $\boldsymbol{c}_t$ and $\boldsymbol{c}_r$ and translational and rotational velocities $\dot{\boldsymbol{x}}$ and $\dot{\boldsymbol{\theta}}$. Stochastic forces and moments are determined in accordance to the fluctuation-dissipation theorem and read

$$\boldsymbol{f}_{stoch} = \sqrt{2k_B T}\boldsymbol{s}_t \frac{\partial \boldsymbol{\mathcal{W}}_t^2(s,t)}{\partial s \partial t}, \quad \boldsymbol{m}_{stoch} = \sqrt{2k_B T}\boldsymbol{s}_r \frac{\partial \boldsymbol{\mathcal{W}}_r^2(s,t)}{\partial s \partial t} \tag{2.103}$$

with damping tensors $\boldsymbol{s}_{\{t,r\}}$ chosen to satisfy $\boldsymbol{s}_{\{t,r\}} {\boldsymbol{s}_{\{t,r\}}}^T = \boldsymbol{c}_{\{t,r\}}$. $\boldsymbol{\mathcal{W}}$ denotes a standard Wiener process.

Time is discretized using an *Implicit-Euler* scheme, which allows for larger step sizes and therefore much greater simulated time intervals as compared to explicit

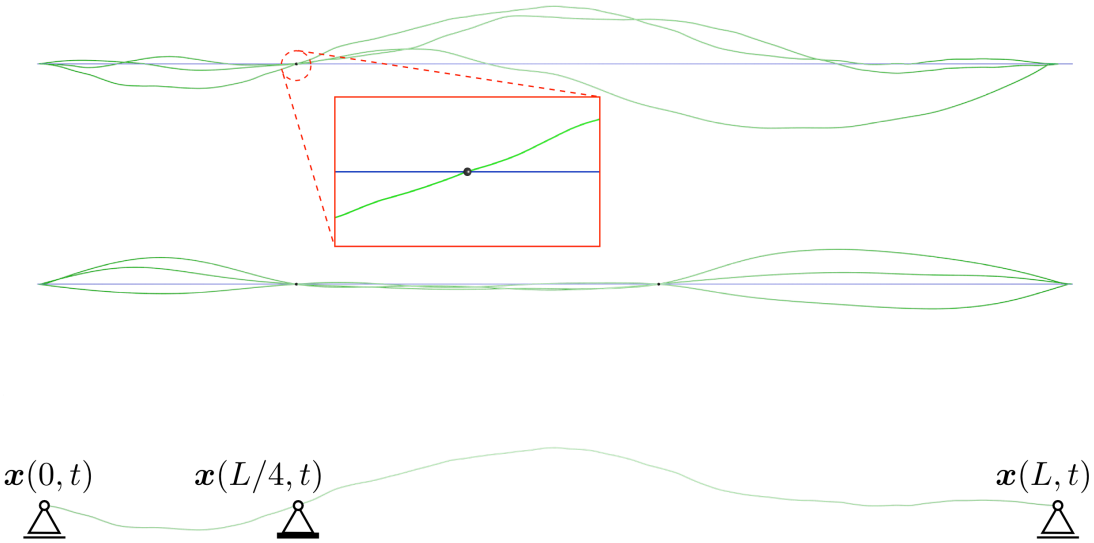

Figure 2.10: Snapshots of filaments pinned down at one location $s = 0.25L$ (*top*) and two locations $s_1 = 0.25L, s_2 = 0.6L$ (*center*) during simulation. Pinning sites are marked by black dots. The blue horizontal lines show the initial geometry. The zoomed part shows the smoothness and rotational freedom of the filament around the pinning site; mechanical supports of the filament (*bottom*): the ends of the filament are movable in one translational direction only, the translation of the pinning site is completely inhibited. Rotations are unconstrained in all cases.

schemes due to a better numerical stability. Full details on the mechanical model, the numerical method and the discretization in time are given in [CAO09, CNG10, CMB13].

2.4.2.2 Geometrical and mechanical properties

A filament of length $L = 10\mu$m and persistence length $L_p \approx 18.4\mu$m was discretized with $N = 4000$ beam finite elements, which for the applied beam formulation amounts to 24000 degrees of freedom. Its circular cross section area was set

to $A = 1.9\times10^{-5}\mu\text{m}^2$ leading to a high axial stiffness compared to its bending stiffness. The moment of inertia of area is set to $I = 2.85\times10^{-11}\mu\text{m}^4$ and the polar moment of inertia to $I_p = 5.7\times10^{-11}\mu\text{m}^4$. The initial, stress-free geometry was chosen straight and parallel to the global x-direction. Its movement was constrained to $\mathbb{R}^2$ allowing transverse deflections of the filament only in global y-direction. Temperature was set to $T = 293\text{K}$ and the dynamic viscosity of the fluid to $\eta = 10^{-3}\,\text{Pa}\,\text{s}$.

2.4.2.3 Effects of time discretization

Three different step sizes $\Delta t \in \{10^{-2}\text{s}; 10^{-4}\text{s}; 10^{-6}\text{s}\}$ of the time integration scheme were chosen in order to access a broad set of geometrical configurations of the filament. Figure 2.11 illustrates the effect of step size on the accuracy of the simulation with respect to capturing the filament's various eigenmodes. The left graph features results for $\Delta t = 10^{-2}\text{s}$, which show excellent agreement between theoretical prediction and simulation for slow modes $n \leq 5$. However, for mode numbers $n > 5$, the quality of the numerical approximation deteriorates due to Δt being too large to accurately capture faster modes. Hence, additional simulations were conducted in order to assess the behavior of the numerical model regarding its sensitivity to step size. The effect is clearly visible in the central and right panels of Figure 2.11. Simulations with intermediate step size $\Delta t = 10^{-4}\text{s}$ provide an acceptable approximation of slow modes. They exhibit an onset of deviation from theory at higher mode numbers around $n \geq 15$. Finally at the lowest studied step size $\Delta t = 10^{-6}\text{s}$, the trade-off in accuracy between fast and slow modes becomes even more apparent. While results for slow modes are poor, fast modes are approximated well. As characteristic relaxation times τ_n of the modes vary widely, the dynamics of the filament need to be sampled over a step size interval of several orders of magnitude as well.

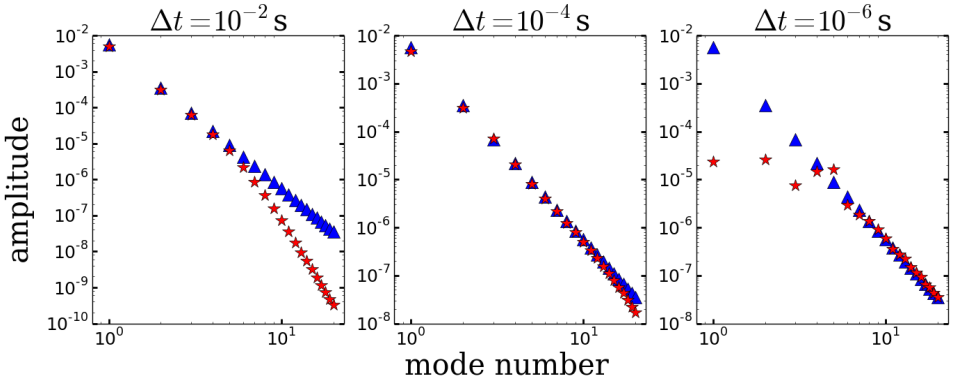

Figure 2.11: Comparison of theoretical (▲) diagonal mode amplitudes to those computed (★) from finite element simulations for different time discretizations.

2.4.2.4 Boundary conditions for single-filament simulations

In case of the simulation of a single filament, the effect of linkers pinning down the filament at a certain location s along the filament is modeled by permanently inhibiting the translational degrees of freedom at the pinning site as sketched in the bottom illustration of Figure 2.10. The filament is still free to rotate about this pinning site as shown in the zoomed part of the illustration at the top of Figure 2.10. The ends of the filament are free to slide in longitudinal direction and rotations remain unconstrained. Two parameter studies were conducted with transverse thermal fluctuations of the filament constrained by

(S1) a single pinning site at discrete finite element node positions $s \in [0; L/2]$. The affected nodes are located at sites $s/L \in \{[0.025; 0.5], \emptyset\}$ (illustration at the top of Figure 2.10). The empty set represents the linker-free case.

(S2) two pinning sites at positions $\{s_1, s_2\} \in [0; L], \quad s_1 \neq s_2$, neglecting symmetric configurations (illustration in the middle of Figure 2.10).

All cases with a single pinning point were simulated for $i > 200000$ time steps for all step sizes, while all cases with two pinning sites were simulated up to $i \approx 100000$ time steps.

2.4.2.5 Calculation of covariance matrices from simulations

Simulations provide us with filament geometries, from which we can draw the transverse deflections of the filament $y(s)$. Over the course of a total number of I time steps, we gather $M \leq I$ geometrical configurations of the filament. In case of a discretized geometry, we obviously are only able to provide a discrete signal of length L, which in turn allows for a discrete Fourier analysis up to mode $N = L/2$. The k^{th} Fourier coefficient, i.e., the approximated amplitude of eigenmode k, is

$$A_k = \sqrt{\frac{2\pi}{L}} \sum_{n=1}^{N} y(s) \sin(n\pi\, s/L). \tag{2.104}$$

With this, the covariance matrix can be written as

$$\langle A_k A_l \rangle = \mathrm{cov}(A_k, A_l) = \mathrm{E}\left[(A_k \cdot A_l)\right] \tag{2.105}$$

with mode number indices k and l, providing a measure for the interdependence of modes.

2.4.3 Results

The numerically determined mode amplitudes for the single pinning site are compared with Eq. 2.99, and with Eq. 2.100 for the double pinning sites. Levine plots encode the results and are shown for an array of single site locations in Fig. 2.13, and double site locations in Fig. 2.13. For details on the Levine plot please see Fig. 2.12, which explains the plot for $D = .4L$. Errors are consistently on the order of 10% and may be shown to decrease with additional observations. The equivalence of the mode spectra between simulation and theory suggests that ideal cross-linkers experience a fluctuation induced attraction when bound to semi-flexible filaments.

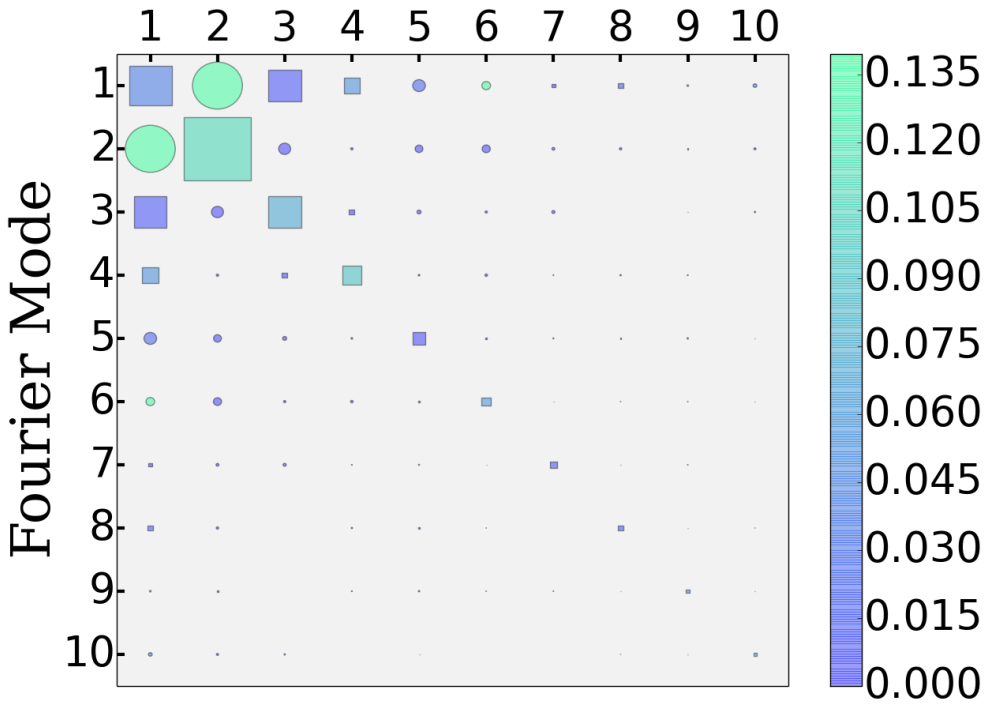

Figure 2.12: The Fourier amplitude covariance matrix of the first 10 modes obtained via finite element simulation for a filament pinned at $D = .4L$ The area of each element represents its log normalized magnitude, while its shape represents the sign with rectangles being positive, circles negative. The color bar indicates the % error relative to Eq. 2.99. The error magnitude is consistent across different pinning locations and supports the existence of a casimir effect between crosslinkers in semiflexible polymers.

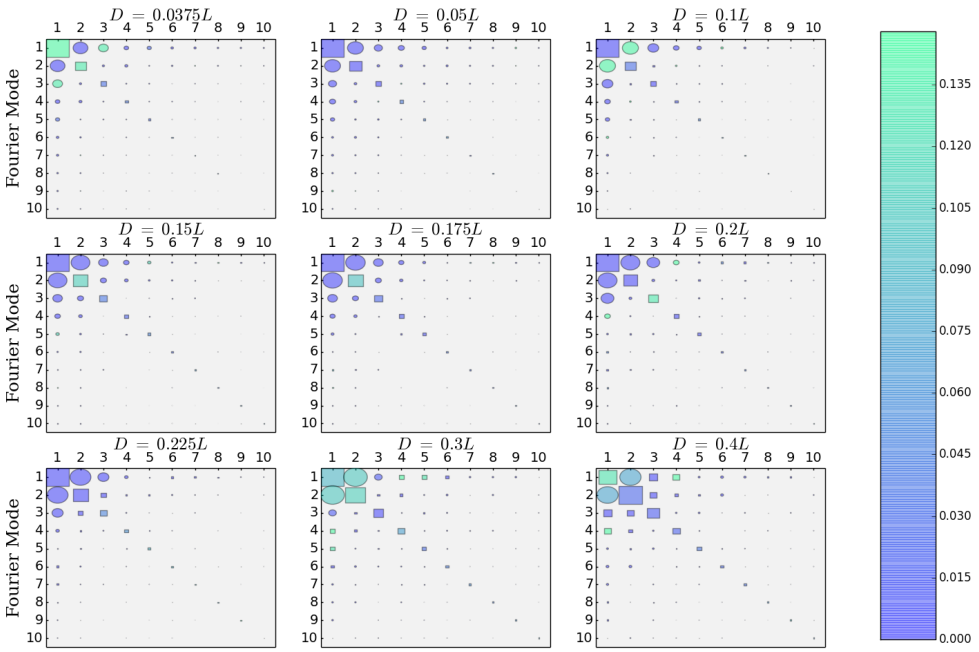

Figure 2.13: Levine plots for nine different values of the single pinning location D-See Fig. 2.10. Errors are consistently on the order of 10%. Please see Fig. 2.12 for details regarding the Levine plot.

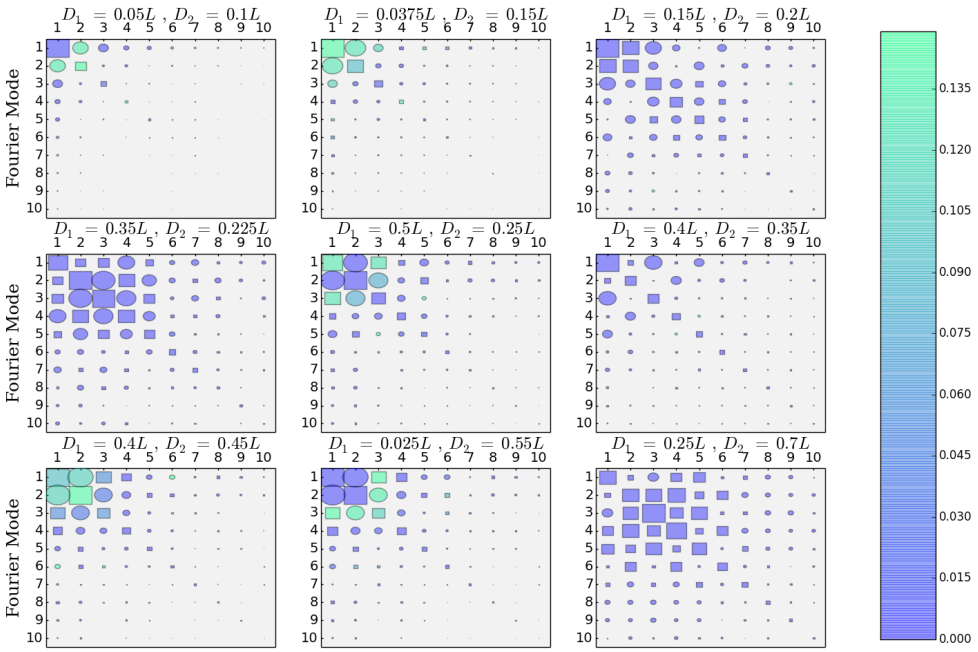

Figure 2.14: Levine plots for nine different values of the two pinning locations D_1 and D_2–See Fig. 2.10. Errors are consistently on the order of 10%. Please see Fig. 2.12 for details regarding the Levine plot.

2.5 Conclusions

I showed in this chapter that when semiflexible polymers are connected by sliding linkers as in Fig.2, then thermal conformational fluctuations generate a long-range Casimir attractive pair interaction $V(D) = \gamma k_B T \log D$ between linkers separated by a distance D. The proportionality constant γ is a number that ranges from 1/2 to 4 depending on: (i) the presence or absence of tension along the polymer, (ii) whether or not the polymers are confined to a plane, and (iii) the rigidity of angular constraints imposed by the sliding linkers.

For distances large compared to the persistence length, the polymers can be treated as flexible. In that case, $V(D)$ can be roughly approximated as the entropic energy cost of a loop of size D, if we reinterpret D as the total polymer length between the two linkers. In that limit, the linker pair-interaction maintains the same form, though the prefactor γ will be different (for non self-avoiding polymers, γ would equal $d/2$ with d the spatial dimension). It is important to stress that the Casimir attraction between sliding linkers only is important if elastic stress does not prevent the two linkers from approaching each other. For example, if the two sliding linkers in Fig. 2 impose a non-zero angle then this generates an elastic stress that amounts to a repulsive interaction that overwhelms the Casimir interaction on length scales small compared to the persistence length. The most interesting examples of polymer networks held together by transient linkers involve F-actin filaments in the presence of linker proteins. F-actin has a persistence length in the range of 20 microns. The force between two sliding linker proteins separated by a distance of $\sim$ 10nm is in the picoNewton range, which is the same order of magnitude as typical forces exerted on proteins.

Any elastic compliance in the cross linkers will decrease the overall prefactor of the Casimir interaction between them. We analyzed this effect for the case of replacing the fixed angle boundary conditions with a harmonic potential having

a minimum at the desired crossing angle of the two filaments at the cross linker. As the curvature of that potential was reduced, the contribution to the Casimir interaction coming from the pinning of the angular degrees of freedom vanished continuously. Since slope and position variables are treated analogously within the path integral formulation, replacing the boundary condition of the fixed filament position at the cross linkers with a harmonic potential at those positions will have a similar effect. Alternately, one might consider treating the cross linkers as small rings of radius a, as represented in our figures. If that radius is finite then undulatory modes of the filaments with an equilibrium amplitude less than a should be essentially unaffected by the rings and not contribute to the Casimir interaction. As the persistence length of the filaments diverges and all undulatory mode amplitudes decrease, the Casimir interaction must vanish. We pursued our calculation by first taking the limit of an infinitesimal ring so that our results show a finite Casimir interaction for arbitrarily large (but finite) persistence lengths. As mentioned above however, one can still explore the effect of softening the position boundary condition by treating the cross linker as a spring instead of a hard constraint.

Different values for γ may lead to different equilibrium phase behavior for networks of semiflexible polymers. Assume a stress-free network of semiflexible polymers held together by sliding linkers. If two neighboring linkers of a given polymer can approach each other – without generating elastic stress – then the equilibrium probability distribution $P(D)$ for the separation of the two linkers would be proportional to $\exp[-\beta V(D)] \propto 1/D^{\gamma}$. The mean square separation $<D^2>$ of the two linkers then would be infinite for γ less than or equal to 2. That would suggest that for γ greater than 2, linkers would come together into pairs of linkers. Would this trigger decomposition of the network as a whole? Estimate the free energy density of the linker many-body system as $F(\rho)/k_{\mathrm{B}}T \approx \rho \log \rho - (z/2d)\gamma\rho \log \rho$, with z the average number of nearest neighbors per linker

in the network and $\rho \approx 1/D^d$ the linker density. The critical value for γ above which the free energy density is a concave function of the density is $2d/z$. For larger values of γ, the network state is thermodynamically unstable. These arguments assumed that the Casimir force could be treated as a pair interaction. In Sec. 2.3.4 we show that this is not quite right: three-body Casimir interactions cannot be neglected in general. I will explore the thermodynamic stability of these networks in much greater detail in the following chapter.

We conclude by noting an important difference between the Casimir interactions in liquid membranes and on semiflexible polymers. It is essential to recognize that the linkers in our problem constrain the filament's position with respect to the space in which the filament is embedded. In other words, the filament can exchange momentum with the background system, e.g., a polymer network with the linkers at those points. If it were not constrained in this manner, so that the linker polymer system could collectively diffuse in the space, there would be *no* fluctuation-induced interaction between the linkers. This is demonstrated in Sec. 2.2.3. This aspect of the Casimir interaction on one dimensional elastic objects is surprising when compared to the analogous problem of rigid, disk-like inclusions in an isolated membrane. These are known to interact via a power-law Casimir force even if the collective disk and membrane system were allowed to freely diffuse in the embedding space. One cannot simply generalize this membrane result to the semiflexible polymer problem and this has significant biophysical implications. Based on our result, we predict that DNA binding proteins do not experience a long-ranged attractive Casimir interaction along a DNA filament, while membrane-bound proteins do.

CHAPTER 3

Casimir Gas & Bundle Stabilization

3.1 Introduction

Semiflexible networks with transient cross linkers form the main structural elements of the cytoskeleton of eukaryotic cells and provide an intriguing arena in which to study nonequilibrium physics. Due to the steric interactions between the long filaments (e.g. F-actin) these systems are typically frustrated, unable to reach more ordered ground states [CMS13]. In spite of this steric frustration, experiments [GSM04, WTH06, PPH03, SLB09, LCH07] have found that both the statistical properties of the network's structure and its mechanics (rheology) can be reproducibly predicted as a function of the ratio of the concentrations of the filaments and their cross linkers. In particular, one observes an abrupt transition between filament networks and networks composed of small bundles of these filaments as a function of these concentrations. This seems surprising as one might expect there to be continuous growth of bundles with increasing cross linker density, cutoff in the high cross linker limit only by the aforementioned steric frustration.

In this letter we propose that one can understand the abruptness of the bundling transition in semiflexible networks by considering the Casimir or fluctuation based interaction between cross linkers bound to the same filament. The basic physics of this Casimir interaction in semiflexible polymers has been explored previously–See Ch. 2. Here we present new calculations showing that, due

to the long-range nature of the Casimir interaction, there is an abrupt condensation transition in which a gas of free cross linkers abruptly lock nearly parallel filaments into bundles as a function of cross linker concentration. We test the predictions of the fundamental Casimir interaction between cross linkers and the condensation transition based on this interaction using large-scale Brownian dynamics finite-element simulations of the network.

This first order condensation transition appears in spite of the one-dimensional nature of the problem due specifically to the long-range (i.e., logarithmic) nature of the fluctuation-induced interaction between cross linkers (violating the van Hove condition [Hov50]). This allows for the abrupt condensation transition in the line density of cross linkers on the filament at a critical value of their chemical potential. In the condensed phase one finds that the bound linker line density is significantly enhanced relative to that expected from a simple Langmuir isotherm [Lan18]. In fact, one rapidly reaches bound linker saturation where their line density is limited only by their hardcore repulsion. Below the condensation point one finds large linker density fluctuations but a small mean concentration implying insignificant bundling. Thus, we find that Casimir interactions between linkers produce a type of binary chemical switch controlled by linker concentration between two states: (i) free filaments and a solution of unbound cross linkers below the transition, and (ii) bundles composed of filaments that are maximally coated with cross linkers. One may speculate that this cooperative transition produced by the strongly interacting linker gas is exploited by the cell to induce such dramatic structural rearrangements in the cytoskeleton via small changes in linker protein concentration by remaining near the critical linker concentration. Conversely, the cell may limit the dependence of cytoskeletal structure upon the precise concentration of linkers by tuning their concentration far away from this boundary.

In section 3.2 we derive the macroscopic properties of a line of Casimir inter-

acting particles using classical results for one dimensional systems. We assume a pairwise potential and study the interaction of a single particle with an island of linkers to justify the assumption. The equation of state predicts novel behavior, including the previously mentioned condensation transition. These surprising results are verified in Sec. 3.3 with a Monte Carlo simulation using the Metropolis–Hastings dynamics to prove the equilibrium distribution of the gas. In sec 3.5 we study physical bundles, such as the ubiquitous actin bundles found in biology, with large scale finite element simulations, and find evidence of a condensation transition in these more realistic systems. The chapter concludes with a discussion of the statistical mechanics of the Casimir gas, with an emphasis on the pair distribution function.

3.2 Thermodynamics of the Casimir Gas

The extension of the two-particle Casimir interaction derived in Ch.2 to a large number of cross linkers in a network has two nontrivial features: (i) Because cross linkers will only interact if they are on the same filament, the full interaction energy of a network configuration depends explicitly on the network topology, and (ii) a single filament's degrees of freedom on either side of the cross linker are coupled by the condition of slope continuity, leading to an interaction which is not strictly pairwise. For these reasons a treatment of general networks is difficult, but one particularly simple topology, the *bundle*, is amenable to analytic calculations. The simplest bundle model, which we consider here, consists of two parallel filaments sufficiently close together so that linkers may join them. In this section we will first examine the validity of the pairwise interaction approximation for different cross-linker types, then study the thermodynamics of this one dimensional system.

3.2.1 Geometry and Interactions

Consider N cross-linkers adsorbed onto a tensionless semi-flexible filament of length L and bending modulus κ. An isolated filament will fluctuate at finite temperature T with a spectrum specified by the equipartition theorem (see Sec. 2.3.5) and the cross-linkers will not interact. However, if the cross-linkers bind the filament to a stiff elastic background as shown in Fig. 3.1, their modification of the fluctuation spectrum of the filament will mediate an attractive Casimir interaction. This was shown in detail for two and three cross-linkers in Ch. 2 but the argument is easily extended to a large number of particles. The partition function of N particles separated by displacements d_i is

$$\mathcal{Z} \propto \left(\prod_{i=1}^{N-1} \frac{1}{d_i^{2d_\perp}} \right) \exp \left\{ - \sum_{i=1}^{d_\perp (N-1)} \frac{2}{d_i} \left(v_i^2 + v_{i+1}^2 + v_i v_{i+1} \right) \right\}, \tag{3.1}$$

where $d_\perp$ is the dimension of transverse fluctuations of the filament, v_i is the angle the filament makes with the $\hat{z}$ direction (see Fig. 2.2), and a constant prefactor has been neglected. The sum in the exponent goes to $d_\perp(N-1)$ because there is one v_i for each transverse dimension. This equation assumes the slope is continuous across a linker, which is justified for the stiff semi-flexible polymers we consider in this work. This assumption has important consequences: The Casimir interaction between cross-linkers is not strictly pairwise since the filament's degrees of freedom on either side of the crosslinker are coupled.

The properties of the cross-linkers naturally have a significant impact on the strength of the interaction. Here we explore what role, if any, they play in the assumption of pairwise additivity. We recognize and draw distinction between two broad categories of of cross-linkers: Bundling linkers, which fix the slope of the filament to be zero, and network linkers which have no preference and are flexible enough to allow for slope fluctuations–see Sec. 2.3 for more details. As will be shown, bundling linkers interact in a purely pairwise additive fashion, while network linkers experience lightly screened interactions. Nevertheless, if the

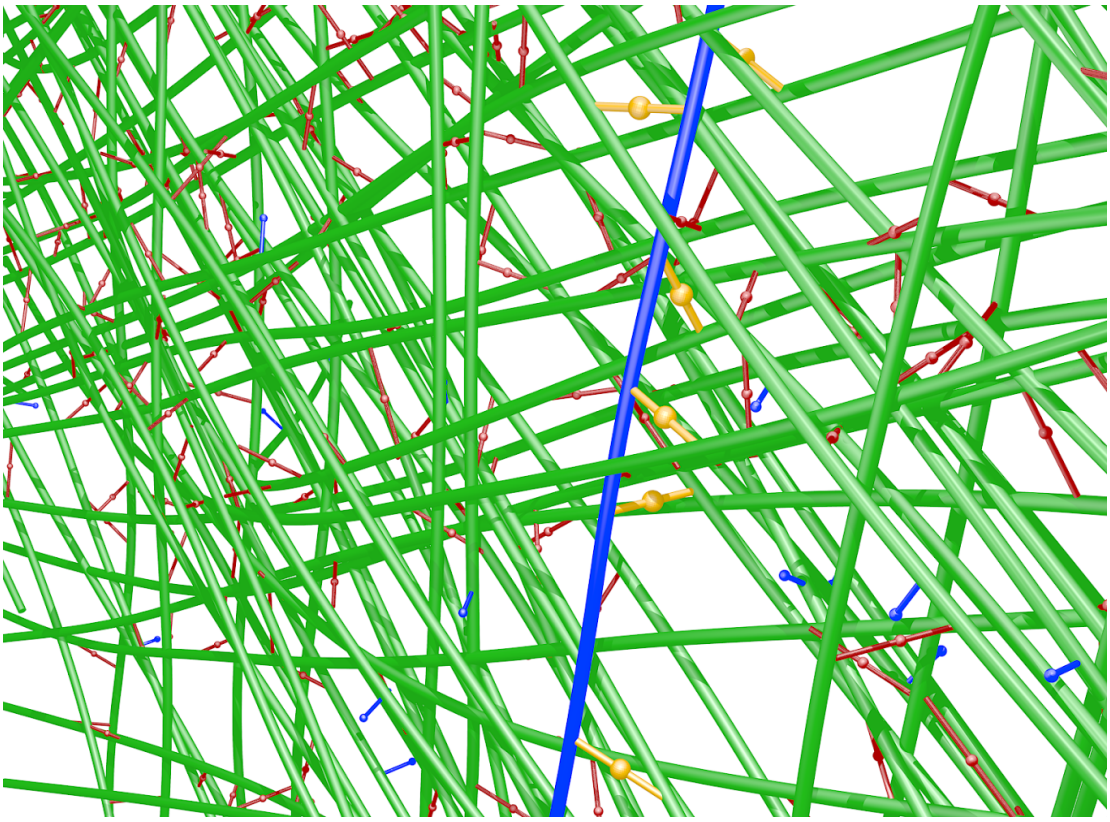

Figure 3.1: A single filament, shown in blue, is attached to a background elastic network. The cross-linkers, highlighted in yellow, experience a Casimir interaction due to their modification of the fluctuation spectrum of the filament away from it's equilibrium form. It is essential that the filament is pinned to the background: An isolated filament with bound linkers will not generate a Casimir interaction–see Sec. 2.2.3

network linkers cluster they will in fact behave as a single bundling type linker, lending credibility to the treatment of the Casimir interaction as pairwise.

Bundling cross-linkers force the slope v_i to vanish wherever they bind. The full partition now factorizes as

$$\mathcal{Z} = \prod_{i=1}^{N-1} \mathcal{Z}_1(d_i), \tag{3.2}$$

where the single particle partition function is $\mathcal{Z}_1(d) = 1/d^{2d_\perp}$. Bundling cross-linkers experience strictly pairwise interactions with the Casimir potential $V(d) = 2d_\perp T \log(d/\lambda_c)$, where we have set Boltzmann's constant $k_\mathrm{B} = 1$, and the length λ_c represents the volume of phase space of a single filament state and is related to $\hbar$ – see Sec. 2.2.2.5 for details.

The many body interaction of network linkers is considerably more complicated. The slopes v_i must be integrated out of the partition function to derive the full interaction. It is instructive to review a few finite cases before studying the large N limit. Two network linkers separated by a distance d have the potential $V(d) = d_\perp \log(d/\lambda_c)$ (see Sec. 2.3.1). The integration produces a repulsive contribution to the force which cancels exactly half of the original interaction. Continuing, consider three mutually interacting network linkers, separated by d_1 and $d_2 = d - d_1$, as shown in Fig. 2.9. The interaction potential is given by Eq. 2.75 and is reproduced here

$$V(d_1, d_2) = d_\perp T \left(\log(d_1/\lambda_c) + \log(d_2/\lambda_c) + \frac{1}{2}\log(d/\lambda_c) \right). \tag{3.3}$$

We find that the leftmost linker experiences a force $f = -d_\perp T \left(\frac{1}{2D} + \frac{1}{d_1} \right)$ which is the sum of nearest and next nearest neighbor contributions. Insight into the problem comes from letting $d_1 \to d$, representing a single linker interacting with a cluster of two linkers. The resulting force, $-\frac{3d_\perp T}{2d}$, is equivalent to the two body interaction of a network linker with a bundling linker. This is a natural result because tight clusters eliminate fluctuations and therefore must force the slopes

to be identically zero at the edges of the cluster. This suggests that a cluster of network linkers behaves identically to a single bundling linker. The prefactor 3/2 may be alternatively understood as the fluctuation generated elastic repulsion $\frac{Td_\perp}{2d}$ of the single network linker subtracted from the pairwise bundle linker force $\frac{2Td_\perp}{d}$. We see that an individual linker will be preferentially attracted to clusters over solitary linkers. This result should hold for the interaction of a single linker with any size cluster up to correction of order $\frac{a}{d}$, where a is the mean spacing within a cluster and d is the separation of the single linker with the cluster. We may also deduce that two clusters will interact with the full fluctuation force $-\frac{2k_\mathrm{B}T}{D}$ since there are no slope fluctuations at either end.

We will now attempt an analytical treatment of N network linkers. As stated, consider N interacting network linkers with local slopes v_i separated by projected distances d_i. For simplicity let $d_\perp = 1$. We rewrite the partition function Eq. 3.1 in more compact notation

$$\mathcal{Z} = \left(\prod_i^{N-1} \frac{1}{d_i^2} \right) \exp\left\{ -2\mathbf{v}^T \mathbf{M} \mathbf{v} \right\}, \tag{3.4}$$

where $\mathbf{v}$ is a vector of slopes:

$$\mathbf{v} = \begin{pmatrix} v_1 \\ v_2 \\ \vdots \\ v_N \end{pmatrix}, \tag{3.5}$$

and $\mathbf{M}$ is symmetric positive definite matrix

$$\mathbf{M} = \begin{pmatrix} \frac{1}{d_1} & \frac{1}{2d_1} & 0 & \dots & 0 \\ \frac{1}{2d_1} & \frac{1}{d_1} + \frac{1}{d_2} & \frac{1}{2d_2} & \ddots & \vdots \\ 0 & \frac{1}{2d_2} & \ddots & \ddots & 0 \\ \vdots & \ddots & \ddots & \frac{1}{d_{N-1}} + \frac{1}{d_{N-2}} & \frac{1}{2d_{N-1}} \\ 0 & \dots & 0 & \frac{1}{2d_{N-1}} & \frac{1}{d_{N-1}} \end{pmatrix}. \tag{3.6}$$

After integrating out the slope variables one finds

$$\mathcal{Z} \propto \frac{1}{\left(\prod_i^{N-1} d_i^2\right)\sqrt{\det \mathbf{M}}}. \tag{3.7}$$

The determinant is difficult to calculate in general and it's best to examine a specific case, which has applications to the cluster geometry, where the linkers are equally spaced $d_i = d$. The factor $\frac{1}{d}$ in $\mathbf{M}$ is common to all terms now and may be factored out. We must now calculate the determinant of the $N \times N$ matrix

$$\mathbf{J}_N = \begin{pmatrix} 1 & \frac{1}{2} & 0 & \dots & 0 \\ \frac{1}{2} & 2 & \frac{1}{2} & \ddots & \vdots \\ 0 & \frac{1}{2} & \ddots & \ddots & 0 \\ \vdots & \ddots & \ddots & 2 & \frac{1}{2} \\ 0 & \dots & 0 & \frac{1}{2} & 1 \end{pmatrix}. \tag{3.8}$$

The approach is to develop a recursion relation for the determinant of $\mathbf{J}_N$ with initial conditions $\det \mathbf{J}_1 = 1, \det \mathbf{J}_2 = \frac{3}{4}$. First introduce the auxiliary $N \times N$ matrices $\mathbf{W}_N$ and $\mathbf{Q}_N$, defined as

$$\mathbf{W}_N = \begin{pmatrix} 2 & \frac{1}{2} & 0 & \dots & 0 \\ \frac{1}{2} & 2 & \frac{1}{2} & \ddots & \vdots \\ 0 & \frac{1}{2} & \ddots & \ddots & 0 \\ \vdots & \ddots & \ddots & 2 & \frac{1}{2} \\ 0 & \dots & 0 & \frac{1}{2} & 1 \end{pmatrix}$$

$$\mathbf{Q}_N = \begin{pmatrix} \frac{1}{2} & \frac{1}{2} & 0 & \dots & 0 \\ 0 & 2 & \frac{1}{2} & \ddots & \vdots \\ 0 & \frac{1}{2} & \ddots & \ddots & 0 \\ \vdots & \ddots & \ddots & 2 & \frac{1}{2} \\ 0 & \dots & 0 & \frac{1}{2} & 1 \end{pmatrix}. \tag{3.9}$$

It is easily seen that

$$\det \mathbf{J}_N = \det \mathbf{W}_{N-1} - \frac{1}{2} \det \mathbf{Q}_{N-1}, \tag{3.10}$$

and furthermore

$$\begin{aligned} \det \mathbf{W}_N &= 2 \det \mathbf{W}_{N-1} - \frac{1}{2} \det \mathbf{Q}_{N-1} \\ \det \mathbf{Q}_N &= \frac{1}{2} \det \mathbf{W}_{N-1}. \end{aligned} \tag{3.11}$$

Combining Eq. 3.11 we have the closed recurrence relation

$$\det \mathbf{W}_N = 2 \det \mathbf{W}_{N-1} - \frac{1}{4} \det \mathbf{W}_{N-2}, \tag{3.12}$$

with initial conditions $\det \mathbf{W}_0 = \det \mathbf{W}_1 = 1$. An ansatz of $\det \mathbf{W}_N = r^N$ solves the relation for $r_\pm = 1 \pm \frac{\sqrt{3}}{2}$ and the linear combination which satisfies the initial conditions is

$$\det \mathbf{W}_N = \frac{1}{2} \left(1 + \frac{\sqrt{3}}{2} \right)^N + \frac{1}{2} \left(1 - \frac{\sqrt{3}}{2} \right)^N. \tag{3.13}$$

The determinant of $\mathbf{Q}_N$ is found directly from Eq. 3.11 and one may now calculate the determinant of $\mathbf{J}_N$:

$$\begin{aligned} \det \mathbf{J}_N &= \frac{1}{2} \left(1 + \frac{\sqrt{3}}{2} \right)^{N-1} + \frac{1}{2} \left(1 - \frac{\sqrt{3}}{2} \right)^{N-1} \\ &- \frac{1}{8} \left[\left(1 + \frac{\sqrt{3}}{2} \right)^{N-2} + \left(1 - \frac{\sqrt{3}}{2} \right)^{N-2} \right]. \end{aligned} \tag{3.14}$$

In the large N limit only the r_+ solutions survive, leaving

$$\det \mathbf{J}_N = \frac{1}{2} \left(1 + \frac{\sqrt{3}}{2} \right)^{N-1} - \frac{1}{8} \left(1 + \frac{\sqrt{3}}{2} \right)^{N-2}. \tag{3.15}$$

The exact free energy for this special case of an island of interacting cross linkers is given by

$$\mathcal{F}_{island} = T d_\perp \left[\left(\frac{3N}{2} - 2 \right) \log d + \frac{1}{2} \log \det \mathbf{J}_N \right], \tag{3.16}$$

where we have restored the dependence on $d_\perp$. The second term is independent of d and may be dropped if considering an island at fixed N. We see that, in the large N limit, the free energy can be written as a sum of pairwise logarithmic interactions with strength $\frac{3Td_\perp}{2}$. In this mean field sense the Casimir interaction

of network linkers is pairwise additive, although with a coupling exactly between the network and bundle two particle interactions. The result can be improved by considering a single linker separated by D from the island. The derivation of the partition function is nearly identical to the simple island case. The D dependent part of the resulting free energy is

$$\mathcal{F} = Td_\perp \left\{ \frac{3}{2} \log D/\lambda_c + \frac{1}{2} \log \left[4r_+ - 1 + 3r_+ \frac{d}{D} \right] \right\}. \tag{3.17}$$

When the linker is far away from the island, $D \gg d$, the island appears as a single bundling linker and the characteristic $3/2$ prefactor emerges. Conversely, for $D \ll d$ the coupling becomes $Td_\perp$, which is the bare two particle interaction for network type cross-linkers. Finally, if $D = d$ we find the coupling $Td_\perp \frac{3}{2} \left(2 - \frac{2}{\sqrt{3}} \right) \approx 1.27 Td_\perp$. The interaction of network linkers is always strengthened by the inclusion of non nearest-neighbor interactions, but in all cases it may be understood as a simple renormalization of the coupling parameter.

This analysis suggests that the integration of the filament's degrees of freedom produces a pairwise potential between linkers with the general form $V(x) = d_\perp \alpha T \log x/\lambda_c$, where α depends on the nature of the cross-linkers: Bundling linkers have $\alpha = 2$, whereas network linkers will have $1 < \alpha < 3/2$. The singularity at $x = 0$ is an unphysical consequence of including arbitrarily high wavenumber fluctuations in the calculation of the Casimir interaction. We assign a hard core potential of radius a to the cross-linkers to mask our ignorance of the short distance physics of the system. The final form of the potential which will be used throughout the chapter is

$$V(x) = \begin{cases} \infty & \text{if } x < a \\ d_\perp \alpha\, T \log \frac{x}{\lambda_c} & \text{if } x \geq a. \end{cases} \tag{3.18}$$

3.2.2 One Dimensional Thermodynamics

It is always possible to obtain an implicit equation of state for a one dimensional pairwise interacting system, from which all thermodynamic functions follow naturally. The derivation presented follows [LM66] and begins by considering the partition function of N particles on a line of length L interacting with the pairwise potential V

$$\begin{aligned} Z_N(L) &= \int\cdots\int_{0<x_1<x_2<\cdots<x_N<L} \mathrm{d}x_1\cdots\mathrm{d}x_N \exp\left\{-\beta\left[V(x_1)\right.\right. \\ &+ \left.\left. V(x_2-x_1)+\cdots+V(L-X_N)\right]\right\}, \end{aligned} \tag{3.19}$$

where $\beta = \frac{1}{T}$ is the inverse thermodynamic temperature and I have assumed the particle-wall interaction is equivalent to the particle-particle interaction. The integral has the form of an N fold convolution of the function

$$\Omega(R) = e^{-\beta V(R)}, \tag{3.20}$$

so that the partition function may be written succinctly as

$$Z_N(L) = \underbrace{\Omega \star \Omega \star \cdots \star \Omega}_{N}. \tag{3.21}$$

Functions of this form are most conveniently written in terms of a Laplace variable s since convolutions map onto multiplication in Laplace space. Rewriting, we have

$$\begin{aligned} Z_N(s) &= [\Omega(s)]^N \\ \Omega(s) &= \int_0^\infty e^{-sx-\beta V(x)}\,\mathrm{d}x. \end{aligned} \tag{3.22}$$

To connect this result to thermodynamic functions one can alternatively write

$$Z_N(s) = \int_0^\infty \mathrm{d}L\, Z_N(L)\exp\{-sL\} = \int_0^\infty \mathrm{d}L \exp\left\{-\beta(F+\frac{s}{\beta}L)\right\}, \tag{3.23}$$

where F is the configurational part of the Helmholtz free energy, $F = -T\log Z$. In the large N limit the integral is expected to be sharply peaked and we may safely replace the integral by it's largest value,

$$Z_N(s) \approx \exp\left\{-\beta(F+\frac{s}{\beta}L)\right\}. \tag{3.24}$$

The extremal condition requires

$$\frac{\mathrm{d}}{\mathrm{d}L}(F + \frac{s}{\beta}L) = 0, \tag{3.25}$$

implying that the quantity $p \equiv \frac{s}{\beta} = -\frac{\mathrm{d}F}{\mathrm{d}L}$ should be interpreted as the pressure of the system. With this association we recognize $F + \frac{s}{\beta}L = F + pL$ as the configurational contribution to the Gibbs free energy G. Furthermore, for an extensive system (appropriate for strictly nearest neighbor interactions) $G = \mu N$, where μ is the chemical potential. Finally, comparing with the direct evaluation of the partition function one finds

$$Z_N(s) = \exp^{-\beta\mu N} = \left[\int_0^\infty e^{-\beta p x - \beta V(x)}\,\mathrm{d}x\right]^N, \tag{3.26}$$

or, upon inclusion of the kinetic degrees of freedom

$$\beta\mu = -\log\left(\frac{1}{\lambda_t}\int_0^\infty e^{-\beta p x - \beta V(R)}\,\mathrm{d}x\right), \tag{3.27}$$

where λ_t is the thermal deBroglie wavelength, $\lambda_t = \sqrt{\frac{2\pi\beta\hbar^2}{m}}$. This final result is an implicit relation between the chemical potential and the thermodynamic pressure. For the convenience of deriving other thermodynamic functions it may be encoded in the function

$$f(\beta, \mu, p(\beta,\mu)) \equiv \beta\mu + \log\left(\frac{1}{\lambda_t}\int_0^\infty \mathrm{d}x\, e^{-\beta p x} e^{-\beta V(x)}\right). \tag{3.28}$$

3.2.3 Casimir Gas Equation Of State

Inserting the Casimir pair potential Eq. 3.18 into Eq. 3.28 gives an implicit relation between the (one-dimensional) pressure $p(\beta,\mu)$ of the linkers in the bundle, temperature, and their chemical potential μ,

$$\beta\mu = -\log\left[\frac{(\lambda_c\beta p)^{d_\perp\alpha}}{\lambda_t\beta p}\Gamma(1 - d_\perp\alpha, \beta p a)\right], \tag{3.29}$$

where $\Gamma(s,x)$ is the upper incomplete gamma function. The chemical potential of the linkers on the bundle may be controlled by allowing them to come into

chemical equilibrium with a solution of free linkers at number density c; treating the linker solution as an ideal gas one finds $\beta\mu = \log c\lambda_t^d$. Deviations from ideality in the solution phase may be accounted via standard methods, and are immaterial to our discussion.

The chemical potentials and pressures of the gas and line, μ_g, p_g and μ_l, p_l, respectively, must be equal in equilibrium. However, if the gas is made sufficiently dilute such that the pressure of the gas $p_g \to 0$ it can be shown that there are no solutions to equation 3.29 for sufficiently strong interaction strength $d_\perp\alpha$. Explicitly, the $p \to 0$ limit is

$$\begin{aligned} \beta\mu_l &\to -\infty & \alpha \leq 1 \\ \beta\mu_l &\to \log\left[\frac{\lambda_c}{\lambda_t}(d_\perp\alpha - 1)\right] & \alpha > 1. \end{aligned} \tag{3.30}$$

The $p \to 0$ limit of the ideal gas is equivalent to letting the chemical potential go to -∞ and this suggests that it will be possible to find equilibrium solutions for $\alpha \leq 1$. For more strongly interacting particles the condition $\mu_g \geq \mu_{crit} = T\log[\frac{\lambda_c}{\lambda_t}(d_\perp\alpha - 1)\,]$ is required for equilibrium. To explore this relation in more depth we must consider other state variables.

The pressure $p(L,T)$ can be found from the relation $N = -\frac{\partial}{\partial\mu}\Omega = L\frac{\partial p}{\partial\mu}$, where $\Omega = -pL$ is the grand potential, in conjunction with

$$\frac{\mathrm{d}f}{\mathrm{d}\mu} = \frac{\partial f}{\partial\mu} + \frac{\partial f}{\partial p}\frac{\partial p}{\partial\mu} = 0. \tag{3.31}$$

This implies the general relation

$$\frac{N}{L} = \frac{\partial p}{\partial\mu} = -\frac{\frac{\partial f}{\partial\mu}}{\frac{\partial f}{\partial p}} = \frac{\int_0^\infty \mathrm{d}x\, e^{-\beta px}e^{-\beta V(x)}}{\int_0^\infty \mathrm{d}x\, x\, e^{-\beta px}e^{-\beta V(x)}}, \tag{3.32}$$

which for the case of the nearest neighbor Casimir interaction Eq. 3.18 becomes

$$\frac{Na}{L} \equiv \rho = \frac{a\int_a^\infty \mathrm{d}x\, x^{-d_\perp\alpha}e^{-\beta px}}{\int_a^\infty \mathrm{d}x\, x^{1-d_\perp\alpha}e^{-\beta px}} = \beta pa\frac{\Gamma(1-d_\perp\alpha, \beta pa)}{\Gamma(2-d_\perp\alpha, \beta pa)}, \tag{3.33}$$

where we have introduced the line density ρ. This equation of state implicitly gives the pressure of the gas in terms of the line density, temperature and interaction

strength. Unfortunately, explicit expressions for the pressure can only be found in select limits. The physics of a dense gas will be dominated by the hard core interaction between the particles, and it is expected that the equation of state will be independent of the Casimir interaction strength. In fact, when $d_\perp \alpha = 0$ the solutions should reduce to the classical Tonks gas equation of state for hard core spheres [Ton36]:

$$p_t = \frac{\rho T}{a(1-\rho)}. \tag{3.34}$$

This equation of state is quite simple to understand: in the low density limit $\rho << 1$ the gas is ideal, while conversely the pressure diverges for $\rho \to 1$ as it takes an infinite amount of work to add an additional particle to an otherwise full line. We similarly expect the pressure to be large in the Casimir gas when $\rho \to 1$ and upon taking this limit in Eq. 3.33 one finds

$$p_c = \frac{T}{a(1-\rho)}, \tag{3.35}$$

which is identical to the Tonks pressure, ignoring corrections of order $\epsilon = 1 - \rho$. The Casimir interaction causes the pressure to be strictly less than the Tonks pressure, but the effect is overwhelmed by the hard core repulsion at high line densities. The converse is true at low line densities where we expect significant deviations from ideal gas behavior and also strong dependence on the interaction strength. Since the pressure at low line densities must also be very low it is reasonable to expand the Gamma functions in Eq. 3.33 for small second argument. We find

$$\rho = x \frac{x^\alpha \Gamma(1 - d_\perp \alpha) + \frac{x}{d_\perp \alpha - 1} - \frac{x^2}{d_\perp \alpha - 2}}{x^{d_\perp \alpha} \Gamma(2 - d_\perp \alpha) + \frac{x^2}{d_\perp \alpha - 2}}, \tag{3.36}$$

where $x \equiv \beta p a$ and $\Gamma(x)$ is the standard Gamma function. Unfortunately there is no analytic solution for general $d_\perp \alpha$, although one does exist for $d_\perp \alpha = 1, 2$. The case $d_\perp \alpha = 1$ physically represents network linkers on a filament confined to two dimensions, while $d_\perp \alpha = 2$ is either bundling linkers with $d_\perp = 1$ or network

linkers with $d_\perp = 2$. The equation of state with $d_\perp \alpha = 1$ is

$$p_c = \frac{-\rho T}{a W_{-1}(-\rho e^{\gamma})}, \tag{3.37}$$

where W_{-1} is the lower branch of the Lambert W function, with the lower branch chosen to ensure positive compressibility, and γ is the Euler-Mascheroni constant. For small argument $W_{-1}(x) \sim \log(-x)$ so the Casimir pressure is lower than the Tonks pressure Eq. 3.34 by a factor of $-\log(\rho a e^{\gamma})$. A plot of both pressures is shown in Fig. 3.2. The compressibility will also be smaller by this logarithmic factor, which in turn means density fluctuations should be larger by $-\log(\rho a e^{\gamma})$ for the Casimir gas relative to the Tonks gas in the dilute limit.

An explicit expression is likewise found for $d_\perp \alpha = 2$:

$$p_c = \frac{T e^{-\gamma - \frac{1}{\rho}}}{a}, \tag{3.38}$$

which displays very interesting non-analytic behavior as the line fraction $\rho \to 0$. This value is in fact critical in the sense that stronger interacting systems display discontinuous behavior in thermodynamic variables. To see this directly consider again Eq. 3.33 in the limit $p \to 0$, which must correspond to the dilute limit. For $d_\perp \alpha \leq 2$ one finds $\rho \to 0$, as expected. However, for larger values of $d_\perp \alpha$ the result is $\rho \to \rho_{crit} \equiv \frac{d_\perp \alpha - 2}{d_\perp \alpha - 1}$ at $p = 0$, *independent* of temperature. This is a direct result of the interaction energy scale being proportional to T, which allows the system to overcome the tendency to disorder (for sufficiently strong interactions) at all temperatures. Plots of pressure versus ρ for different values of $d_\perp \alpha$ are shown in Fig. 3.2.

3.2.4 Internal Energy and Entropy

The entropy of a one dimensional pairwise interacting gas can be found from Eq. 3.28 in a similar manner to the pressure by considering $\frac{df}{dT}$ and using the relation

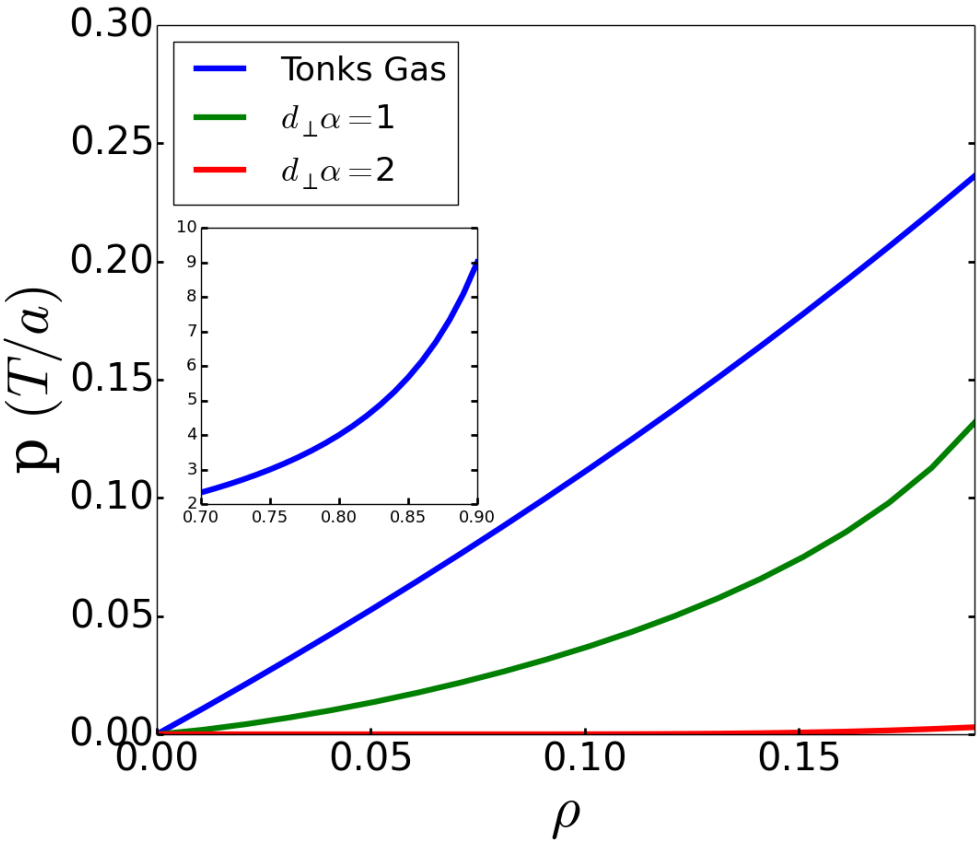

Figure 3.2: Pressure of a 1-D gas of particles interacting via the Casimir force versus line fraction. The hard core only Tonks gas $\alpha = 0$ is shown for reference. The attractive interaction dramatically reduces the pressure at small line fraction relative to an ideal gas. Inset: The hard core repulsion dominates at large densities and all curves will collapse onto the Tonks result.

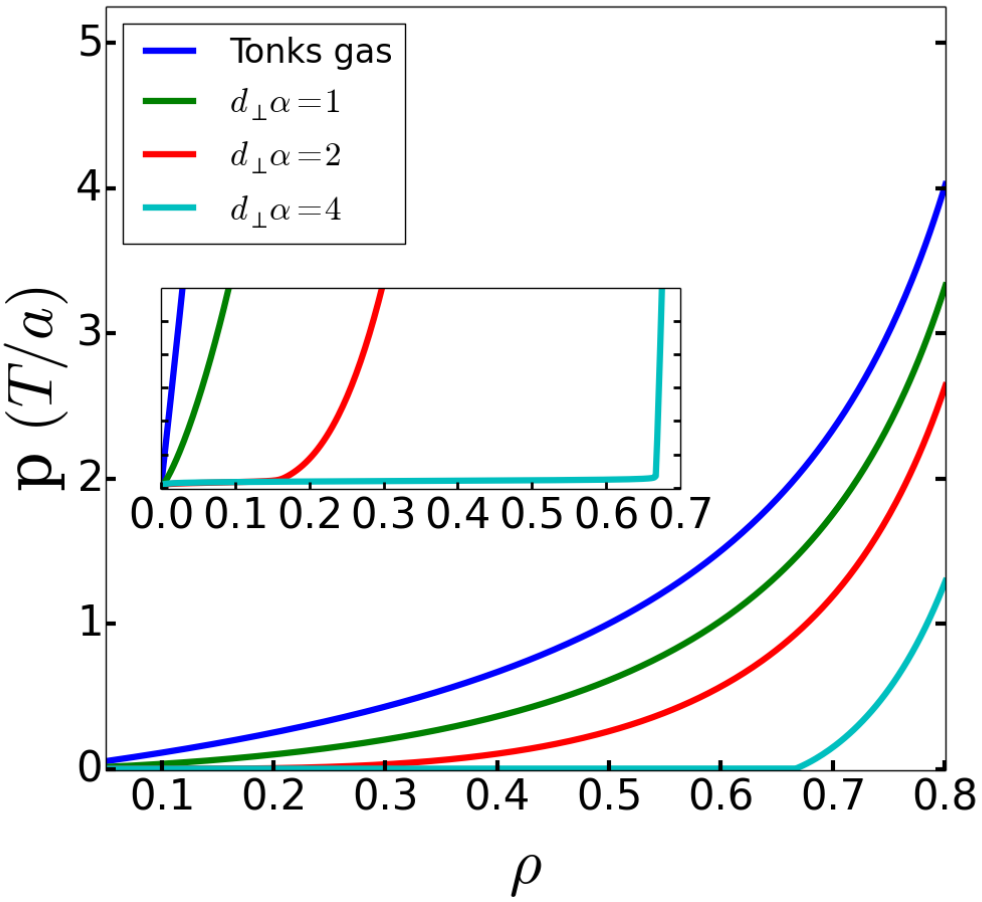

Figure 3.3: Pressure of a 1-D gas of particles with Casimir interactions versus line fraction. The hard core only Tonks gas is shown for reference. For $d_\perp\alpha \leq 2$ the pressure grows continuously from zero at zero line density, while for $d_\perp\alpha > 2$ the pressure experiences a slope discontinuity at nonzero line fraction.

$S = L\frac{\partial p}{\partial T}$. Explicitly

$$\frac{\partial p}{\partial T} = -\frac{\frac{\partial f}{\partial T}}{\frac{\partial f}{\partial p}} = \frac{\frac{\partial f}{\partial T}}{\frac{\partial f}{\partial \mu}/\frac{\partial p}{\partial \mu}} = \frac{NT}{L}\frac{\partial f}{\partial T}, \tag{3.39}$$

where Eq. 3.32 was used for the last equality. The resulting expression for the entropy is

$$S = -\frac{N\mu}{T} + \frac{N}{2} + \frac{pL}{T} + \frac{N}{T}\frac{\int_0^\infty \mathrm{d}x\, V(x) e^{-\beta p x} e^{-\beta V(x)}}{\int_0^\infty \mathrm{d}x\ e^{-\beta p x} e^{-\beta V(x)}}, \tag{3.40}$$

where the full chemical potential μ found from Eq. 3.28 is

$$\mu = -T \log\left[\frac{1}{\lambda_t}\int_0^\infty \mathrm{d}x\, e^{-\beta p x} e^{-\beta V(x)}\right]. \tag{3.41}$$

In the absence of an interaction Eq. 3.40 reduces to the familiar Sackur-Tetrode equation for the entropy of an ideal gas [Kar07]. The integral term in the entropy is due entirely to the interaction and is interpreted as $S_{int} = \frac{N<V>}{T}$ where the average is taken over a pair of interacting particles under an external pressure p. The dominant contribution to the integral in the numerator is for $x < \frac{1}{\beta p}$ and, assuming $V(x)$ is slowly varying, the integral will be proportional to $V(\frac{1}{\beta p})$. As the pressure is raised corresponding to an increase in volume fraction, we see that the per particle contribution to the entropy will decrease if $\frac{dV}{dx} > 0$, i.e. if the interaction is attractive. An explicit calculation of the interaction entropy gives

$$\begin{aligned} N d_\perp \alpha \frac{\int_a^\infty \mathrm{d}x\, x^{-d_\perp\alpha}\, \log x\, e^{-\beta p x}}{\int_a^\infty \mathrm{d}x\, x^{-d_\perp\alpha} e^{-\beta p x}} &= \frac{N d_\perp \alpha}{\Gamma(1-d_\perp\alpha, \beta p a)} \int_a^\infty \mathrm{d}x\, x^{-d_\perp\alpha}\, \log x\, e^{-\beta p x} \\ &= \frac{N d_\perp \alpha}{\Gamma(1-\alpha, \beta p a)} \left[\Gamma(1-d_\perp\alpha, \beta p a)\log a \right. \\ &+ \left. G^{30}_{23}\left(\beta p a \,\middle|\, \begin{matrix} 1 & 1 & \\ 0 & 0 & 1-d_\perp\alpha \end{matrix}\right)\right], \end{aligned} \tag{3.42}$$

where G is the Meijer G function. A plot of the entropy for different values of $d_\perp\alpha$ is shown in Fig. 3.4. As the rods approach close packing the number of states clearly decreases and the interaction plays no role. In the dilute limit strong interactions ($d_\perp\alpha \geq 2$) cause significant reductions in the entropy of the system. We may also calculate the internal energy of the Casimir gas using the

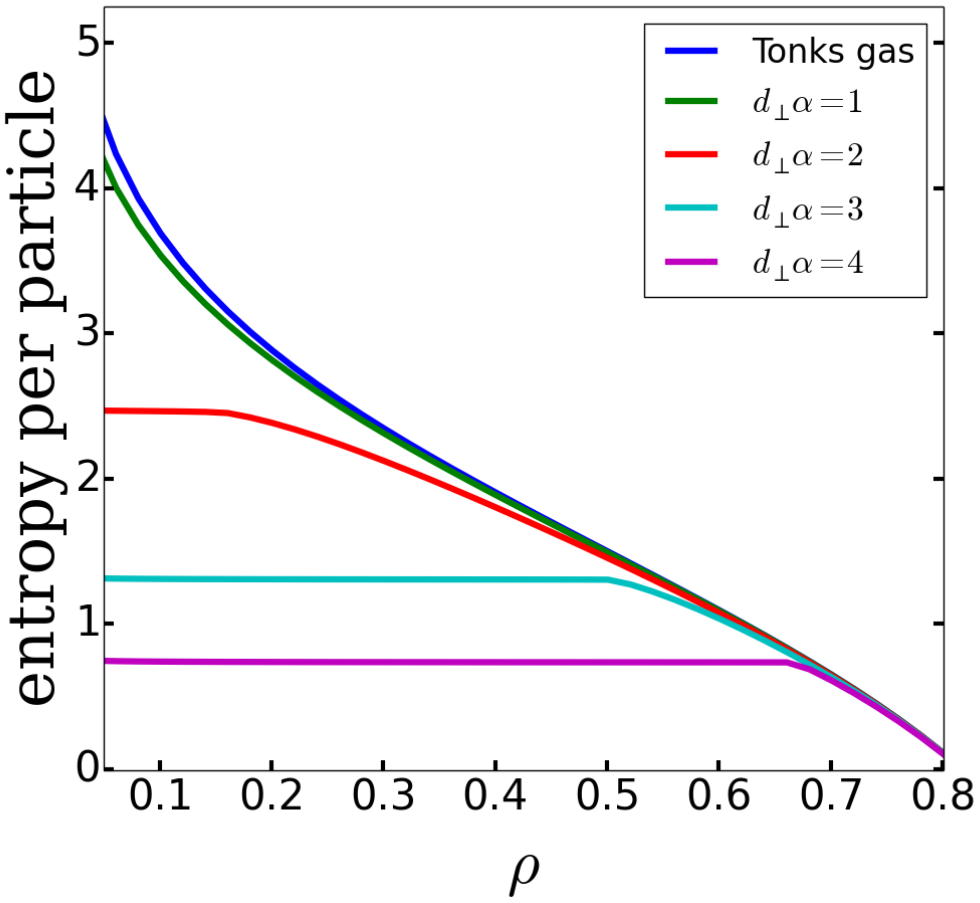

Figure 3.4: The configurational entropy of a 1-D gas as a function of line density. The curves collapse in the dense regime where the hard core repulsion dominates the attractive Casimir interaction. For sparse systems the reduction in entropy due to the pinning of filament fluctuations is apparent: The larger the coupling, i.e. the more restrictive the cross-linker, the larger the reduction.

thermodynamic relation

$$U = G + TS - pV = N\frac{\int_0^\infty \mathrm{d}x\, V(x) e^{-\beta p x} e^{-\beta V(x)}}{\int_0^\infty \mathrm{d}x\; e^{-\beta p x} e^{-\beta V(x)}} \tag{3.43}$$

The integral, which has already been calculated for the entropy, is evaluated to give

$$U = N d_\perp \alpha \frac{\Gamma(1 - d_\perp\alpha, \beta p a)\log a + G^{30}_{23}\left(\beta p a \,\middle|\, \begin{matrix} 1 & 1 & \\ 0 & 0 & 1 - d_\perp\alpha \end{matrix}\right)}{\Gamma(1 - d_\perp\alpha, \beta p a)} \tag{3.44}$$

The internal energy per particle for different values of α is shown in Fig. 3.5. Despite the appearance of the graph, higher values of $d_\perp\alpha$ (stronger attractive interactions) always correspond to lower internal energies in the very dilute limit. In fact, the limit of the internal energy per particle for $d_\perp\alpha \leq 1$ as $\phi \to 0$ diverges. The plateau in the $d_\perp\alpha = 2$ curve is due to the pressure being essentially zero for low volume fraction, letting the internal energy take its $\phi \to 0$ limiting value over a range of volume fractions.

3.2.5 Langmuir Isotherm

The Langmuir isotherm describes the adsorption of an ideal gas of particles onto a substrate at fixed temperature. Explicitly, the isotherm relates the coverage on the substrate to the pressure or concentration of the ideal gas through the relation $N = -\frac{\partial\Omega}{\partial\mu}$, where Ω is the grand potential. With $\Omega = -p(\beta,\mu)L$ the Langmuir equation can be rewritten as $\rho = a\frac{\partial p}{\partial\mu}$. The isotherm for the Tonk's gas, $d_\perp\alpha = 0$, is first derived for reference. The pressure of this hard-core gas is given implicitly in terms of μ by

$$\beta\mu = \beta p a + \log \beta p \lambda_t, \tag{3.45}$$

with solution

$$p = \frac{W_0\left(\frac{a e^{\beta\mu}}{\lambda_t}\right)}{\beta a}, \tag{3.46}$$

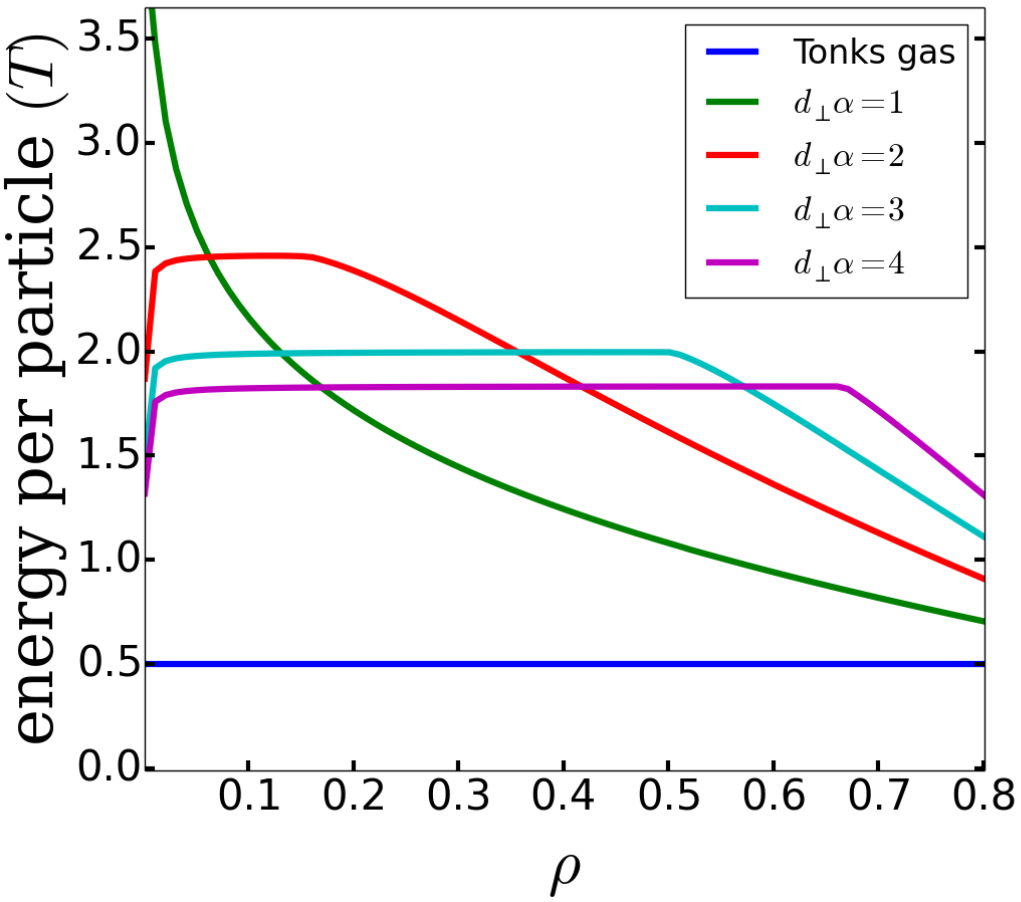

Figure 3.5: The internal energy per particle of a 1-D gas with Casimir interactions versus line density.

where $W_0(x)$ is the principal branch of the Lambert-W function, also known as the Product-Log function. The resulting Langmuir isotherm is

$$\rho = \frac{W_0\left(\frac{ae^{\beta\mu}}{\lambda_t}\right)}{1 + W_0\left(\frac{ae^{\beta\mu}}{\lambda_t}\right)}. \tag{3.47}$$

The limits are simple: For low chemical potential the adsorbed line density vanishes, while for $\mu \to \infty$ the system close packs. Due to the hard-core repulsion, the coverage is always less than the classical result for non-interacting rods. Extending the discussion to $d_\perp \alpha > 0$ by solving for the Isotherms numerically, the long-range nature of the Casimir interaction leads to a remarkable result in the thermodynamic limit: for sufficiently strong linker interactions $d_\perp \alpha > 1$, their line density vanishes when the linker chemical potential falls below the critical value $\mu \leq \mu_{crit} = T \log[\frac{\lambda_c}{\lambda_t}(d_\perp \alpha - 1)\,]$. Moreover, upon increasing μ past μ_{crit}, the line density jumps discontinuously from 0 to $\rho = \rho_{crit} = \frac{d_\perp \alpha - 2}{d_\perp \alpha - 1}$. Both of these results persist in finite length bundles (confirmed analytically by introducing a long distance cutoff to the interaction and through Monte Carlo simulations – see Sec. 3.3 and Fig. 3.9) leading to a continuous, but extremely sharp *condensation transition* in which linkers collectively bind to the bundle when their solution concentration is increased through the critical value: $c_{crit} : \mu(c_{crit}) = \mu_{crit}$. A similar transition occurs for linkers which restrict the torsional fluctuations of a larger bundle [SDB09], suggesting that nature may take advantage of fluctuation forces in many different contexts.

Given the attractive Casimir interaction, the decrease in linker density at small μ in the bundle with increasing α is surprising. At low density, however, adding another linker to the bundle introduces an entropic contribution to the free energy $\sim -T \log L/N$, but this can be more than offset by the loss in filament entropy, which is the source of the Casimir interaction, $\sim d_\perp \alpha T \log L/N$, leading to a net increase in free energy due to the additional linker. This is possible since both the translational entropy of the linker and its Casimir interactions are entropic and

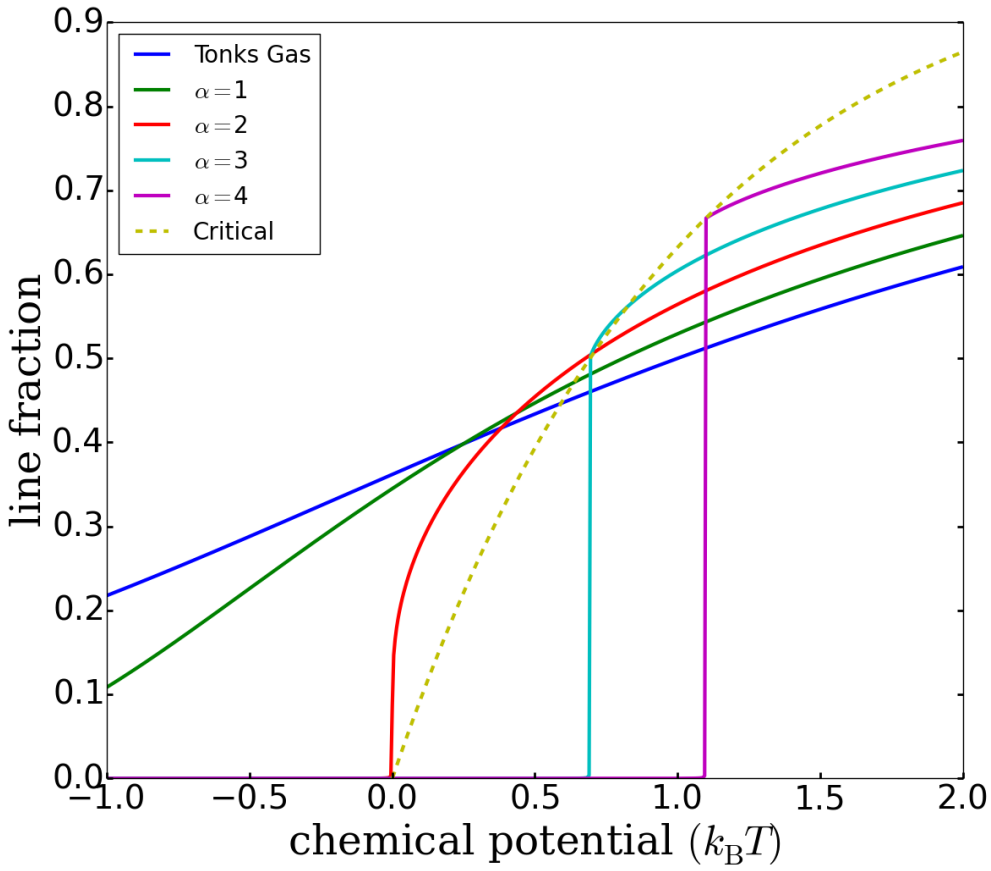

Figure 3.6: The coverage of an ideal gas being adsorbed onto a line with Casimir interactions plotted versus the chemical potential of the ideal gas. At low gas concentrations and high interaction strength it is entropically unfavorable for the particles to adsorb.

thus proportional to T.

3.3 Monte Carlo Simulations

The thermodynamic state functions of the previous section are verified with Monte Carlo techniques. Specifically, I simulate particles interacting with the pairwise Casimir interaction Eq. 3.18 on a line of length $L = 10^5 a$ in both the canonical and grand canonical ensembles. The walls at $x = 0$ and $x = L$ are assumed to interact with adjacent particles with the same potential. Random initial states are evolved with Metropolis–Hastings dynamics, wherein an initial state S is transformed to S', chosen with probability $f(S \to S')$ and accepted with probability $A(S \to S')$. To guarantee that the dynamics evolve an arbitrary state to the equilibrium configuration, the distributions f and A must be chosen to satisfy the detailed balance condition

$$\frac{P(S \to S')}{P(S' \to S)} = \frac{P(S')}{P(S)}, \tag{3.48}$$

where $P(S)$ is the equilibrium probability distribution and $P(S \to S')$ is the transition rate from S to S'. In the simulated dynamics the transition rate is simply $A(S \to S') \times f(S \to S')$, and upon insertion into Eq. 3.48 one finds the relation

$$\frac{A(S \to S')}{A(S' \to S)} = \frac{P(S') f(S' \to S)}{P(S) f(S \to S')}. \tag{3.49}$$

Metropolis proposed an acceptance rate of the form

$$A(S \to S') = \min\left(1, \frac{P(S') f(S' \to S)}{P(S) f(S \to S')}\right), \tag{3.50}$$

which clearly satisfies the detailed balance condition. To make further progress one must specify both the form of the equilibrium distribution and the specific form of the steps, thus determining $P(S)$ and $f(S \to S')$, respectively.

To model the Casimir gas, consider a state S_N specifying the positions of N indistinguishable particles on the line. The underlying probability distribution

$P(S_N)$, given by elementary statistical mechanics, is proportional to $e^{\beta(\mu N - E_N)}$, where $\beta = 1/k_{\rm B}T$ is the inverse temperature, μ is the chemical potential, and E_N is the energy. The state is evolved by two distinct steps:

1. The translation of a randomly chosen particle to another position on the line.

2. The insertion of a particle in a random position on the line or deletion of a randomly chosen particle, both occurring with probability $\frac{1}{2}$.

The probability distribution for selecting a particular translation is $f(S_N \to S'_N) = 1/NL$, where S'_N denotes an N particle state with one particle in a different location. This expression is simply the product of the probability of selecting a particular particle at random $(1/N)$ and moving it to a random location $(1/L)$. Since this distribution is the same for the reverse process, the required acceptance rate is

$$A_{translation}(S_N \to S'_N) = \min\left(1, e^{-\beta(E'_N - E_N)}\right), \tag{3.51}$$

where I have used the known form of $P(S_N)$. The second step is necessary to model the system in the Grand Canonical ensemble because it explicitly allows for number fluctuations. The probability of insertion is given by $f(S_N \to S_{N+1}) = \frac{1}{2L}$, where the 1/2 factor represents choosing between insertions and deletions. Likewise, the probability of the reverse step is $f(S_{N+1} \to S_N) = \frac{1}{2(N+1)}$. This gives the acceptance rate of insertions

$$A_{\rm ins}(S_N \to S_{N+1}) = \min\left(1, \frac{L}{N+1} e^{\beta\mu} e^{-\beta(E_{N+1} - E_N)}\right), \tag{3.52}$$

and rate of deletions

$$A_{\rm del}(S_N \to S_{N-1}) = \min\left(1, \frac{N}{L} e^{-\beta\mu} e^{-\beta(E_{N-1} - E_N)}\right). \tag{3.53}$$

To verify the equation of state found in Eq. 3.33, I attach stiff harmonic springs to the walls at $x = 0$ and $x = L$ and deduce the pressure of the gas by

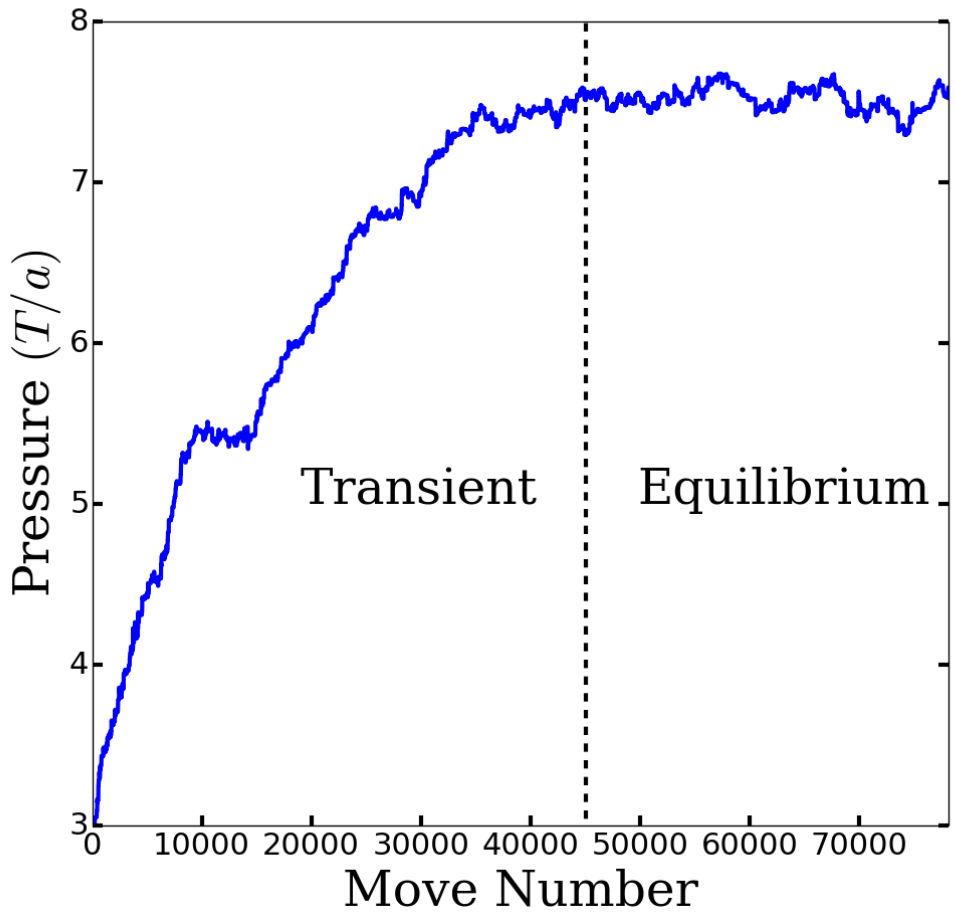

Figure 3.7: Trace of the pressure in the canonical ensemble. After an initial transient the pressure fluctuates around its equilibrium value.

sampling the separation of the walls. A typical trace of the pressure is shown in Fig. 3.7. Equilibrium was achieved after an initial transient lasting approximately 5×10^4 steps. An additional 2×10^6 moves were performed and a sample of the pressure was taken every 1000 steps. This process was repeated for line densities in the range $[0, .8]$ and for different values of $d_\perp \alpha$. The results are shown in Fig. 3.8 and it is clear that the Monte Carlo simulation confirms the equation of state found numerically. Allowing particles to come on and off the line at fixed chemical potential probes the system in the Grand Canonical ensemble. The translation

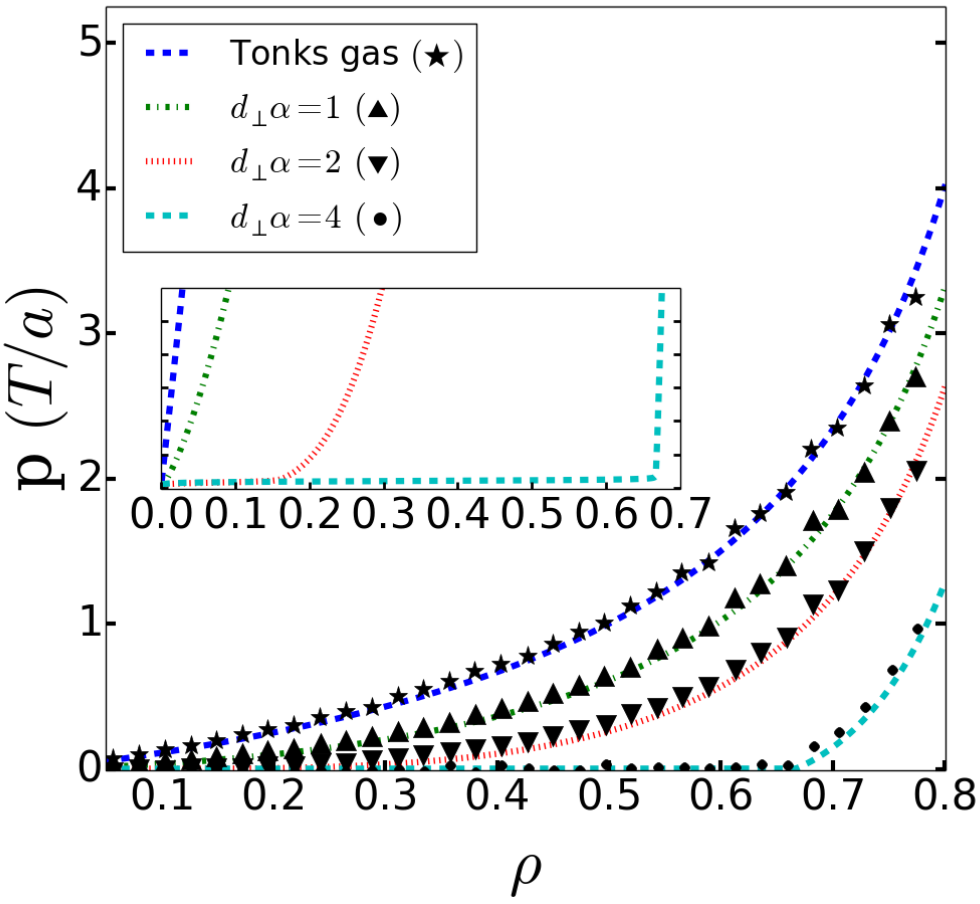

Figure 3.8: The simulated equation of state compared with analytical solutions.

step was also included so that the system would maintain mechanical equilibrium. After an initial transient abated, the line density was sampled at fixed intervals for different values of the coupling $d_\perp \alpha$ and chemical potential μ. The results are plotted alongside the Langmuir Isotherm obtained numerically in Fig. 3.9, and once again the simulations are in agreement with the numerics. The largest discrepancies occur near the condensation transition and are likely due to finite size scaling, i.e. they would be removed as the system size was increased. This is explored in greater detail in the following section, Sec. 3.4, where large-scale finite element simulations are employed.

3.4 Finite Element Simulations

We explored the role of Casimir interactions in more complicated bundles via large-scale finite-element simulations. We simulated a single central filament surrounded by six outer filaments, all subject to hinged boundary conditions at one end – see Fig. 3.10. This avoids the potential for frustrated dynamics associated with bundle formation, and focuses on the equilibrium adsorption isotherms. All filaments together offer $N_b = 4207$ binding sites. Except for finite size scaling tests with halved filament length and persistence length, the filaments' mechanical properties remain the same as in Section 2.4.2.2. The cross-linkers, which may form transient connections between filaments, exist in three distinct chemical states: free (in solution), singly bound, and doubly bound. The transitions between these states are governed by Poisson processes with rate constants k_{on} and k_{off} for association and dissociation of the bonds, respectively. Both the bundle and the linkers are located within a cubic simulation box, whose faces are equipped with periodic boundary conditions. The number of linkers in solution is approximately twenty-five times higher ($N_l \sim 50000$) than the maximal number of doubly bound linkers ($N_{db} \sim 2000$), ensuring an approximately constant free

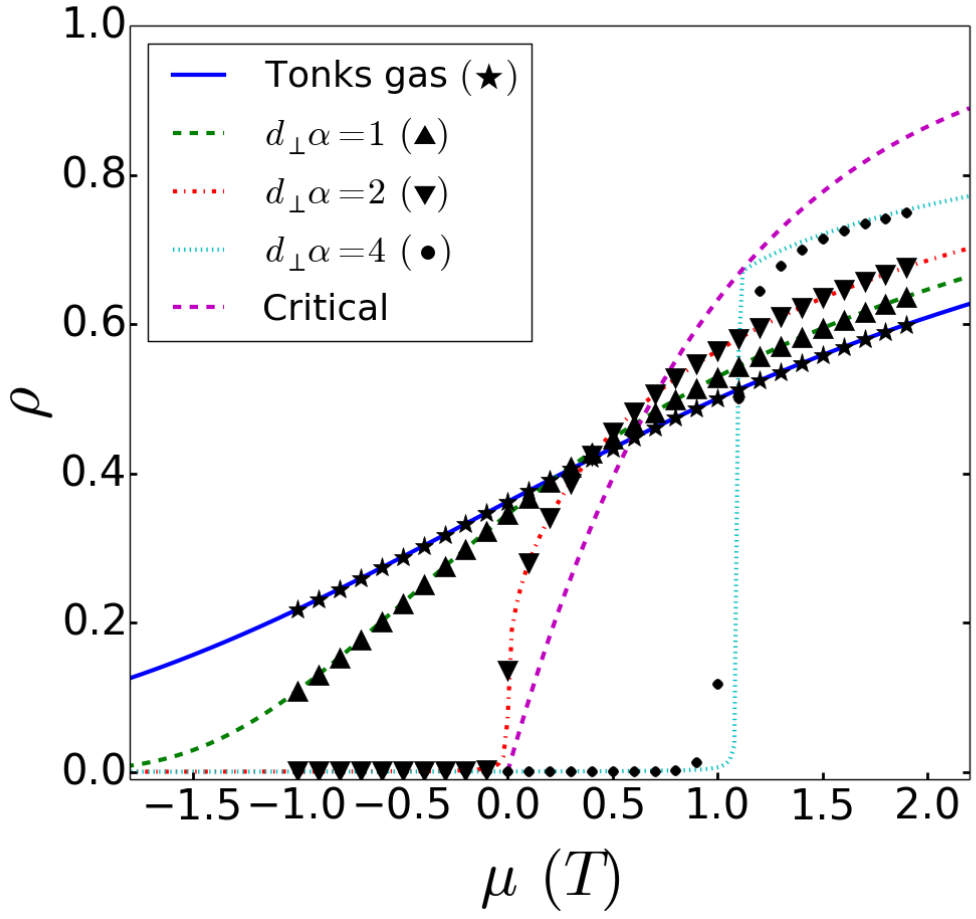

Figure 3.9: The density of a casimir gas in equilibrium with an ideal gas of crosslinkers at fixed chemical potential. For $\alpha > 2$ the system undergoes a first order phase transition in the thermodynamic limit: The crosslinkers spontaneously condense to the critical density $\rho_{crit} = \frac{\alpha-2}{\alpha-1}$ at $\mu_{crit} = k_\mathrm{B}T \log \frac{\lambda_c}{\lambda_t}\alpha - 1$.

linker chemical potential. The stochastic dynamics of the linkers as well as their reaction kinetics are described in [CMS13]. We chose cross linkers that pin the slope of the filaments ($\alpha = 2$) at fixed concentration (therefore fixed chemical potential), and allowed the filaments to move in three dimensions ($d_\perp = 2$), so that the prefactor of the Casimir interaction was $d_\perp \alpha = 4$.

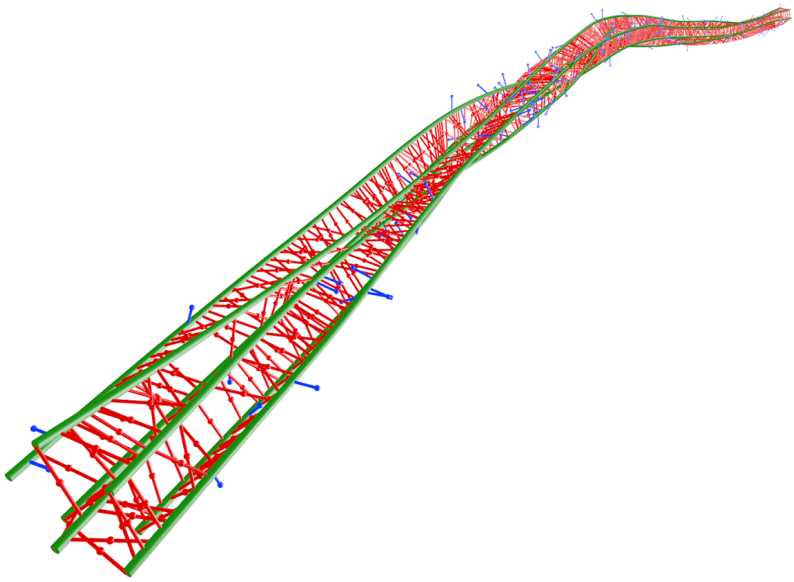

Figure 3.10: The geometry of the finite element bundle simulation. A single semi-flexible filament is surrounded by 6 neighbors, which may cross-link to each other as well as the central filament. All filaments are subjected to hinged boundary conditions at one end, while the other remains free. The bundle is shown in a highly saturated state.

The Langmuir isotherms for simulations of two different length bundles are shown in Fig. 3.11 alongside best theoretical fit (dot-dashed, green line) with two free parameters: a trivial horizontal shift representing a choice of reference chemical potential, and a vertical scaling which effectively tunes the strength of the hard-core repulsion. For comparison we also plot the best fit Langmuir isotherm for a Tonks gas (dashed, blue line) showing that, without the Casimir

interaction, one cannot account for the sharpness of the condensation transition. As the bundles are made longer (filled triangles) the transition is observed to become even sharper in the simulation, suggesting that the observed rounding is a finite size effect. The large error bars near the transition indicate significant density fluctuations. These may be understood by inverting Eq. 3.33 to give the pressure in terms of of density, as shown in Fig. 3.8. Bound linker number fluctuations $\langle(\Delta N)^2\rangle/N^2$ are proportional to $\left(\frac{\partial p}{\partial L}\right)^{-1} = -L^2N^{-1}\left(\frac{\partial p}{\partial \rho}\right)^{-1}$. For $d_\perp\alpha > 1$ the derivative of the pressure with respect to density vanishes at small densities resulting in large density fluctuations.

3.5 Statistical Treatment of the Casimir Gas

The approach thus far has focused on a thermodynamic treatment of the interacting Casimir gas, which has been sufficient to understand the condensation transition in bundles. An alternate approach is to study the statistical distribution of the particles on the line by continuing the derivation given in Sec. 3.2.2.

Consider the same partition function of N particles on a line of length L interacting with the pairwise potential V as in previous sections:

$$\begin{aligned} Z_N(L) &= \int\cdots\int_{0<x_1<x_2<\cdots<x_N<L} \mathrm{d}x_1\cdots\mathrm{d}x_N \exp\left\{-\beta\left[V(x_1)\right.\right. \\ &+ \left.\left. V(x_2-x_1)+\cdots+V(L-X_N)\right]\right\}, \end{aligned} \tag{3.54}$$

which may be written more succinctly in terms of a Laplace variable s

$$\begin{aligned} Z_N(s) &= [\Omega(s)]^N \\ \Omega(s) &= \int_0^\infty e^{-sx-\beta V(x)}\,\mathrm{d}x. \end{aligned} \tag{3.55}$$

Instead of relating this result to a thermodynamic potential, we advance the discussion by writing the partition function in terms of a Bromwich integral

$$Z_N(L) = \frac{1}{2\pi i}\int_{c-i\infty}^{c+i\infty} e^{sL}\Omega^{N+1}(s)\,\mathrm{d}s, \tag{3.56}$$

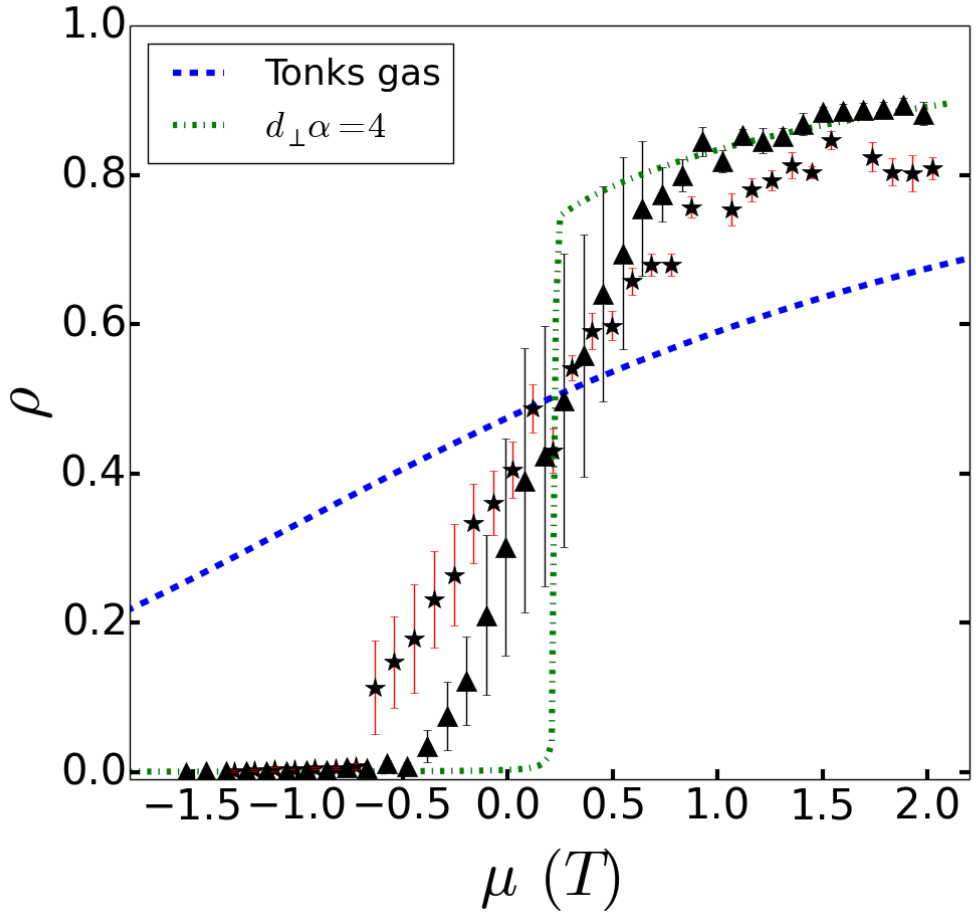

Figure 3.11: (color online) Theoretical and simulated Langmuir isotherms of linkers adsorbed onto a filament bundle. (★) Simulation data for a 5μm bundle with persistence length $l_p = 9.2\mu$m. (▲) Both the system size and the persistence length doubled to study finite size scaling effects. The transition is noticeable sharper and is approaching the expected thermodynamic limit.

where c is any real number greater than the largest pole of $\Omega^{N+1}(s)$. Expressions for the pair distribution functions $\rho^{(1)}(r) = \sum_i \langle \delta(r_i - r) \rangle$, $\rho^{(2)}(r, r') = \sum_{i,j} \langle \delta(r_i - r)\delta(r_j - r') \rangle$, and $\cdots$ $\rho^{(n)}(r, r', r'', \cdots)$ may be derived in a similar manner. Since we are interested in a pairwise, non spatially dependent potential we must have that $\rho^{(1)}(r) = \frac{N}{L} = \rho$ since $\rho^{(1)}(r)$ is the density distribution. The pair distribution function $\rho^{(2)}(r, r')$ is more interesting since it quantifies spatial correlations and is also responsible for determining the thermodynamic properties of the system. Exact results may be derived In the limit $N \to \infty$ following [SZK53]

$$\rho^{(2)}(R) = \rho \sum_{n=1}^{\infty} \frac{1}{2\pi i} \int_{c-i\infty}^{c+i\infty} e^{R(s-c)} \left[\frac{\Omega(s)}{\Omega(c)} \right]^n \mathrm{d}s, \tag{3.57}$$

where $R \equiv r' - r$ and the constant c is determined by the solution of Eq. 3.33 for βp. Each term in the sum represents a contribution due to a different adjacency. In other words, the full distribution function has been decomposed into a sum over nearest neighbors, next nearest neighbors, etc. If the gas particles have a finite size a then the sum cannot extend to infinity since it is impossible to place an infinite number of particles a finite distance apart. We therefore append the result with a theta function to accommodate hard core particles:

$$\rho^{(2)}(R) = \rho \sum_{n=1}^{\infty} \frac{\Theta(R - na)}{2\pi i} \int_{c-i\infty}^{c+i\infty} e^{R(s-c)} \left[\frac{\Omega(s)}{\Omega(c)} \right]^n \mathrm{d}s. \tag{3.58}$$

3.5.1 Tonks gas distribution function

It is instructive to calculate the full radial distribution function for the hard core Tonk's gas. The pressure of a Tonks gas, found using e.g. Feynman's method, determines the constant c

$$c = \beta p = \frac{\rho}{a(1 - \rho)}. \tag{3.59}$$

Plugging the hard core potential into Eq. 3.55 we find $\Omega(s) = \frac{e^{-sa}}{s}$. All that remains is the Bromwich integral

$$I_n = \frac{1}{2\pi i} \int_{c-i\infty}^{c+i\infty} e^{Rs} \Omega^n(s) \, \mathrm{d}s = \frac{1}{2\pi i} \int_{c-i\infty}^{c+i\infty} \frac{e^{(R-na)s}}{s^n} \, \mathrm{d}s. \tag{3.60}$$

The integral may be evaluated using the theory of residues. Analytically continue the integrand into the complex plane and consider a contour along the line $[c - i\infty, c + i\infty]$ closed by a semicircle of radius b in the left half plane. Since $R \geq na$ by the Θ function in Eq. 3.58 the contribution along the left part of the semicircle will vanish as $b \to \infty$. Likewise, the top and bottom portions of the semicircle will contribute nothing since $\Omega(s) \sim \frac{1}{s}$. Since $c \geq 0$ the contour will enclose the n^{th} order pole at the origin. The residue is

$$\mathrm{Res}_n(s = 0) = \frac{(R - na)^{n-1}}{(n-1)!}, \tag{3.61}$$

which can be seen by Taylor expanding the exponential in the integrand. By the residue theorem we have that the integral Eq. 3.60 evaluates to

$$I_n = \frac{(R - na)^{n-1}}{(n-1)!}. \tag{3.62}$$

The distribution function is

$$\rho^{(2)}(R) = \sum_{n=1}^{\infty} \frac{N\Theta(R - na)}{L} \frac{(R - na)^{n-1}}{(n-1)!} \left(\frac{\rho}{a(1-\rho)}\right)^n \exp\left[-\frac{\rho(R - na)}{a(1-\rho)}\right] \tag{3.63}$$

A plot of the Tonks distribution function is shown for two different volume fractions in Fig. 3.12. For $\rho << 1$ the distribution is flat and resembles an ideal gas. For $\rho \sim 1$ the system is fully packed and the distribution function shows the expected crystalline order.

3.5.2 Casimir gas distribution function

We need to calculate the same quantities as for the Tonks gas. We have that $\Omega(s) = s^{\alpha-1}\Gamma(1 - \alpha, sa)$ and the constant c is given by the solution of

$$\rho = c\frac{\Gamma(1 - \alpha, ca)}{\Gamma(2 - \alpha, ca)}. \tag{3.64}$$

The integral we need to evaluate is

$$I_n = \frac{1}{2\pi i} \int_{c-i\infty}^{c+i\infty} \mathrm{d}s\, e^{Rs} \left[s^{\alpha-1}\Gamma(1 - \alpha, sa)\right]^n. \tag{3.65}$$

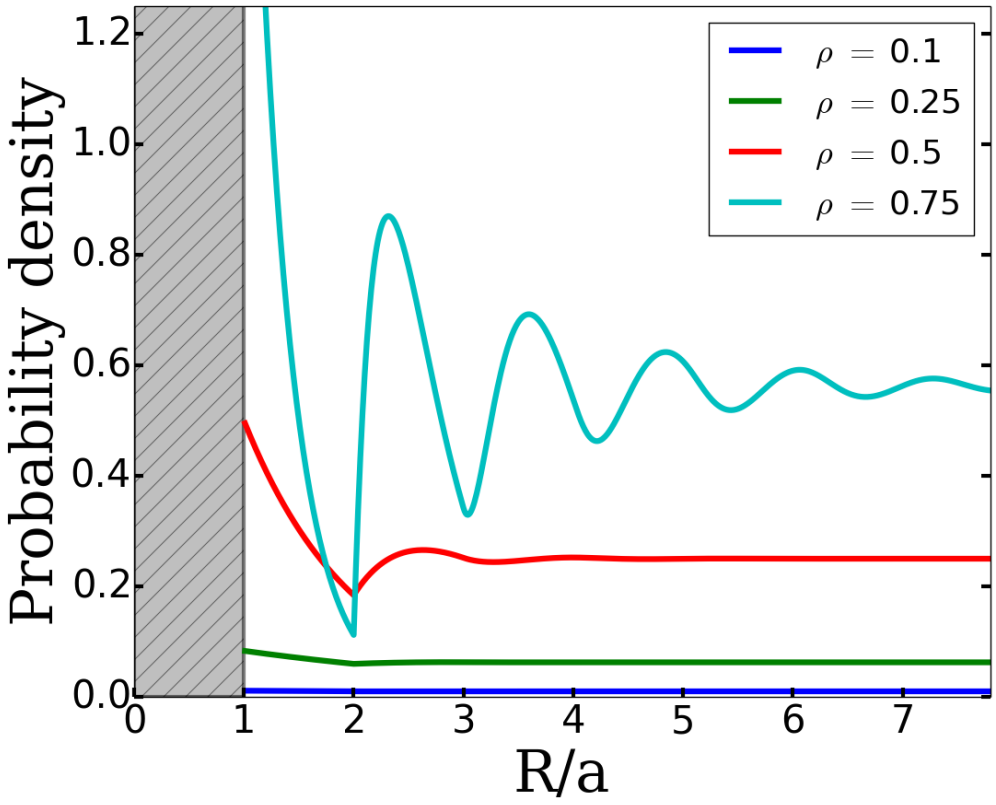

Figure 3.12: The radial distribution function for a Tonks gas for different values of the line density. The x axis is $\frac{R}{a}$ so that distance is measured in particle number. The probability density is zero inside of the hard core region (shaded rectangle) and approaches ρ^2 for large R.

First examine these expressions in the dense limit. This limit corresponds to high pressures and therefore high values of the constant c. Integration by parts gives the series expansion for the incomplete gamma function at large second argument: $\Gamma(s,x) \sim e^{-x}x^{s-1}$. In this limit Eq. 3.64 reduces to the Tonks relation Eq. 3.59 and likewise the bromwich integral Eq. 3.65 likewise reduces to the appropriate Tonks expression. The Casimir interaction is overwhelmed by the steric interaction for any α.

In the dilute limit the Casimir interaction is responsible for a considerable amount of structure in the distribution function. Analytic expressions for c in the sparse limit have been found previously for $\alpha = 1, 2$ (Eq. 3.37,3.38). Once again there is no representations of the solution of Eq. 3.64 in terms of elementary functions for general α. The incomplete gamma function introduces a branch cut in the Bromwich integral Eq. 3.65 which we choose to be along the negative real axis. We turn the line integral into a contour integral by closing in the left half plane with a key-hole contour along the branch cut. For large $|s|$ the integral looks the same as the Tonks gas $\frac{\exp[(R-na)s]}{s}$ and we see that the semi-circle contour in the left half plane has no contribution as its radius is taken to infinity and likewise the top and bottom portions of the integral vanish since $\Omega(s) \sim \frac{1}{s}$. The full integral is then given by the discontinuity along the branch cut. To the best of our knowledge there is no closed form expression for this integral for general n so we will examine just the first few values $n = 1, 2$ in detail. Since n refers to the distribution of finding your nth nearest neighbor some distance away there is physically relevant information in this expansion. In particular if one considers the full distribution function for distances less than $\frac{n}{\rho}$ only the first n terms of Eq. 3.58 will give meaningful contributions. In the limit $\rho \to 0$ only $n = 1$ contributes so we examine that first. The branch cut integral will be dominated by small s due to the exponential suppression so we expand the incomplete gamma function

for small second argument and find:

$$\begin{aligned} I_n &= \frac{-1}{2\pi i}\left\{\int_{-\infty+i\epsilon}^{i\epsilon} \mathrm{d}s\, e^{Rs}\left[s^{\alpha-1}\Gamma(1-\alpha) - \frac{1}{1-\alpha} + \frac{s}{2-\alpha} + \cdots\right]\right. \\ &- \left.\int_{-i\epsilon}^{-\infty-i\epsilon} \mathrm{d}s\, e^{Rs}\left[s^{\alpha-1}\Gamma(1-\alpha) - \frac{1}{1-\alpha} + \frac{s}{2-\alpha} + \cdots\right]\right\} \\ &= \frac{-1}{2\pi i}\int_{-\infty}^{0} \mathrm{d}s\, \left[f(s+i\epsilon) - f(s-i\epsilon)\right], \end{aligned} \tag{3.66}$$

where $\Gamma(x)$ is the standard Gamma function and the higher order terms contain simple poles at all positive integer values of α which cancel the corresponding simple pole in the Gamma function. At this point it is most instructive to look at particular cases.

3.5.2.1 $\alpha = 1$

In the limit $\alpha \to 1$ the integrand in Eq. 3.66 is $f(s) = e^{Rs}\,(-\ln sa - \gamma + sa)$. Analytically continuing the log we find the discontinuity is $-2\pi i e^{Rs}$ so that our integral is

$$I_1(\alpha = 1) = \frac{-1}{2\pi i}\int_{-\infty}^{0} \mathrm{d}s\, -2\pi i e^{Rs} = \frac{1}{R}. \tag{3.67}$$

Recalling that for $\alpha = 1$ the constant c is given by Eq. 3.37 multiplied by β we have that the n=1 term in the radial distribution function is

$$\rho_1^{(2)}(R) = \rho \frac{\exp\left[\frac{\rho R}{W_{-1}(-\rho a e^{\gamma})}\right]}{R\,\Gamma(0, \frac{-\rho R}{W_{-1}(-\rho a e^{\gamma})})}\Theta(R-a). \tag{3.68}$$

The computation of higher order terms in n is limited only by time and integration skills. The distribution function including $n = 1$ and $n = 2$ is shown in Fig 3.13 alongside the Tonks distribution for reference.

3.5.2.2 $\alpha = 2$

For $\alpha = 2$ the integrand in Eq. 3.66 is $f(s) = e^{Rs}\,(1 + (\gamma - 1)sa + sa\,\ln sa)$. Analytically continuing the log we find the discontinuity is $2\pi i\, sa\, e^{Rs}$ so that our

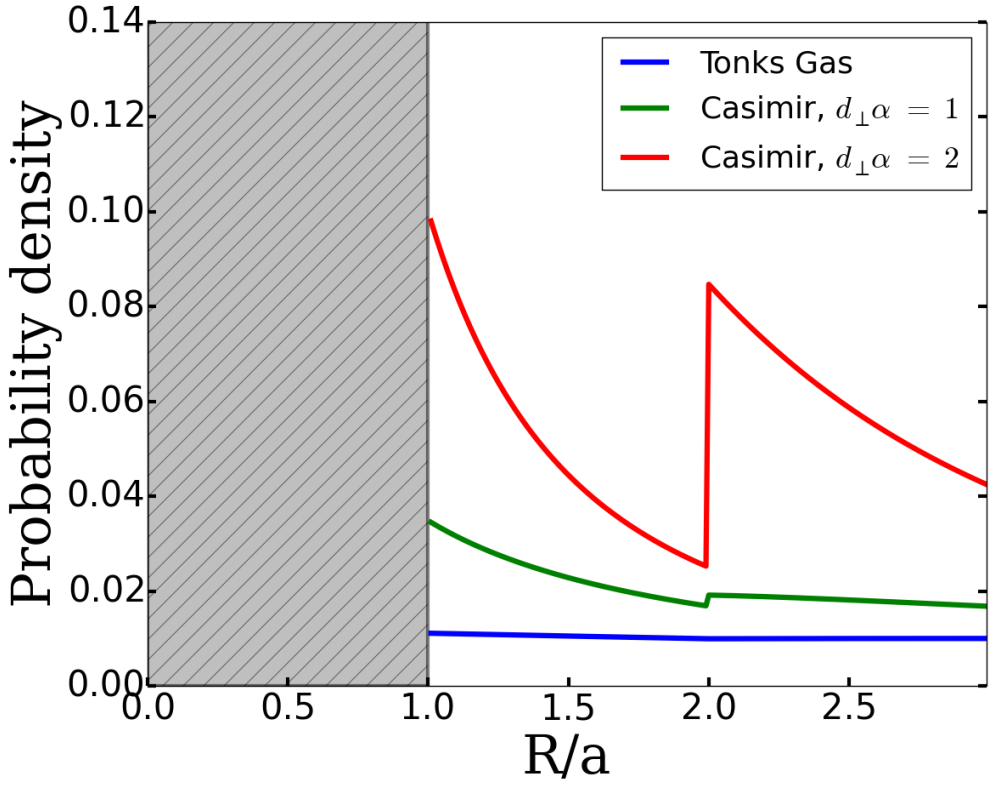

Figure 3.13: The sum of the first two terms of the analytical approximation to the radial distribution function for a Casimir gas with $\rho = .1$. The Tonks distribution shown for reference. The x axis is $\frac{R}{a}$ so that distance is measured in particle number.

integral is

$$I_1(\alpha = 1) = \frac{-1}{2\pi i} \int_{-\infty}^{0} \mathrm{d}s \, 2\pi i \, sa \, e^{Rs} = \frac{a}{R^2}. \tag{3.69}$$

Recalling that for $\alpha = 2$ the constant c is given by Eq. 3.38 multiplied by β we have that the n=1 term in the radial distribution function is

$$\rho_1^{(2)}(R) = \rho \frac{a^2 \exp\left[\frac{-Re^{-\gamma-\frac{1}{\rho a}}}{a}\right]}{R^2 e^{-\gamma-\frac{1}{\rho a}} \, \Gamma(-1, \frac{Re^{-\gamma-\frac{1}{\rho a}}}{a})} \Theta(R-a). \tag{3.70}$$

Higher order terms can likewise be calculated. A plot of the first two terms is shown in Fig. 3.13. Doubling the strength of the interaction has considerable impact on the distribution function, with ordering/clustering appearing at relatively low concentrations. It can be expected that the physically relevant $\alpha = 4$ will have a strong tendency to cluster and that it will have an $n = 1$ distribution function $\sim \frac{\rho a^4 \exp -R/a}{R^4}$. One may also evaluate the pair distribution function using numerical results for the pressure, as shown in Fig. 3.14.

3.6 Conclusions

Although highly nonequilibrium systems, cells may take advantage of *equilibrium* Casimir interactions to control cytoskeletal structure. The discontinuous condensation transition suggests that cells may be able to exploit this strongly interacting system to effect dramatic topological rearrangements of the cytoskeleton via small changes in the concentration of cross linking proteins. The difference in elastic response of filament networks and bundle networks is stark [MWB14] and potentially amenable to precise chemical control if linker concentrations are tuned to a high susceptibility point near $\mu = \mu_{crit}$. Alternatively, cells may tune these concentrations far from the transition to effectively decouple cytoskeletal topology and linker concentration.

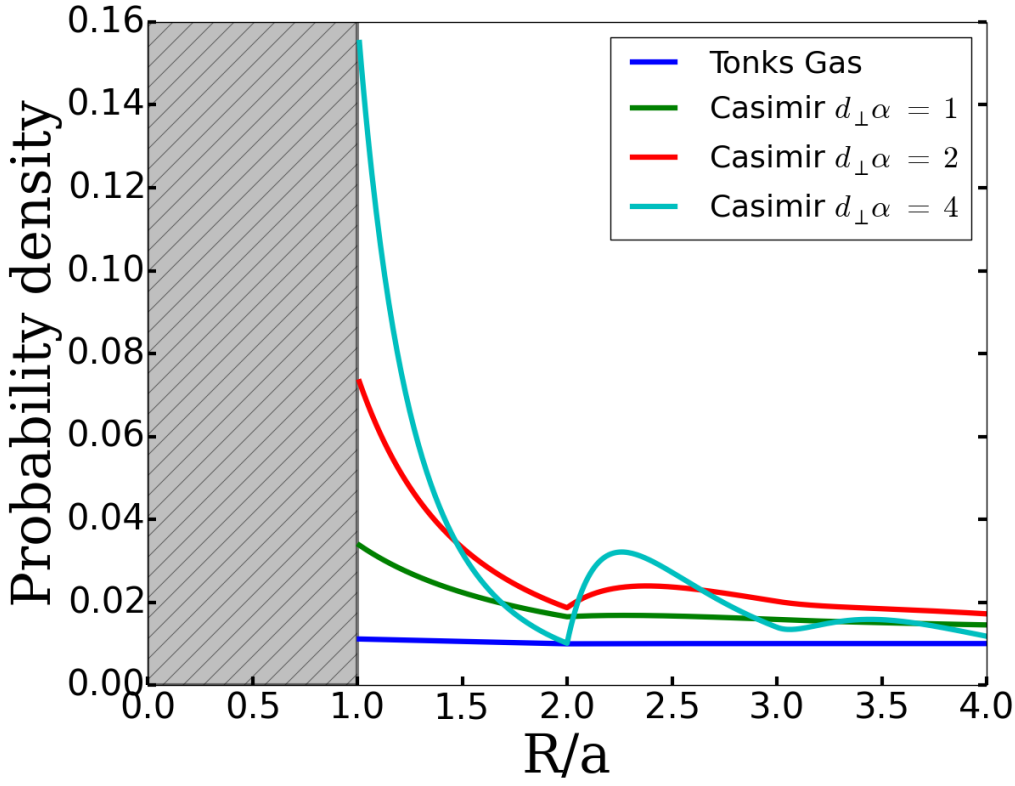

Figure 3.14: The numerically evaluated radial distribution function for a Casimir gas with different values of $d_\perp\alpha$ at fixed $\rho = .1$. The Tonks solution is shown for reference. The x axis is $\frac{R}{a}$ so that distance is measured in particle number. The probability density is zero inside of the hard core region (shaded rectangle) and approaches ρ^2 for large R.

CHAPTER 4

Critical Non-Equilibrium Networks

While the previous chapters have explored the importance of *equilibrium* fluctuation effects in cross-linked polymer networks, here I will study networks which have been actively driven far from equilibrium. Cellular systems, which are naturally found in non-equilibrium states, provide the inspiration for the models studied in this chapter. Section 4.1, which focuses on the role of active noise within elastic networks, is meant to model the role motor proteins plays within the cytoskeleton. The motors are assumed to randomly drive the network, although the persistence of the motors suggests that this noise will be correlated or *colored*. Treating the network as a scalar elastic continuum, I study the system with Renormalization Group techniques and show that it displays dynamic critical behavior. Section 4.2 explores the effect of *soft modes*, which have zero restoring force, on the mechanics of isostatic networks. In cross-linked polymer systems, the soft modes are the anomalously soft bending modes, which are orders of magnitude more compliant than the stretching modes. Invoking a correspondence with jammed emulsions, I study a kinetic model of the rigidity transition in the network, and predict a nonlinear strain stiffening with $G \sim \gamma$, where G is the shear modulus and γ is the applied strain.

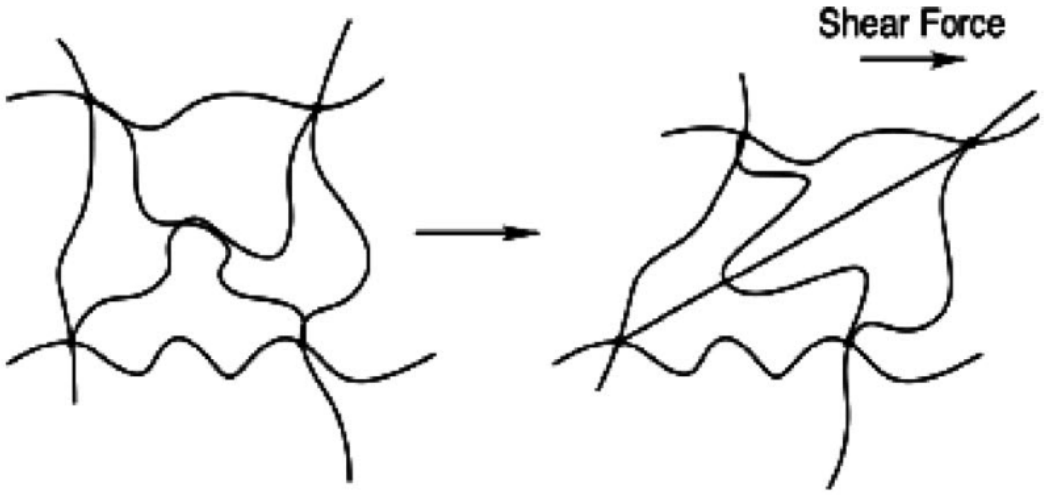

Figure 4.1: Cross-linked Biopolymer networks are intrinsically nonlinear due to the underlying constituent filaments: They can support large tensile stresses but buckle easily. From Kang 2009 [KWJ09]

4.1 Active noise in elastic networks

4.1.1 Elastic description of cross-linked biopolymer networks

Biopolymer networks display rich mechanical behavior due in part to their highly nonlinear elastic response. For example, when subjected to external shear stress the networks have been observed to rapidly strain stiffen and develop negative normal stresses [MKJ95, HLM03, CMS13] . The origin of the nonlinearity is the asymmetric response of semi-flexible polymers to applied load: They can support large tensile stresses but buckle easily under compression–See Fig. 4.1. Cross linkers are necessary to transmit the stresses through the network, allowing access to the nonlinear regime. A further source of nonlinearity is the network composition. Networks are observed in multiple phases, including amorphous networks of single filaments, lamellar configurations, and networks of bundles. The cross linkers again play a key role in deciding which phase is thermodynamically favorable, as was discussed in detail in Chapter 2.

At large scales, however, the cross-linkers must drop out of the description of the network and what remains may be treated as an elastic continuum. Here I derive the most general isotropic quartic free energy of an elastic body, which is sufficient to explain the nonlinear effects mentioned above.

Consider the deformations of an elastic body described by the right Cauchy strain tensor $u_{ij} = \frac{1}{2}(\partial_i u_j + \partial_j u_i + \partial_i u_k \partial_j u_k)$, where $\mathbf{u(x)}$ is the deformation field. The strain tensor transforms as a rank 2 tensor under rotations of the reference space and as a scalar under rotations of the target space. If one considers an isotropic reference state, appropriate for biopolymer networks, then the free energy must be invariant with respect to rotations in either space. This requires each term to be fully contracted in the strain field, i.e. to be composed of products of $\mathrm{Tr}\underline{\underline{u}}^n$ for $n = 1, 2, ...$ The most general form to quartic order is

$$\begin{aligned} F_{\mathrm{iso}}[\underline{\underline{u}}] &= \int \mathrm{d}^d\mathbf{x} \frac{\lambda}{2}(\mathrm{Tr}\underline{\underline{u}})^2 + \mu \mathrm{Tr}\underline{\underline{u}}^2 + c_1 \mathrm{Tr}\underline{\underline{u}}^3 + c_2(\mathrm{Tr}\underline{\underline{u}})^3 + c_3 \mathrm{Tr}\underline{\underline{u}}\mathrm{Tr}\underline{\underline{u}}^2 \\ &+ c_4 \mathrm{Tr}\underline{\underline{u}}^4 + c_5(\mathrm{Tr}\underline{\underline{u}})^4 + c_6 \mathrm{Tr}\underline{\underline{u}}\mathrm{Tr}\underline{\underline{u}}^3 + c_7 \mathrm{Tr}\underline{\underline{u}}^2(\mathrm{Tr}\underline{\underline{u}})^2 + c_8(\mathrm{Tr}\underline{\underline{u}}^2)^2, \quad (4.1) \end{aligned}$$

where μ and λ are the usual Lamé coefficients, the c_i are presently arbitrary coefficients, and linear terms which must vanish for a body in equilibrium have been neglected. Further restricting our attention to three dimensional systems, the above simplifies because there are only three unique rotational invariants, which may be taken to be $\mathrm{Tr}\underline{\underline{u}}, \mathrm{Tr}\underline{\underline{u}}^2$, and $\mathrm{Tr}\underline{\underline{u}}^3$. The term $\mathrm{Tr}\underline{\underline{u}}^4$ can thus be neglected since it can be written as a linear combination of the other invariants.

To gain insight into the effect of each nonlinear term consider the response of the system to a pure shear strain $u_{xy} = u_{yx} = \frac{\gamma}{2}$. The stress from this deformation can be calculated from $\sigma_{ik} = \frac{\delta F}{\delta u_{ik}}$. Since pure shear is volume preserving ($\mathrm{Tr}\underline{\underline{u}} = 0$) any term that is quadratic or higher in $\mathrm{Tr}\underline{\underline{u}}$ will not contribute any stresses and thus we may neglect c_2, c_5, and c_7. The remaining non zero contributions to the

stress are

$$\begin{aligned}
\mu &: \sigma_{xy} = \sigma_{yx} = \mu\gamma, \\
c_1 &: \sigma_{xx} = \sigma_{yy} = c_1\frac{3\gamma^2}{4}, \\
c_3 &: \sigma_{xx} = \sigma_{yy} = \sigma_{zz} = c_3\frac{\gamma^2}{2}, \\
c_6 &: \underline{\underline{\sigma}} = 0, \\
c_8 &: \sigma_{xy} = \sigma_{yx} = c_8\gamma^3.
\end{aligned} \tag{4.2}$$

Evidently c_1 and c_3 contribute to the normal stresses and c_8 contributes to strain stiffening. If the free energy is meant to model a biopolymer gel we must impose conditions on the coefficients to guarantee both negative normal stresses and strain stiffening under shear. This gives the constraints $c_8 \geq 0, c_3 \leq 0$, and $c_1 \leq -\frac{2}{3}c_3$. Including these constraints gives the minimally nonlinear model free energy for a large-scale biopolymer network

$$F[\underline{\underline{u}}] = \int \mathrm{d}^d\mathbf{x}\frac{\lambda}{2}(\mathrm{Tr}\underline{\underline{u}})^2 + \mu\mathrm{Tr}\underline{\underline{u}}^2 - A\mathrm{Tr}\underline{\underline{u}}\mathrm{Tr}\underline{\underline{u}}^2 - B\mathrm{Tr}\underline{\underline{u}}^3 + C(\mathrm{Tr}\underline{\underline{u}}^2)^2, \tag{4.3}$$

where $A \geq 0, C \geq 0$, and $B \geq -\frac{2}{3}A$. This free energy will be the inspiration for the dynamical renormalization group study performed later in the chapter.

4.1.2 Motors

Biopolymer networks are actively driven by motor proteins, which accomplish force generation by consuming ATP. The most prevalent motor proteins in the cell are kinesin and myosin, which act on microtubules and F-Actin, respectively [AJL02]. A single myosin motor is not processive, i.e. it will act instantaneously and then fall off the filament and back into solution. Myosin can multimerize, however, into thick filaments which act processively. These motors can cause large network rearrangements including the formation of stress fibers. A graphical depiction of a myosin thick filament and it's resulting influence on a cross-linked F-Actin network is shown in Fig. 4.2.

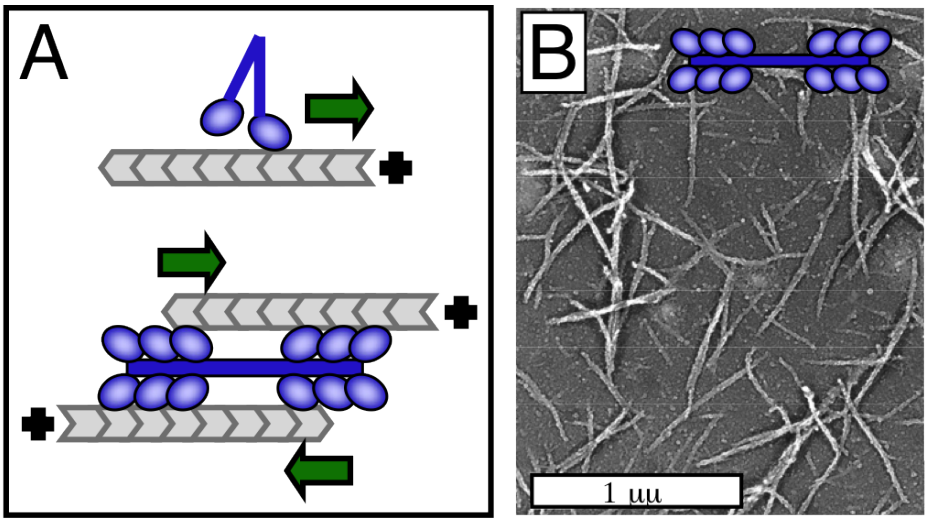

Figure 4.2: Left: a single myosin is not processive, but can multimerize into processive thick filaments. Right: The formation of stress fibers is evident in the presence of motors. From Koenderink 2009 [KDN09]

Here I briefly describe the physical model of the motors and derive the statistical properties of the noise the motors introduce to the polymer networks. I assume the motors generate a constant force $\vec{f_0}$ while they are acting on the network. This represents motors which are held fixed at one end (an experimentally realizable system), for example to a glass coverslip. If the motors were in the bulk they would act as force dipoles and there would be no net injection of momentum into the network. The dissociation of the motors is assumed to follow a poisson process where the probability of a motor acting for duration T is

$$P(T) = \frac{1}{\tau} e^{-\frac{T}{\tau}}, \tag{4.4}$$

where τ is the characteristic on time of the motors, a few seconds for most myosin thick filaments. This describes an Ornstein–Uhlenbeck process with correlation function

$$\langle f_i(\mathbf{x}, t) f_j(\mathbf{x}', t') \rangle = \frac{f_0^2}{\tau} e^{-\frac{t-t'}{\tau}} \delta_{i,j} \delta(\mathbf{x} - \mathbf{x}'). \tag{4.5}$$

The noise is assumed isotropic with vanishing first moment. As stated by the Wiener-Khinchin theorem, the power spectral density is the Fourier transform of the real space two point function [Kit58]

$$2D(\mathbf{k},\omega) = \langle f_i(\mathbf{k},\omega) f_j(\mathbf{k}',\omega')\rangle = \frac{2f_0^2}{1+\omega^2\tau^2}\delta_{i,j}\delta(\mathbf{k}+\mathbf{k}')\delta(\omega+\omega'). \tag{4.6}$$

In the limit $\tau \to 0$ the motors are uncorrelated and the standard white noise limit is recovered. As $\tau \to \infty$ the noise amplitude vanishes continuously, except for very small frequencies, in such a way that the total noise $D(\mathbf{k},0)$ remains fixed. It is interesting to consider more dramatic forms of external driving, for example the forcing function given by

$$2D(\mathbf{k},\omega) = \langle f_i(\mathbf{k},\omega) f_j(\mathbf{k}',\omega')\rangle = \frac{2f_0^2}{\omega^2 \ + \frac{1}{\tau^2}}\delta_{i,j}\delta(\mathbf{k}+\mathbf{k}')\delta(\omega+\omega') \tag{4.7}$$

has a diverging zero frequency component as $\tau \to \infty$. This will presumably drive the system very far from equilibrium, with unknown consequences. This noise form may model a system where motors are constantly created and added to the system, so that $D(\mathbf{k},0)$ is not fixed.

I note that it is a simple manner to treat motors acting in the bulk, i.e. one which act as force dipoles: The spectral densities given above need only be multiplied by k^2.

4.1.3 Dynamics and critical behavior

The dynamics resulting from active motor forcing should reflect the fact that natural biopolymer networks exist in highly over damped environments. The correct dynamical description of the displacement field $\mathbf{u}$ is therefore Model A [HH77]:

$$\frac{1}{\Gamma}\partial_t u_i = -\frac{\delta F}{\delta u_i} + f_i = \nabla_i \cdot \frac{\delta F}{\delta \underline{\underline{u}}} + f_i, \tag{4.8}$$

where Γ is a drag coefficient which is henceforth set to unity, $\mathbf{f}$ is the random forcing, and the free energy F is given by Eq. 4.3. Neglecting the nonlinearities

for the moment, and assuming an incompressible gel, one finds the dynamical equation

$$\partial_t u_i = \mu \nabla^2 u_i - \nabla_i P + f_i, \tag{4.9}$$

where μ is the shear modulus, and the pressure P enforces incompressibility. Naturally the equation is easier to treat in Fourier space, where the differential operators are diagonal:

$$-i\omega u_i = \mu k^2 u_i - i k_i P + f_i. \tag{4.10}$$

The pressure is eliminated by enforcing $\mathbf{k} \cdot \mathbf{u} = 0$, which effectively removes the longitudinal component of the displacement field from the theory. The resulting dynamics for the transverse component are

$$u_i(\mathbf{k}, \omega) = \frac{1}{-i\omega + \mu k^2} P_{ij}(\mathbf{k}) f_j(\mathbf{k}, \omega), \tag{4.11}$$

where $\underline{\underline{P}}$ is the transverse projection operator. To continue we must specify the form of the random forcing $f(\mathbf{k}, \omega)$. We assume it is Gaussian distributed so that we only need to specify the first two moments

$$\begin{aligned} \langle f_i(\mathbf{k}, \omega) \rangle &= 0 \\ \langle f_i(\mathbf{k}, \omega) f_j(\mathbf{k'}, \omega') \rangle &= 2D(\mathbf{k}, \omega) \delta^d(\mathbf{k} + \mathbf{k'}) \delta(\omega + \omega') \delta_{ij}, \end{aligned} \tag{4.12}$$

where $D(\mathbf{k}, \omega)$ is the forcing function or power spectral density. We may now examine the typical strains present in the network due to the random forcing. The linearized strain tensor is given by

$$e_{ij} = \frac{1}{2}(\partial_i u_j + \partial_j u_i). \tag{4.13}$$

The average strain $\langle \underline{\underline{e}} \rangle = 0$ since the noise is assumed isotropic, but the second moments will in general not vanish. The fluctuations of each element of the strain tensor are of the same order (off diagonal elements are half as big as diagonal elements), so without loss of generality we look at the xx component $e_{xx} = \partial_x u_x$.

Fourier transforming and using our solution for **u** Eq. 4.11 gives an explicit expression for the strain in terms of the noise:

$$e_{xx}(\mathbf{k},\omega) = \frac{ik_x P_{xj} f_j(\mathbf{k},\omega)}{-i\omega + \mu k^2}. \tag{4.14}$$

The interesting quantity is $\langle e_{xx}(\mathbf{k},\omega) e_{xx}(\text{-}\mathbf{k},-\omega)\rangle$ which we denote as $e^2(\mathbf{k},\omega)$. We have that

$$\begin{aligned} e^2(\mathbf{k},\omega) &= \left\langle \frac{ik_x P_{xj} f_j(\mathbf{k},\omega)}{-i\omega+\mu k^2} \frac{-ik_x P_{xk} f_k(\mathbf{k},\omega)}{i\omega+\mu k^2} \right\rangle \\ &= \frac{k_x k_k P_{xj} P_{xk} \langle f_k f_j\rangle}{\omega^2 + \mu^2 k^4} \\ &= \frac{k_x k_k P_{xj} P_{xj} 2D(\mathbf{k},\omega)}{\omega^2+\mu^2 k^4}. \end{aligned} \tag{4.15}$$

A quick calculation shows that $P_{xj}P_{xj} = 1 - \hat{k_x}^2$. What we're really interested in is the equal time equal space correlations, i.e. in the Fourier transform of e^2 with $x = t = 0$. Explicity:

$$e^2(\mathbf{x}=0,t=0) = \int \frac{\mathrm{d}^d\mathbf{k}}{(2\pi)^d}\frac{\mathrm{d}\omega}{2\pi}\frac{2D(\mathbf{k},\omega)k_x k_x(1-\hat{k_x}^2)}{(\omega+i\mu k^2)(\omega - i\mu k^2)}. \tag{4.16}$$

It is convenient to evaluate the integral in d dimensional spherical polar coordinates. The angular integral gives a dimension dependent prefactor A_d. The remaining radial and frequency integrals are

$$e^2(\mathbf{x}=0,t=0) = A_d \int \mathrm{d}k\, k^{d-1} k^2 \int \frac{d\omega}{\pi} \frac{D(k,\omega)}{(\omega+i\mu k^2)(\omega - i\mu k^2)}. \tag{4.17}$$

At this point the exact form of $D(k,\omega)$ must be specified. First assume the motors follow an Ornstein-Uhlenbeck process, so that D is given by Eq. 4.6:

$$D(\mathbf{k},\omega) = \frac{2D_0}{1+\frac{\omega^2}{s^2}} \tag{4.18}$$

where I have introduced $s = \frac{1}{\tau}$. This gives squared strain fluctuations

$$e^2(\mathbf{x}=0,t=0) = A_d \int \mathrm{d}k\, k^{d-1} k^2 \int \frac{d\omega}{\pi} \frac{D_0}{(\omega+i\mu k^2)(\omega - i\mu k^2)(1+\frac{\omega^2}{s^2})}. \tag{4.19}$$

The frequency integral may be performed by contour integration. The result is

$$e^2(\mathbf{x}=0,t=0) = A_d \frac{D_0}{\mu} \int \mathrm{d}k\, k^{d-1} \frac{1}{1+\frac{\mu k^2}{s}}. \tag{4.20}$$

The radial integral may be evaluated but that is not necessary to capture the general behavior. We see that for finite s the integral is infrared divergent only for $d \leq 0$, and thus there will not be large fluctuation corrections to the strain in physical networks due to this noise. As $s \to 0$, however, the integral becomes formally divergent in two or less dimensions, suggesting that the noise is important for the physically realizable $d \leq 2$. This limit is somewhat subtle and will be examined in greater detail in subsequent sections.

Now consider the case of the divergent noise given by Eq. 4.7

$$D(k,\omega) = \frac{D_0}{\omega^2 + s^2}. \tag{4.21}$$

This gives squared strain fluctuations

$$e^2(\mathbf{x}=0,t=0) = A_d \int \mathrm{d}k\, k^{d-1} k^2 \int \frac{d\omega}{\pi} \frac{D_0}{(\omega + i\mu k^2)(\omega - i\mu k^2)(\omega^2 + s^2)}. \tag{4.22}$$

The frequency integral again may be performed by contour integration with result

$$e^2(\mathbf{x}=0,t=0) = A_d \frac{D_0}{s\mu^2} \int \mathrm{d}k\, k^{d-1} k^{-2} \frac{1}{1+\frac{s}{\mu k^2}}. \tag{4.23}$$

We see that in the $s \to 0$ limit the strains will diverge in *any* dimension! For small but finite s the integral is infrared divergent in $d \leq 2$ dimensions.

4.1.4 A model system: ϕ^4 with colored noise

To make further progress we must include the nonlinearities in the free energy Eq. 4.3. Assuming the nonlinearities are small, the resulting dynamical equations can be studied with the tools of perturbative renormalization group. Unfortunately, the elastic system is extremely complicated even for vanilla white noise, due in part to both the tensorial nature of the strain field and the requirement of incompressibility. Since the goal is to understand the role the active noise plays, I will

consider instead a scalar elastic model, i.e. a ϕ^4 theory in the presence of active colored forcing. The effect of the noise may now be isolated, since, unlike in the tensorial elastic model, the white noise limit is well understood.

In the usual way, consider a scalar field $\phi(x,t)$ with the general quartic Landau-Ginzburg nonlinear free energy (cubic term excluded by e.g. symmetry):

$$\mathcal{F}[\phi] = \frac{1}{2}\int \mathrm{d}^d x\, r\phi^2 + \mu|\nabla\phi|^2 + \frac{1}{2}g\phi^4, \tag{4.24}$$

where r is assumed positive. Imagine that this field is driven by an active noise source η which has first and second moments

$$\begin{aligned} \langle\eta\rangle &= 0 \\ \langle\eta(x,t)\eta(x',t')\rangle &= 2D(x,t)\delta(x-x')\delta(t-t'). \end{aligned} \tag{4.25}$$

If we assume that ϕ is a non conserved field then it will satisfy the dynamical equation

$$\partial_t\phi = -r\phi + \mu\nabla^2\phi - g\phi^3 + \eta. \tag{4.26}$$

The linear differential operators are diagonalized in Fourier space so we switch and never look back. Dropping the tildes on $\phi(x,t) \to \tilde{\phi}(k,\omega)$:

$$-i\omega\phi = -r\phi - \mu k^2\phi - g\int_{p,q,\nu,\Omega} \phi(k-q)\phi(q-p)\phi(p) + \eta, \tag{4.27}$$

where the arguments of ϕ have been suppressed for convenience. The linear behavior is determined entirely by the propagator or linear response function

$$G_0(k,\omega) = \frac{1}{-i\omega + \mu k^2 + r}, \tag{4.28}$$

in terms of which the equation of motion reads

$$\phi = G_0\eta - gG_0\int_{p,q,\nu,\Omega} \phi(k-q)\phi(q-p)\phi(p). \tag{4.29}$$

In the linear theory (g=0) correlation functions are determined by $G_0(k,\omega)$ and $D(k,\omega)$. Explicitly we have that $\langle\phi\rangle \propto \langle\eta\rangle = 0$ and

$$\frac{\langle\phi(k,\omega)\phi(k',\omega')\rangle}{\delta(k+k')\delta(\omega+\omega')} = \frac{2D(k,\omega)}{\omega^2 + (\mu k^2 + r)^2}. \tag{4.30}$$

All higher order odd correlation functions vanish and even ones may be calculated from the two point function with Wick's theorem since the theory is Gaussian. I will study two different forms of the forcing function $D(k,\omega)$, which were discussed in Sec. 4.1.2. The finite noise is given by

$$D_f(k,\omega) = \frac{D_f}{1+\frac{\omega^2}{s^2}}, \tag{4.31}$$

while the singular noise has

$$D_s(k,\omega) = \frac{D_s}{\omega^2+s^2}. \tag{4.32}$$

I am primarily interested in understanding the large scale, long time (hydrodynamic) characteristics of the system. In this limit of the theory may be studied with the tools of Renormalization Group Theory, which involves a systematic scaling out to larger distances and timescales. The relevance of model parameters is determined primarily by their naıve scaling dimension, but if this vanishes, i.e. if the gaussian theory exhibits scale invariance, then non linear corrections will determine the behavior of the model. Under a simple scale transformation $x = bx', t = b^z t', \phi = b^\chi \phi'$, with $b = 1 + \delta l$ the infinitesimal transformation parameter, the equations of motion may be made invariant provided the model parameters satisfy

$$\begin{aligned}
\frac{\mathrm{d}r}{\mathrm{d}l} &= zr \\
\frac{\mathrm{d}\mu}{\mathrm{d}l} &= (z-2)\mu \\
\frac{\mathrm{d}g}{\mathrm{d}l} &= (2\chi+z)g \\
\frac{\mathrm{d}s}{\mathrm{d}l} &= zs \\
\frac{\mathrm{d}D_s}{\mathrm{d}l} &= (3z-d-2\chi)D_s \\
\frac{\mathrm{d}D_f}{\mathrm{d}l} &= (z-d-2\chi)D_f.
\end{aligned} \tag{4.33}$$

The exponents z and χ may be chosen to simply the flow equations. Let the dynamical exponent $z = 2$ and the roughness exponent $\chi = \frac{2-d}{2}, \frac{6-d}{2}$, for the

conservative and non-conservative cases, respectively, so that μ and the noise strength do not renormalize. It is clear that the parameters r and s always grow under rescaling and are considered relevant. The nonlinear coupling g is found to be marginal in $d_f = 4, d_s = 8$ dimensions for the two types of noise.

What effect does the nonlinearity have on this analysis? I can answer this question so long as the nonlinear coupling g is small (more precisely we will need a small *effective coupling*), so that I may proceed perturbatively. The basic idea, following [HH77], is to integrate out the large k and ω modes from the system, absorbing the perturbative corrections into redefinitions of the bare model parameters, r, μ, s, and D. The divergences in the integrals are tamed by integrating only over an infinitesimal shell. The solution is organized into a propagator, spectral density, and vertex correction, as shown in figure 4.3. I now examine the two different forcing functions presented in 4.1.2 separately.

4.1.5 Finite colored noise

4.1.5.1 Propagator Renormalization

The lowest order correction to the propagator (diagram (a) in Fig. 4.3) is

$$\delta G_1 = -6G_0^2(k,\omega)g \int_{q,\Omega} \frac{D_f}{1+\frac{\Omega^2}{s^2}} \frac{1}{\Omega^2 + (\mu q^2 + r)^2}, \tag{4.34}$$

where I have included the symmetry factor 3 and the integral over q, Ω contains a factor $1/(2\pi)^{d+1}$. The integral is to be evaluated over an infinitesimal shell containing the large k, ω modes. Conventionally, this is taken to be a momentum shell, and the frequency integral is performed in its entirety. However, there is nothing wrong in principle with choosing the opposite scheme: Integrate over all wave vectors and over an infinitesimal frequency shell– See Fig. 4.4. The reason for breaking with tradition has to do with power law nature of the noise as $s \to 0$, making the frequency integral badly divergent. Unlike momentum shell integration, The frequency shell method avoids the line $\omega = 0$ and thus is a well

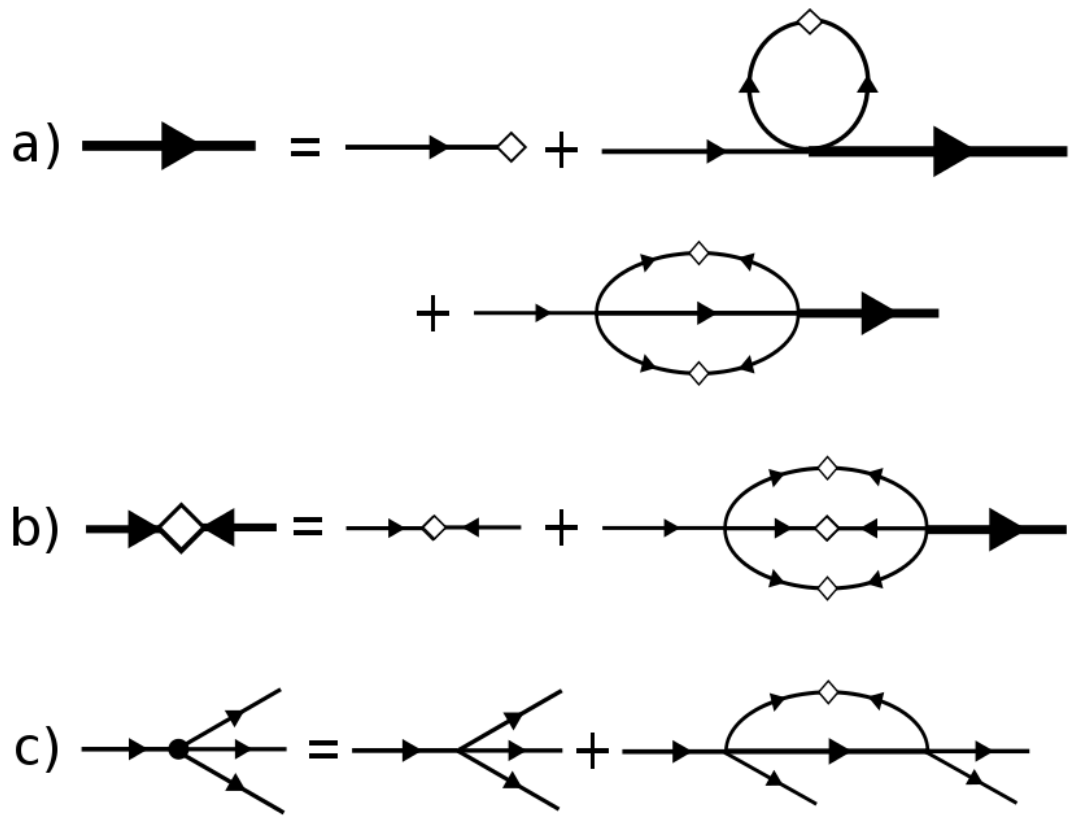

Figure 4.3: Feynman diagrams contributing to the renormalization of the model parameters. a) Response function renormalization. The $\mathcal{O}(g)$ diagram renormalizes the relaxation rate r, while the $\mathcal{O}(g^2)$ gives corrections to both r and μ. b) The spectral density renormalization gives corrections to $D(k,\omega)$. c) Lowest order diagram contributing to vertex renormalization.

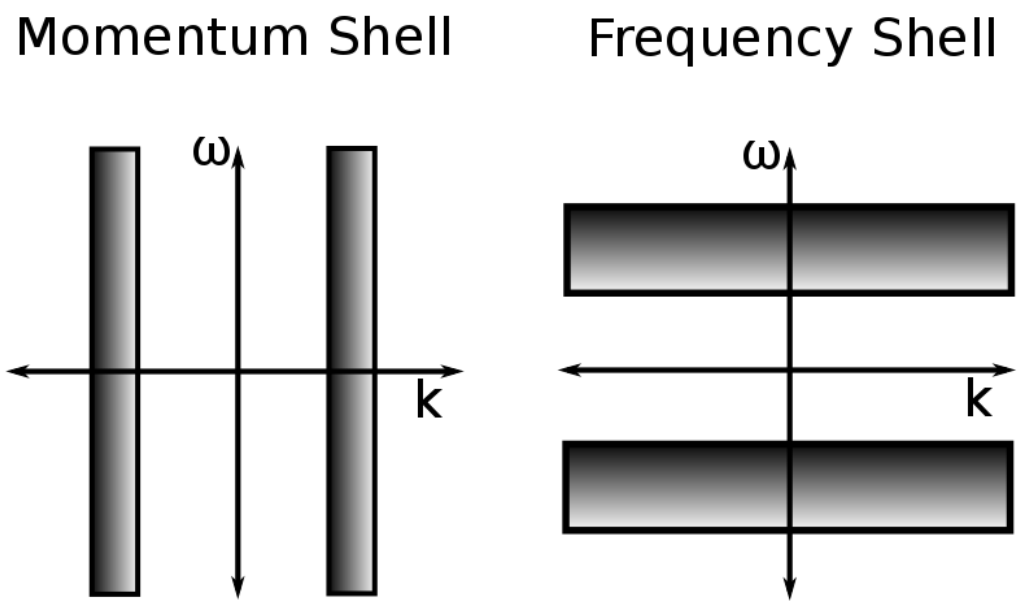

Figure 4.4: Two different shell integration schemes.

defined procedure.

Taking the shell to be at $\Lambda_\omega = 1$ with width $z\delta l$ I find the following correction in the limit $r \to 0$.

$$\delta G_1 = -G_0^2(k,\omega)\frac{3zD_f g K_d}{2\mu}\frac{1}{1+\frac{1}{s^2}}\csc\left(\frac{\pi d}{4}\right)\delta l, \tag{4.35}$$

where $K_d = \frac{S_{d-1}}{(2\pi)^d}$, with S_{d-1} as the surface area of a d dimensional sphere. There is an ultraviolet divergence in $d = 4$ due to extending the momentum integral over all space. This could be removed by considering a frequency-momentum shell scheme, but since the physical dimensions of interest are $d \leq 3$ it is not problematic. This correction is independent of k and will only renormalize r. To find the lowest order correction to μ the expansion must be taken to two loop order. I find the second order correction

$$\delta G_2 = G_0^2(k,\omega)\frac{zD_f^2 g^2}{\mu^3}\left(\frac{1}{1+\frac{1}{s^2}}\right)^2\left(C_0(d) - C_1(d)k^2 + \mathcal{O}(k^4)\right)\delta l, \tag{4.36}$$

where C_0 and C_1 are dimension dependent constants. In the relevant case of $d = 3$ I find $C_0 = 9.5 \times 10^{-4}, C_1 = 7.5 \times 10^{-5}$. Collectively, the corrections imply the following corrections to the RG flow equations for r and μ:

$$\begin{aligned} \frac{\mathrm{d}r}{\mathrm{d}l} &= zr + \frac{3zD_f g K_d}{2\mu} \frac{1}{1+\frac{1}{s^2}} \csc\left(\frac{\pi d}{4}\right) - \frac{zD_c^2 g^2}{\mu^3} \left(\frac{1}{1+\frac{1}{s^2}}\right)^2 C_0(d) \\ \frac{\mathrm{d}\mu}{\mathrm{d}l} &= (z-2)\mu + \frac{zD_f^2 g^2}{\mu^4} \left(\frac{1}{1+\frac{1}{s^2}}\right)^2 C_1(d). \end{aligned} \tag{4.37}$$

4.1.5.2 Spectral Density Renormalization

The lowest order correction to the spectral density is order $\mathcal{O}(g^2)$ and comes from the diagram shown in Fig. 4.3(b). Again performing frequency shell integration at $\Lambda_\omega = 1$ with $r \to 0$ I find

$$\delta D_f = \frac{g^2 D_f^3 z C_2(d)}{\mu^4} \left(\frac{1}{1+\frac{1}{s^2}}\right)^3 \delta l, \tag{4.38}$$

where $C_2(d)$ is another dimensional dependent constant, with $C_2(d=3) = 1.09 \times 10^{-4}$. Absorbing this into a redefinition of the conserved noise strength D_c gives the following perturbative correction to the D_c flow equation:

$$\frac{\mathrm{d}D_f}{\mathrm{d}l} = (z - d - 2\chi)D_f + \frac{g^2 D_f^2 z C_2(d)}{\mu^4} \left(\frac{1}{1+\frac{1}{s^2}}\right)^2. \tag{4.39}$$

The motor correlation time $1/s$ is also renormalized by this diagram, but it will not modify the exponents so I neglect it.

4.1.5.3 Vertex Renormalization

The bare vertex(four point function) in the theory is

$$\Gamma = -g G_0^2(k,\omega) |G_0(k_2,\omega_2)|^2, \tag{4.40}$$

to which the nonlinear term generates the frequency shell correction in the hydrodynamic limit

$$\delta\Gamma = G_0^2(k,\omega) |G_0(k_2,\omega_2)|^2 \frac{9 D_f g^2 K_d z}{4\mu^2} \left(\frac{1}{1+\frac{1}{s^2}}\right) (2-d) \sec\left(\frac{\pi d}{4}\right) \delta l, \tag{4.41}$$

where once again the secant highlights the UV divergence in $d \geq 4$. This may be absorbed into a redefinition of g:

$$\frac{\mathrm{d}g}{\mathrm{d}l} = (2\chi + z)g - \frac{9D_f g^2 K_d z}{4\mu^2}\left(\frac{1}{1+\frac{1}{s^2}}\right)(2-d)\sec\left(\frac{\pi d}{4}\right). \tag{4.42}$$

4.1.5.4 RG flow equations

I now summarize the results of the calculations. The full set of flow equations for the finite colored noise is, to leading order,

$$\begin{aligned}
\frac{\mathrm{d}r}{\mathrm{d}l} &= zr + \frac{3zD_f g K_d}{2\mu}\frac{1}{1+\frac{1}{s^2}}\csc\left(\frac{\pi d}{4}\right) \\
\frac{\mathrm{d}\mu}{\mathrm{d}l} &= \left(z - 2 + \frac{zD_f^2 g^2}{\mu^4}\left(\frac{1}{1+\frac{1}{s^2}}\right)^2 C_1(d)\right)\mu \\
\frac{\mathrm{d}s}{\mathrm{d}l} &= zs \\
\frac{\mathrm{d}D_f}{\mathrm{d}l} &= \left(z - d - 2\chi + \frac{g^2 D_f^2 z C_2(d)}{\mu^4}\left(\frac{1}{1+\frac{1}{s^2}}\right)^2\right)D_f \\
\frac{\mathrm{d}g}{\mathrm{d}l} &= (2\chi + z)g - \frac{9D_f g^2 K_d z}{4\mu^2}\left(\frac{1}{1+\frac{1}{s^2}}\right)(2-d)\sec\left(\frac{\pi d}{4}\right),
\end{aligned} \tag{4.43}$$

where I have neglected the $\mathcal{O}(g^2)$ term in the renormalization of r since there is an $\mathcal{O}(g)$ correction. The most striking effect of the noise is on the location of the fixed points. We see that $g^* \sim 1/s^2$ for $s << 1$. If $s(l=0) \equiv s_0$ is sufficiently small, the system will always be strongly nonlinear.

The parameters z and χ are presently free, and we may let them take specific values to simplify the equations. The most common choice enforces that μ and D_f do not renormalize. Introducing $\bar{r} = r/\mu$ and $\bar{g} = D_f g/\mu^2$, I find the exponents

$$\begin{aligned}
z &= 2 - 2\bar{g}^2\left(\frac{1}{1+\frac{1}{s^2}}\right)^2 C_1(d) \\
\chi &= \frac{1}{2}\left[2 - d + 2\bar{g}^2\left(\frac{1}{1+\frac{1}{s^2}}\right)^2 (C_2(d) - C_1(d))\right].
\end{aligned} \tag{4.44}$$

The flow equations for the remaining parameters are

$$\begin{aligned}
\frac{\mathrm{d}\bar{r}}{\mathrm{d}l} &= \left(2 - 2\bar{g}^2 \left(\frac{1}{1+\frac{1}{s^2}}\right)^2 C_1(d)\right)\bar{r} + 3\bar{g}K_d \frac{1}{1+\frac{1}{s^2}} \csc\left(\frac{\pi d}{4}\right) \\
\frac{\mathrm{d}s}{\mathrm{d}l} &= 2s \\
\frac{\mathrm{d}\bar{g}}{\mathrm{d}l} &= (4-d)\bar{g} - \frac{9\bar{g}^2 K_d}{2}\left(\frac{1}{1+\frac{1}{s^2}}\right)(2-d)\sec\left(\frac{\pi d}{4}\right), \qquad (4.45)
\end{aligned}$$

where I have let $z = 2$ where appropriate and neglected terms of order $\bar{g}^3$. The fixed points of this system of equations are trivial. Since s grows under rescaling it must be that $\bar{s} = 0$. In this limit the nonlinear corrections vanish, and we therefore conclude that $\bar{r} = 0$ and $\bar{g} = 0$ as well.

4.1.5.5 Correlation functions

The RG scale transformation enables one to write correlation functions at two different scales. Recalling the scaling behavior of the field ϕ I find the homogeneity relation

$$\begin{aligned}
G(k,\omega;r_0,g_0) &= \frac{\langle\phi(k,\omega)\phi(k',\omega')\rangle}{(2\pi)^{d+1}\delta^d(k+k')\delta(\omega+\omega')} \\
&= e^{2(\beta(l)+dl+\alpha(l))-dl-\alpha(l)} \frac{\langle\phi(e^l k, e^{\alpha(l)}\omega)\phi(e^l k', e^{\alpha(l)}\omega')\rangle}{(2\pi)^{d+1}\delta^d(e^l k + e^l k')\delta(e^{\alpha(l)}\omega + e^{\alpha(l)}\omega')} \\
&= e^{2\beta(l)+dl+\alpha(l)} G(e^l k, e^{\alpha(l)}\omega; \bar{r}(l), \bar{g}(l)), \qquad (4.46)
\end{aligned}$$

where

$$\begin{aligned}
\alpha(l) &= \int^l \mathrm{d}l'\, z(l') \\
\beta(l) &= \int^l \mathrm{d}l'\, \chi(l') \qquad (4.47)
\end{aligned}$$

The prefactor $e^{2(\beta(l)+dl+\alpha(l))}$ follows from the scaling of ϕ in Fourier space; $e^{-dl-\alpha(l)}$ accounts for the scaling dimension of the Dirac delta functions.

Consider the case $r = 0$ where the correlation function is expected to take the form

$$G(k,\omega) = \frac{2D_f^R(k,\omega)}{\omega^2 + \mu_R(k,\omega)^2 k^4} \frac{1}{1+\frac{\omega^2}{s^2}}, \qquad (4.48)$$

with $\mu_R(k,\omega)$, $D_f^R(k,\omega)$ the wave vector and frequency dependent renormalized diffusion coefficient and noise strength, respectively. Scaling relations for the renormalized parameters follow from Eq. 4.46, namely

$$\begin{aligned} \mu_R(k,\omega;\bar{g}_0) &= e^{2l-\alpha(l)}\mu_R\left(e^l k, e^{\alpha(l)}\omega;\bar{g}(l)\right) \\ D_f^R(k,\omega;\bar{g}_0) &= e^{2\beta(l)+dl-\alpha(l)}D_f^R\left(e^l k, e^{\alpha(l)}\omega;\bar{g}(l)\right). \end{aligned} \tag{4.49}$$

Consider now the diffusion coefficient for $k = 0$ in $\epsilon = 4 - d$ dimensions. Evaluate the right hand side at $l = l^*$ such that $e^{\alpha(l^*)}\omega = 1 \to l^* \approx \frac{1}{2}\log 1/\omega$ and expand for small coupling (valid because $\bar{g}$ flows to an order ϵ fixed point).

$$\mu_R(0,\omega) = e^{2l^*-\alpha(l^*)}\mu_R\left(0,1;\bar{g}(l^*)\right) \approx \mu_R(1+\int^{l^*} \mathrm{d}l'\ [2-z(l')]+\cdots), \tag{4.50}$$

where

$$\int^{l^*} \mathrm{d}l'\ [2-z(l')] = 2C_1(d)\int^{l^*} \mathrm{d}l'\,\bar{g}^2(l')\left(\frac{1}{1+\frac{1}{s(l')^2}}\right)^2 \tag{4.51}$$

is order $\bar{g}^2$. The resulting frequency dependent diffusion coefficient is shown for the physically relevant case of $\epsilon = 1$ ($d = 3$) in Fig. 4.5. The different curves represent different values of s_0, with $s(l) = s_0 e^{2l}$.

4.1.6 Singular colored noise–Frequency shell approach

The analysis is similar to the finite noise study of the previous section. In fact, because of the frequency shell scheme, the replacement

$$\frac{1}{1+\frac{1}{s^2}} \quad \to \quad \frac{1}{1+s^2}, \tag{4.52}$$

and the trivial change to the naïve scaling dimension of the noise amplitude, are the only material differences in the flow perturbative flow equations. It is worth noting that frequency shell methods are capable of handling arbitrarily complex temporally correlated forcing functions, whereas momentum shell would be useful for complicated spatially correlated noise. In the problem at hand, the resulting

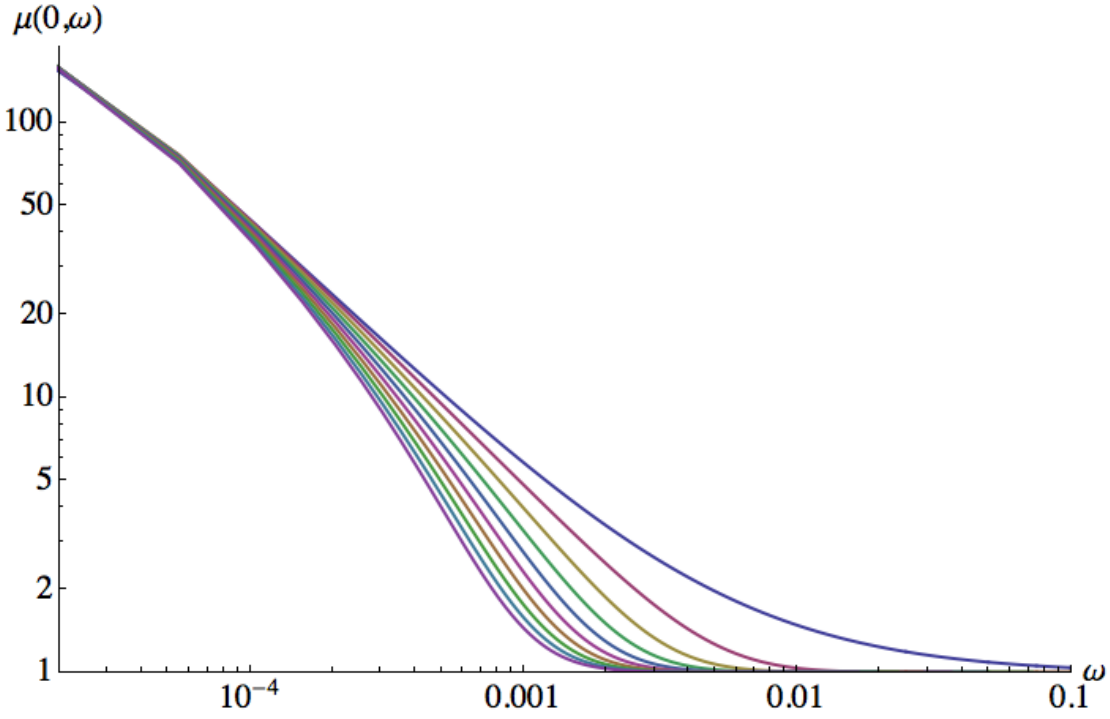

Figure 4.5: Renormalized diffusion coefficient μ at $k = 0$, $r = 0$ for finite noise. The noise does not renormalize μ at high frequency $\omega > s$, but produces a quick transient to the white noise enhanced mixing at low frequencies.

flow equations are

$$\begin{aligned}
\frac{\mathrm{d}r}{\mathrm{d}l} &= zr + \frac{3zD_s g K_d}{2\mu}\frac{1}{1+s^2}\csc\left(\frac{\pi d}{4}\right) \\
\frac{\mathrm{d}\mu}{\mathrm{d}l} &= \left(z - 2 + \frac{zD_s^2 g^2}{\mu^4}\left(\frac{1}{1+s^2}\right)^2 C_1(d)\right)\mu \\
\frac{\mathrm{d}s}{\mathrm{d}l} &= zs \\
\frac{\mathrm{d}D_s}{\mathrm{d}l} &= \left(3z - d - 2\chi + \frac{g^2 D_s^2 z C_2(d)}{\mu^4}\left(\frac{1}{1+s^2}\right)^2\right) D_s \\
\frac{\mathrm{d}g}{\mathrm{d}l} &= (2\chi + z)g - \frac{9D_s g^2 K_d z}{4\mu^2}\left(\frac{1}{1+s^2}\right)(2-d)\sec\left(\frac{\pi d}{4}\right),
\end{aligned} \tag{4.53}$$

where again I have neglected the $\mathcal{O}(g^2)$ term in the renormalization of r since there is an $\mathcal{O}(g)$ correction, and the C_i are identical to the finite noise versions. A reduced set of equations is produced by choosing z and χ such that μ and D_f

do not renormalize. Introducing $\bar{r} = r/\mu$ and $\bar{g} = D_s g/\mu^2$, I find the exponents

$$\begin{aligned} z &= 2 - 2\bar{g}^2 \left(\frac{1}{1+s^2}\right)^2 C_1(d) \\ \chi &= \frac{1}{2}\left[6 - d + 2\bar{g}^2 \left(\frac{1}{1+s^2}\right)^2 (C_2(d) - C_1(d))\right]. \end{aligned} \tag{4.54}$$

The flow equations for the remaining parameters are

$$\begin{aligned} \frac{\mathrm{d}\bar{r}}{\mathrm{d}l} &= \left(2 - 2\bar{g}^2 \left(\frac{1}{1+s^2}\right)^2 C_1(d)\right)\bar{r} + 3\bar{g}K_d \frac{1}{1+s^2} \csc\left(\frac{\pi d}{4}\right) \\ \frac{\mathrm{d}s}{\mathrm{d}l} &= 2s \\ \frac{\mathrm{d}\bar{g}}{\mathrm{d}l} &= (8-d)\bar{g} - \frac{9\bar{g}^2 K_d}{2}\left(\frac{1}{1+s^2}\right)(2-d)\sec\left(\frac{\pi d}{4}\right), \end{aligned} \tag{4.55}$$

where I have let $z = 2$ where appropriate and neglected terms of order $\bar{g}^3$. Following the analysis of Sec. 4.1.5.5 I find a renormalized diffusion coefficient in $d = 8 - \epsilon$ dimensions. The physically relevant case of $\epsilon = 5$ ($d = 3$) is shown in Fig. 4.6. I note in passing that the theory is perfectly well defined for $s \to 0$: it is simply a white noise theory in dimension $d = 8$.

The one loop fixed point structure is very simple. Since s always grows under rescaling, one must have $s = 0$. The flow equations then reduce to the white noise equations around $d = 8$ dimensions:

$$\begin{aligned} \bar{r}^* &= -\frac{\epsilon}{3(2-d)} \cot\frac{\pi d}{4} \\ \bar{g}^* &= \frac{2\epsilon \cos\frac{\pi d}{4}}{9K_d(2-d)}, \end{aligned} \tag{4.56}$$

where $\epsilon = 8 - d$. These equations are different than the momentum shell white noise versions [HH77], but the fixed points are not physically measurable quantities, and it is not expected that the two techniques would produce the same values. Carrying the analysis to two loop order (including corrections to s) would give additional fixed points.

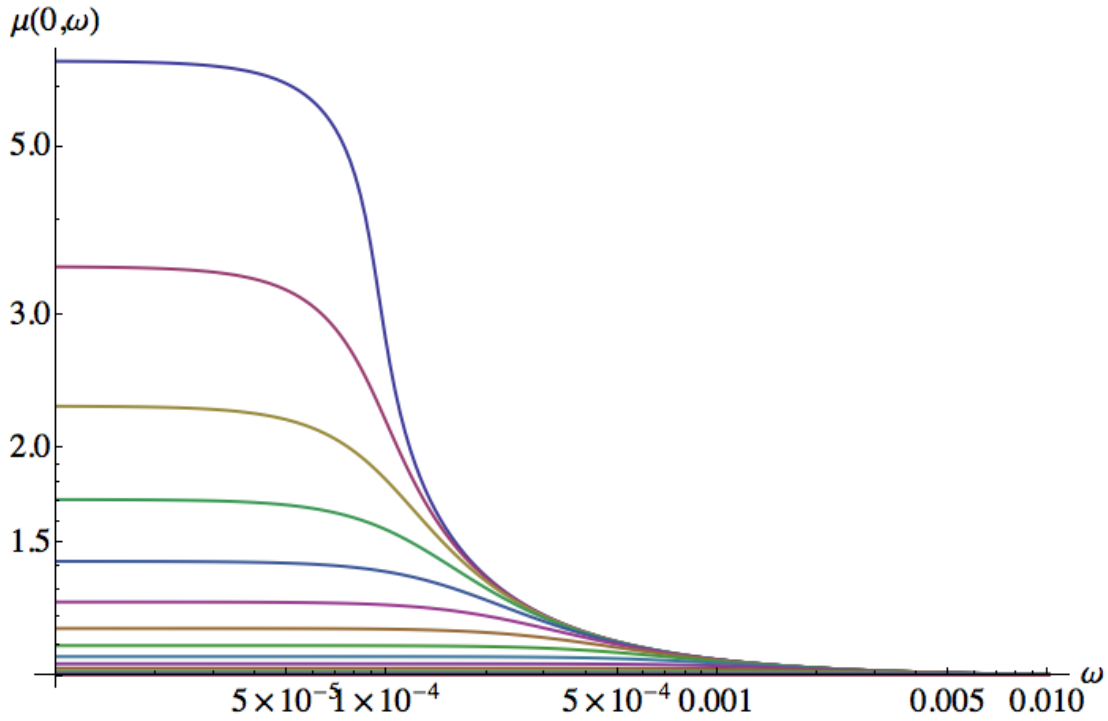

Figure 4.6: Renormalized diffusion coefficient μ at $k = 0, r = 0$ for singular noise. While the noise does not renormalize μ at high frequency $\omega > s$, there is a transient with diverging power law behavior near $\omega = s$. The diffusion coefficient remains constant for $\omega < s$ as $\omega \to 0$.

4.1.7 Comparison with momentum shell approach

I mentioned that it was necessary to employ a frequency shell integration scheme to consistently treat the colored noise for all values of s, especially for the singular noise which has a diverging $\omega = 0$ component as $s \to 0$. It is instructive to look at the difficulties one would encounter using the more traditional momentum shell scheme. I begin with an outline of the perturbative corrections, similar to the preceding sections. For simplicity I will only go to one loop order, so there will be no perturbative correction to the spectral density and no renormalization of the transport coefficients.

4.1.7.1 Propagator Renormalization

The lowest order correction to the propagator is

$$\delta G = 3G_0^2(k,\omega)(-g)\int_{q,\Omega} 2D(q,\Omega)|G_0(q,\Omega)|^2. \tag{4.57}$$

Using the singular noise forcing function Eq. 4.32 we have explicitly

$$\delta G = -6G_0^2(k,\omega)g\int_{q,\Omega}\frac{D_s}{\Omega^2+s^2}\frac{1}{\Omega^2+(\mu q^2+r)^2}. \tag{4.58}$$

In the $r \to 0$ limit, corresponding to the classical order/disorder transition, the correction diverges in $d = 2$ for finite s. If s is also allowed to vanish the correction will be formally infrared divergent in *any* dimension because of the integration across the $\Omega = 0$ singularity. Assuming finite s, I integrate over a shell of infinitesimal width at $|q| = \Lambda$. After setting $\Lambda = 1$ for convenience I find

$$\delta G = -\frac{3G_0^2 D_s g K_d}{s}\frac{1}{(r+\mu)(r+s+\mu)}, \tag{4.59}$$

where $K_d = \frac{S_{d-1}}{(2\pi)^d}$, with S_{d-1} as the surface area of a d dimensional sphere. The $1/s$ dependence is expected due to the divergent $s \to 0$ behavior. This correction may be absorbed into a redefinition of the model parameter r. There is no renormalization of the transport coefficient μ to one loop order because the correction is independent of external wave vector k.

4.1.7.2 Vertex Renormalization

The bare vertex(four point function) in the theory is

$$\Gamma = -gG_0^2(k,\omega)|G_0(k_2,\omega_2)|^2, \tag{4.60}$$

to which the nonlinear term generates the correction

$$\begin{aligned}\delta\Gamma &= 36(-g)^2 G_0^2(k,\omega)|G_0(k_2,\omega_2)|^2 \\ &\times \int_{q,\Omega}\frac{1}{\Omega^2+(\mu(k-q)^2+3)^2}\,\frac{1}{-i\Omega+\mu(q-k_2)^2+r}\,\frac{D_s}{\Omega^2+s^2}.\end{aligned} \tag{4.61}$$

The correction once again suffers from infrared divergences for sufficiently low dimension. If $r \to 0$ the divergence appears in $d = 4$, while if s is further allowed to vanish the integral will again diverge in arbitrary dimension. Following the same shell integration procedure for finite s with $\Lambda = 1$ one finds

$$\delta\Gamma = \frac{9D_s g^2 K_d}{s} \frac{s + 2(\mu + r)}{(\mu + r)^2 (s + r + \mu)^2}, \tag{4.62}$$

where again we see the characteristic $1/s$ divergence.

4.1.7.3 RG flow equations and analysis

The equations of motion may be made invariant to order g provided the model parameters satisfy

$$\begin{aligned}
\frac{\mathrm{d}r}{\mathrm{d}l} &= zr + \frac{3D_s g K_d}{s} \frac{1}{(r + \mu)(r + s + \mu)} \\
\frac{\mathrm{d}\mu}{\mathrm{d}l} &= (z - 2)\mu \\
\frac{\mathrm{d}g}{\mathrm{d}l} &= (2\chi + z)g - \frac{9D_s g^2 K_d}{s} \frac{s + 2(\mu + r)}{(\mu + r)^2 (s + r + \mu)^2} \\
\frac{\mathrm{d}s}{\mathrm{d}l} &= zs \\
\frac{\mathrm{d}D_s}{\mathrm{d}l} &= (3z - d - 2\chi)D_s.
\end{aligned} \tag{4.63}$$

We may choose the exponents z and χ to take the values 2 and $\frac{6-d}{2}$, respectively, so that μ and D_0 do not renormalize. The exponents are identical to the free theory exponents and thus there will be no new corrections to scaling behavior near the critical points $r, s = 0$. This is a consequence of μ not renormalizing to one loop order. If the calculation was carried out to higher order one could expect novel scaling behavior. At the present it is still interesting to examine the flows

of the remaining 3 parameters of the theory:

$$\begin{aligned}
\frac{\mathrm{d}r}{\mathrm{d}l} &= 2r + \frac{3D_0 g K_d}{s}\frac{1}{(r+\mu)(r+s+\mu)} \\
\frac{\mathrm{d}g}{\mathrm{d}l} &= (8-d)g - \frac{9D_0 g^2 K_d}{s}\frac{s+2(\mu+r)}{(\mu+r)^2(s+r+\mu)^2} \\
\frac{\mathrm{d}s}{\mathrm{d}l} &= 2s. \qquad (4.64)
\end{aligned}$$

The bare coupling g is relevant below $d = 8$, while r and s are always relevant, as expected. Again introducing the rescaled parameters $\bar{r} = r/\mu$, $\bar{g} = D_s g/\mu^2$, and $\bar{s} = s/\mu$, the flow equations are

$$\begin{aligned}
\frac{\mathrm{d}\bar{r}}{\mathrm{d}l} &= 2\bar{r} + \frac{1}{\bar{s}}\frac{3\bar{g}}{(1+\bar{r})(1+\bar{r}+\bar{s})} \\
\frac{\mathrm{d}\bar{s}}{\mathrm{d}l} &= 2\bar{s} \\
\frac{\mathrm{d}\bar{g}}{\mathrm{d}l} &= (8-d)\bar{g} - \frac{\bar{g}^2}{\bar{s}}\frac{9(2+2\bar{r}+\bar{s})}{(1+\bar{r})^2(1+\bar{r}+\bar{s})^2}. \qquad (4.65)
\end{aligned}$$

These equations are fundamentally different than the ones found through the frequency shell scheme, Eq. 4.55. While the frequency shell flows vary continuously as $s \to 0$, the momentum shell versions become undefined, encountering a $1/s$ singularity from the $\omega = 0$ component of the frequency integrals. These equations are clearly an incorrect description of the system near the $s = 0$ critical point, since, as shown with the frequency shell scheme, there is a well defined $s \to 0$ limit to the flow equations and the fixed points.

I note that it's possible to *tame* these equations by introducing a new noise amplitude $D_f \equiv D_s/s^2$, which represents the finite noise previously introduced. If one fixes D_f, the resulting flow equations will be well defined as $s \to 0$:

$$\begin{aligned}
\frac{\mathrm{d}\bar{r}}{\mathrm{d}l} &= 2\bar{r} + \frac{3g_w\bar{s}}{(1+\bar{r})(1+\bar{r}+\bar{s})} \\
\frac{\mathrm{d}\bar{s}}{\mathrm{d}l} &= 2\bar{s} \\
\frac{\mathrm{d}g_f}{\mathrm{d}l} &= (4-d)g_f - g_f^2\frac{9\bar{s}(2+2\bar{r}+\bar{s})}{(1+\bar{r})^2(1+\bar{r}+\bar{s})^2}, \qquad (4.66)
\end{aligned}$$

where $g_f = D_f g/\mu^2$. These equations successfully reduce to the vanilla white noise versions [HH77] in the limit $s \gg 1$ (or $\gg \mu\Lambda^2$ in standard units):

$$\begin{aligned} \frac{\mathrm{d}\bar{r}}{\mathrm{d}l} &= 2\bar{r} + \frac{3g_w}{1+\bar{r}} \\ \frac{\mathrm{d}\bar{s}}{\mathrm{d}l} &= 2\bar{s} \\ \frac{\mathrm{d}g_f}{\mathrm{d}l} &= (4-d)g_f - g_f^2 \frac{9\bar{r}}{(1+\bar{r})^2}. \end{aligned} \tag{4.67}$$

4.1.8 Conclusion

Biological motors which introduce temporal correlations into network fluctuations are expected to modify the transport coefficients of the system. Specifically, one should find a diffusion coefficient which is larger than expected, i.e. there will be enhanced mixing in the system. Cells may find this useful since transport by purely diffusive means can become prohibitive at typical cellular length scales. From a technical point of view, the normal momentum shell approach incorrectly predicts divergent behavior in the resulting flow equations, and the true scaling behavior is found with a *frequency* shell renormalization scheme which combats divergences in the forcing at $\omega = 0$. This rarely employed technique provides access to previously restricted dynamical systems.

4.2 Kinetic theory of soft networks

Amorphous solids exhibit anomalous mechanical response that depends sensitively on the contact network between individual constituents. A simple understanding of these phenomena was first proposed by Maxwell, who suggested studying the mechanical stability of solids by counting degrees of freedom relative to constraints imposed by network connectivity [Max64]. The balance of freedom and constraint may be encoded in the average coordination number z, and when the two are equal the system is *isostatic*. For networks whose coordination is above

a critical value, the mechanical response is predicted to behave elastically, while below this value the material exhibits fluid-like properties. These very general arguments have been applied in studying materials as diverse as biopolymer networks [LCB10, PHT14], hydrogels [WBJ12], emulsions [GCO08, GCB10, MCC11], granular media [OSL03], and foams [Dur95].

While static networks are well described using the coordination number as an order parameter for determining global stability, materials that are driven out of mechanical equilibrium cannot be described by connectivity alone. Biopolymer networks, for example, exhibit several regimes of mechanical response [HLM03, DML07, LCB10, PHT14]. On average, these networks are extremely underconstrained, and thus in the global sense Maxwell's argument predicts that they will deform and flow without resistance; contrary to this prediction, above a critical strain these networks exhibit nonlinear elasticity in the form of strain-stiffening, the onset of which is controlled by the coordination [HLM03, HVO07]. The anomalous response arising in the presence of external stress suggests that driving stimuli may used as additional dynamic order parameters in describing the transition between response regimes.

This behavior is reminiscent of jammed emulsions, which also exhibit a coordination controlled transition in the absence of load, and an anomalous dynamic mechanical response when subjected to applied stress. The correspondence between the two systems has been employed successfully in the static case [WSN05, SV10, LN10], and it is reasonable to expect that one could make inroads in the dynamic network stiffening problem by examining existing models of stress induced unjamming. Specifically, kinetic theories of elasto-plastic deformation have seen a great deal of success in predicting the behavior of jammed emulsions, and more generally materials whose macroscopic properties depend on a non-equilibrium microstructure [HL98, SLH97, Sol98, BCA09].

In this Letter, we show how a kinetic theory for strain propagation in an under-

coordinated network predicts the onset of strain induced rigidity, and highlight the correspondence to stress driven unjamming in emulsions. We postulate a series of simple mechanisms that describe how deformations occur within the network, from which a non-equilibrium Fokker-Planck equation describing the strain distribution arises naturally. Along with the formal correspondence between this kinetic theory and the mode-coupling theories describing jammed emulsions, our derivation recovers the strain-stiffening results present in sheared amorphous solids. We close by discussing how this general mechanistic picture is specifically applicable to the response regimes observed in semiflexible biopolymer networks, and comment on the role of coordination number heterogeneities.

4.2.1 Kinetic Model

Consider a disordered network of N nodes connected by harmonic springs with an average coordination number z. A network in d dimensions will have Nd degrees of freedom (ignoring rigid body rotations and translations) which are constrained by $Nz/2$ springs. If $z > z_c = 2d$ the constraints will outnumber the degrees of freedom and the network will be macroscopically rigid; conversely a floppy network with a vanishing shear modulus is expected for $z < z_c$. If $z = z_c$ the network is on the verge of rigidity and is said to be isostatic. Herein we quantify the degree of connectivity by $\delta z \equiv z_c - z$.

We start with an under constrained ($\delta z > 0$) network that is divided into a set of mesoscopic blocks of size a which carry scalar strain γ with time dependent probability $P_i(\gamma, t)$. The probability distribution is assumed to evolve dynamically via a master equation arising from a simple mechanistic picture: (1) deformation from an applied stress and (2) non-local strain propagation.

For small strains the blocks are expected to be fluid-like due to the presence of "soft modes" [WSN05, WLK08, Tig12], defined as deformations which cost

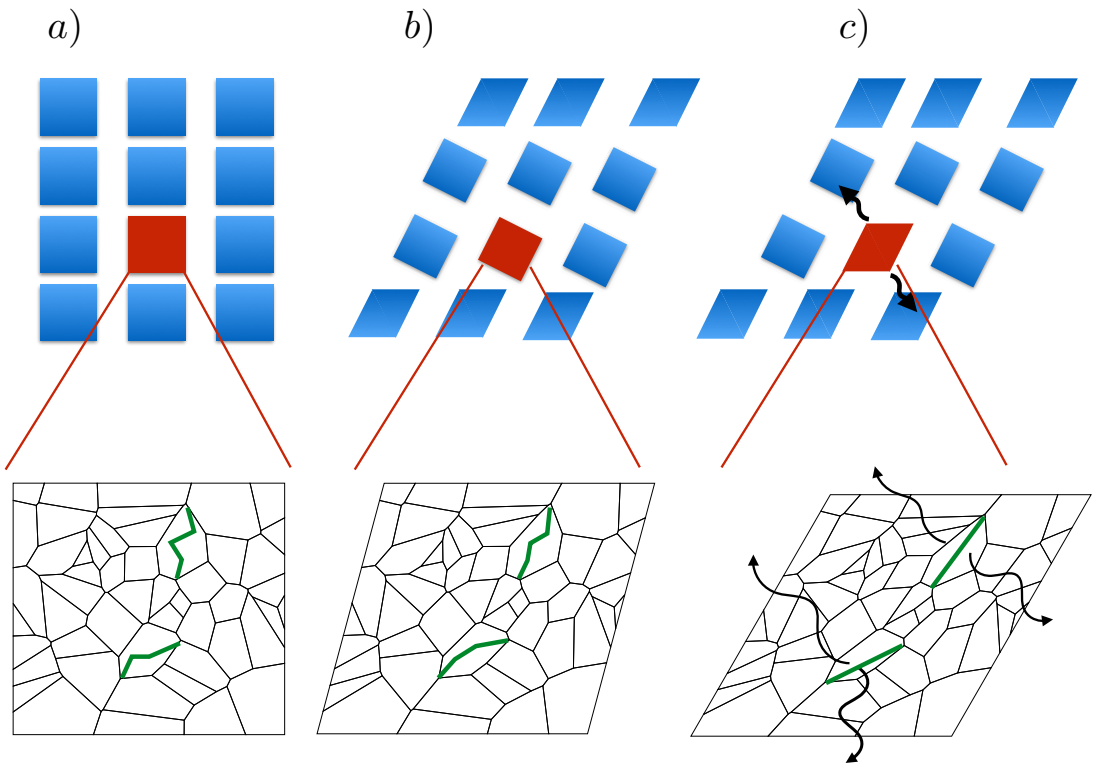

Figure 4.7: Schematic of filamentous network that is globally under constrained. The network is divided into mesoscopic "blocks", and a nearly isostatic network under no external stress has regions that are locally under constrained (a). When the whole network is subjected to a local stress σ, under constrained areas are free to deform without any stress response. This is displayed schematically by rotation (or non-affine deformation) of the blocks (b). At a critical strain γ_c, however, the fully stretched regions now must propagate strain throughout the system in order to maintain stress equilibrium (c).

zero (or anomalously low) energy. A uniformly applied stress σ_0 will lead to a constant accumulation of strain in the block $\sigma_0 t/\eta$, where η is the viscosity of the block. In the master equation this process takes the form of an advective term $-\frac{\sigma_0}{\eta}\partial_\gamma P_i(\gamma,t)$.

Soft modes are only present over a finite range of strain before they are "stretched out" of the material (as illustrated schematically in Fig. 4.7), suggesting that the strain accumulation will proceed only to a critical strain γ_c. This critical strain will depend on the coordination deficit δz, since a vastly underconstrained portion of the network will allow for larger free strain accumulation. Removing bonds from an isostatic network enables node displacement in direct proportion to the number of bonds removed, and thus we expect that the critical strain will scale as $\gamma_c \sim \delta z$. For $\gamma > \gamma_c$ blocks will accumulate stress which is relaxed by elastically propagating excess strain to other blocks in the network over a time scale τ. For simplicity it is assumed that local excess strain relaxes to zero and that the interactions with other blocks take the form of a Boltzmann collision operator $\mathcal{L}(\{P_i\})$.

Collectively these mechanisms describe the following master equation

$$\begin{aligned}\partial_t P_i(\gamma,t) &= -\frac{\sigma_0}{\eta}\partial_\gamma P_i(\gamma,t) - \frac{\Theta(|\gamma|-\gamma_c)}{\tau}P_i(\gamma,t) \\ &+ \rho_i(t)\delta(\gamma) + \mathcal{L}(\{P_i\}),\end{aligned} \tag{4.68}$$

where we define

$$\rho_i = \int \mathrm{d}\gamma' \, \frac{\Theta(|\gamma'|-\gamma_c)}{\tau} P_i(\gamma',t) \tag{4.69}$$

as the *rate of elastic events* associated with elastic strain redistribution in the network. These elastic events are catalysts for the anomalous mechanical response displayed by the system, and physically correspond to soft modes freezing out under local strain. Once the soft modes have been eliminated, the strain must propagate elastically throughout the network. The operator $\mathcal{L}(\{P_i\})$ gives the

change in local probability due to elastic events in other blocks

$$\begin{aligned}\mathcal{L}(\{P_i\}) &= \sum_{j\neq i}\int \mathrm{d}\gamma' \,\frac{\Theta(|\gamma'|-\gamma_c)}{\tau}\,[P_j(\gamma',t)P_i(\gamma+\delta\gamma_i,t) \\ &- P_j(\gamma',t)P_i(\gamma,t)]\,, \end{aligned} \tag{4.70}$$

where the change in strain in block i may be written as $\delta\gamma_i = \Pi_{i,j}\delta\gamma_j$, with $\Pi_{i,j}$ the strain propagator between blocks. One may calculate a general propagator in the continuum limit by dividing the tensorial strain into affine and non-affine components $\mathbf{m}\varepsilon = \mathbf{m}\varepsilon^A + \mathbf{m}\varepsilon^{NA}$. Treating the non-affine component as a perturbation, a background elastic medium will develop a shear stress $\mathbf{m}\sigma = 2\mu\mathbf{m}\varepsilon^A$. Applying stress balance, $\nabla\cdot\mathbf{m}\sigma = 0$, one can show that the non-affine strain component acts as a quadrupolar source that propagates the strain [Esh59, PAL04]; in our scalar model this non-affine source corresponds to the density of elastic events.

In order to make analytical progress it is necessary to simplify the nonlinear collision operator by assuming small $\delta\gamma$ and furthermore full strain relaxation between the blocks $\delta\gamma \approx \gamma_c$. These assumptions are expected to be valid near the rigidity transition when $\delta z \ll 1$ and floppy modes stiffen quickly under small applied stress. One may now perform a Kramers-Moyal [Ris89] expansion where the collision operator is evaluated as a Taylor series in $\delta\gamma$. We truncate the expansion at second order and derive the corresponding Fokker-Planck equation

$$\begin{aligned}\partial_t P_i(\gamma,t) &= -\frac{\sigma}{\eta}\partial_\gamma P_i(\gamma,t) - \frac{\Theta(|\gamma|-\gamma_c)}{\tau}P_i(\gamma,t) \\ &+ \rho_i(t)\delta(\gamma) + D_i(t)\partial_\gamma^2 P_i(\gamma,t). \end{aligned} \tag{4.71}$$

The stress is modified by the elastic events, $\sigma = \sigma_0 + \frac{\eta}{2}\sum_{j\neq i}\Pi_{i,j}\gamma_c\rho_j(t)$. The expansion introduces a strain diffusion term with a *non local* diffusion coefficient D proportional to the rate of elastic events in other blocks

$$D_i(t) = \frac{1}{2}\sum_{j\neq i}\Pi_{i,j}^2\gamma_c^2\rho_j(t). \tag{4.72}$$

The existence of strain diffusion in the system is the primary physical phenomenon responsible for critical rigidity and spatial cooperativity.

The block description is easily coarse grained into a continuous field representation in which the discrete label i is replaced by position vector $\mathbf{r}$. The strain diffusion coefficient can be written as

$$D(\mathbf{r},t) = \alpha\rho(\mathbf{r},t) + m\nabla^2\rho(\mathbf{r},t), \tag{4.73}$$

where $\alpha = \frac{1}{2}\gamma_c^2 \sum_{j\neq i} \Pi_{i,j}^2$ is a coupling constant and $m = \frac{1}{4}a^2\gamma_c^2 \sum_{j\neq i} \Pi_{i,j}^2$ quantifies the degree of heterogeneity in the system. The aforementioned scaling $\gamma_c \sim \delta z$ suggests m and α both scale as δz^2. Before solving the equations we introduce rescaled variables $\tilde{\gamma} = \gamma/\gamma_c, \tilde{\sigma} = \sigma\tau/\eta\gamma_c, \tilde{D} = D\tau/\gamma_c^2, \tilde{\rho} = \rho\tau, \tilde{\mathbf{r}} = \mathbf{r}/a, \tilde{t} = t/\tau, \tilde{m} = m/a^2\gamma_c^2, \tilde{\alpha} = \alpha/\gamma_c^2$, and drop the tildes for clarity.

4.2.2 Homogeneous systems and the rigidity transition in amorphous solids

Steady state solutions to the Fokker-Planck equation, Eq. 4.71, are first found in the limit $\sigma = 0$. For a homogeneous system $m = 0$ and the rate of elastic events is simply proportional to the diffusion coefficient, $\rho = D/\alpha$. Requiring $P(\mathbf{r},\gamma,t)$ to be normalized is equivalent to enforcing

$$D = \frac{2\alpha D}{1 + 2\sqrt{D} + 2D}. \tag{4.74}$$

If $\alpha < \frac{1}{4}$ the only solution is $D = 0$, representing a steady state with no elastic events that behaves macroscopically as a fluid. Two new solutions appear at $\alpha = \frac{1}{4}$ with finite $D(\alpha = \frac{1}{4}) = \frac{1}{4}$ which are elastic states with continuous strain redistribution. For homogeneous systems near the isostatic point one expects a continuous transition between response regimes, as observed in the static coordination controlled transition [SV10, LN10], and these solutions are therefore not immediately accessible. In fact, only one of the new solutions is smoothly connected to $D = 0$, intersecting the fluid like solution at the critical value $\alpha_c = \frac{1}{2}$ where it grows as $D \sim (\alpha - \alpha_c)^2$. In the absence of applied stress the model thus

has two distinct states, fluid and elastic, controlled by the coupling parameter α with crossover between regimes at α_c.

The equations may still be solved in the presence of applied stress, although they simplify considerably in the limit $\sigma \ll 1$. We choose the rate of elastic events $\rho(\mathbf{r})$ and the averaged local strain $\bar{\gamma}(\mathbf{r}) = \int \mathrm{d}\gamma' P(\mathbf{r}, \gamma')$ as the relevant variables and focus on the soft network $\alpha < \alpha_c$. Steady state solutions are found by expanding $\bar{\gamma}$ and ρ in series expansions for small stress, from which we find $\bar{\gamma} = (6\rho)^{-1}\sigma$. An important result is the existence of a non vanishing $\gamma^* \equiv \lim_{\sigma\to 0} \bar{\gamma} = (12\alpha)^{-1/2}(\alpha_c - \alpha)^{1/2}$ that is identified with a rigidifying strain capturing the intuitive idea that the network must remove soft modes before becoming macroscopically stiff. Below the critical point $\gamma^* \sim (\alpha_c - \alpha)^{1/2}$ while above $\gamma^* \sim (\alpha - \alpha_c)^{-2}$. Continuing to the next order in σ we find

$$\bar{\gamma} = \gamma^* + \sqrt{\frac{\gamma^*}{3}}\sqrt{\sigma} + \mathcal{O}(\sigma), \tag{4.75}$$

This predicts a stress-strain relationship that is the primary result of this Letter

$$\sigma = \begin{cases} \frac{3(\bar{\gamma}-\gamma^*)^2}{\gamma^*} & ;\bar{\gamma} \geq \gamma^* \\ 0 & ;\bar{\gamma} \leq \gamma^*. \end{cases} \tag{4.76}$$

Under-constrained systems are predicted to rigidify at a critical strain γ^* into nonlinear elastic materials, as shown in Fig. 4.8. Networks with $\bar{\gamma} < \gamma^*$ are macroscopically soft because of the degenerate set of stress-free configurations associated with local soft modes. The degeneracy is broken as strain is increased and the network acquires a distinctive non linear elastic response $\sigma \sim \gamma^2$ that the model suggests is due to elastic strain propagation within system. In the context of critical phenomena the applied strain acts as a dynamic order parameter whose value, in conjunction with the coordination, is necessary to specify the mechanical response regime of amorphous solids near the isostatic point.

The stress-strain relation Eq. 4.76 is seen numerically in simulations of under-constrained random spring networks near the isostatic point [WLK08], where the

authors observe networks which rigidify as $\sigma \sim \gamma^2$ at a connectivity dependent critical strain $\gamma^* \sim \delta z$. Our kinetic theory connects the macroscopic rigidifying strain γ^* to a microscopic model parameter γ_c and we are thus able to reproduce this latter scaling. Specifically, we argued that γ_c necessarily scales as δz and furthermore $\gamma^* \sim \gamma_c$ so that $\gamma^* \sim \delta z$, as seen in the simulations.

Experimental realizations of the rigidity transition are found in semiflexible polymer networks. Although the networks are generally under constrained in the Maxwell sense they are not truly soft because of either thermal or active fluctuation induced stiffening [DSS13, BM11]. Nevertheless, soft modes are still present in the form of anomalously soft bending excitations of individual filaments [HLM03, BML11]. The bending modes are stretched out under applied strain in a similar fashion to the spring networks (see Fig. 4.7) and become locally stiff as the stretching regime of the polymers is probed. Network connectivity is thus more difficult to define, although the average free contour length of the filaments serves as a reasonable proxy. Despite the differences, Eq. 4.76 accurately models the strain-stiffening transition seen in experiments [WBW07, KWJ09], suggesting that the proposed kinetic theory generically describes stiffening transitions corresponding to excitations of modes with vastly different energy scales.

4.2.3 Correspondence with yield stress fluids

We note that upon taking $\gamma \leftrightarrow \sigma$ and $\sigma_0 \leftrightarrow \dot{\gamma}_0$ in Eq. 4.68 our model is identical to kinetic theories for elasto-plastic flow proposed to describe the jamming transition in emulsions [HL98, BCA09]. The origin of this correspondence lies in how network connectivity generates non-affine or plastic deformations in a material. Jammed emulsions flow when local plastic events collaboratively fluidize the system, while for floppy networks the characteristic inelastic deformation is the non-affine strain (see Fig. 4.8). This non-affine deformation, caused by the pulling out of soft modes, locally changes the equilibrium reference state of the network,

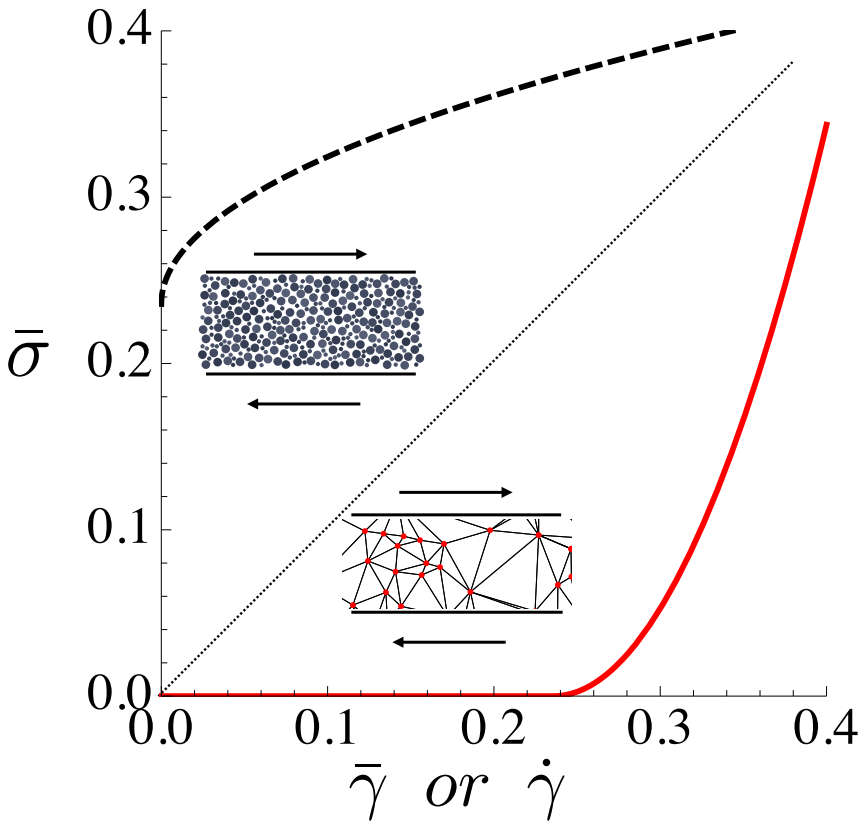

Figure 4.8: Red curve: An under constrained network displays fluid-like behavior for small strains, but the system rigidifies above the critical strain γ^*. The continuous transition from fluid-like to elastic behavior is seen in experiments and simulations, and the scaling arguments we derive here correspond to the numerical results of [WLK08]. Black curve: Comparison of the stress-strain relations for the kinetic theory for soft glassy flows [BCA09] and the kinetic theory for isostatic spring networks presented here. Jammed emulsions must build up a finite yield stress before the flowing state is achieved. In this case, the initial static response is elastic, since the material is jammed, but in the presence of an applied dynamic external stimulus the system displays fluid behavior. This correspondence arises from the intrinsic dependence on the underlying contact network that these disparate systems share.

and thus mediates a geometrically controlled nonlinear elastic response at high strain. In jammed emulsions, microscopic stresses build up and dynamically relax through plastic events, until the whole system yields and flows; in floppy networks, strain accumulates and then dynamically relaxes through non-affine elastic events, and the whole system rigidifies.

4.2.4 Non-universal behavior of inhomogeneous systems

Motivated by this correspondence, we note that in yield stress fluids, heterogeneity leads to a spatial cooperativity length scale that prevents a universal collapse of the constitutive relations [HML03, LAM14]. We now examine the case of floppy networks where $m \neq 0$. Since m is a measurement of the nearest neighbor strain propagator, the spatial fluctuations in δz are an appropriate measure of the heterogeneity. In other words, when the correlation length associated with the spatial variance of the coordination is on the order of the system size, the universal curve in Fig. 4.8 is expected to break down. Relaxing the $m = 0$ condition, eliminating the shear rate, and expanding the rate of elastic events around γ^* we find the self consistency equation

$$m\nabla^2\rho = a_1\gamma^*(\gamma^* - \bar{\gamma})\rho + a_2\rho^{3/2} + \mathcal{O}(\rho^2), \tag{4.77}$$

where $a_1 = 48\alpha^2$ and $a_2 = 4\alpha^{3/2}(1-\alpha)$ and we have used Eq. 4.73 to eliminate the diffusion coefficient. For a homogeneous system the left hand side of Eq. 4.77 vanishes and we immediately find the bulk density of elastic events

$$\rho_b = \left(\frac{a_1\gamma^*}{a_2}\right)^2 (\bar{\gamma} - \gamma^*)^2. \tag{4.78}$$

Expanding ρ around ρ_b one finds

$$\nabla^2\rho = \frac{1}{\xi^2(\bar{\gamma})}(\rho - \rho_b), \tag{4.79}$$

where we have introduced the rigidity correlation length

$$\xi(\bar{\gamma}) = \sqrt{\frac{m}{a_1(\bar{\gamma} - \gamma^*)}}. \tag{4.80}$$

In many simulations of amorphous solids, special care is taken to ensure that the spatial fluctuations of the coordination are small; this prevents percolation effects that may obscure careful observation of the properties of the transition point. However, biopolymer networks are complicated, often very heterogeneous networks. Inhomogeneities on a length scale $\sim \xi$ will prevent a universal scaling collapse onto the curve described by Eq. 4.77. Instead, there will be spatially extended regions of strain diffusion, and thus the effective exponent of the shear modulus will be non-universal. A macroscopic measurement of nonlinear elasticity that corresponds to the distribution of biopolymer microstructure is a key component of building an understanding of these systems.

4.2.5 Conclusion

Motivated by successful theories describing the dynamic unjamming transition in emulsions we propose a simple kinetic theory which predicts the onset of a non-percolative rigidity transition in under constrained elastic networks subject to external stress. The main result is a nonlinear stress-strain relationship $\sigma \sim (\gamma - \gamma^*)^2$ which recovers numerical predictions and is consistent with experimental observations of biopolymer networks. More generally, the model serves to extend the known static correspondence between jamming and the isostatic transition to systems out of mechanical equilibrium, and suggests that heterogeneous networks should display non-universal rigidity transitions. Due to the presence of a rigidity correlation length, universal scaling breaks down and the microstructure of the network needs to be modeled to accurately predict the emergent modulus. Finally, we note that ρ can be thought of as an order parameter that comes from minimizing a dynamic free energy, and thus creates an effective thermodynamic field theory for these out-of-equilibrium systems. This framework supports adding more complicated mechanisms into the theory, as well as accommodating thermal fluctuations or the active noise that is prevalent in biopolymer systems.

References

[ABD92] A. Ajdari, B. Duplantier, D. Hone, L. Peliti, and J. Prost. “”Pseudo-Casimir” effect in liquid crystals.” *J. Phys. II France*, **2**(3):487–501, 1992.

[AJL02] Bruce Alberts, Alexander Johnson, Julian Lewis, Martin Raff, Keith Roberts, and Peter Walter. *Molecular biology of the cell*. Garland Science, 2002.

[BCA09] Lydéric Bocquet, Annie Colin, and Armand Ajdari. “Kinetic theory of plastic flow in soft glassy materials.” *Physical review letters*, **103**(3):036001, 2009.

[BGP94] R. Bruinsma, M. Goulian, and P. Pincus. “Self-assembly of membrane junctions.” *Biophysical Journal*, **67**(2):746 – 750, 1994.

[BM11] CP Broedersz and FC MacKintosh. “Molecular motors stiffen non-affine semiflexible polymer networks.” *Soft Matter*, **7**(7):3186–3191, 2011.

[BML11] Chase P. Broedersz, Xiaoming Mao, Tom C. Lubensky, and Frederick C. MacKintosh. “Criticality and isostaticity in fibre networks.” *Nat Phys*, **7**(12):983–988, 12 2011.

[10.1038/nphys2127.]

[BMS94] C. Bustamante, J.F. Marko, E. D. Siggia, and S. Smith. “Entropic Elasticity of lambda-phage DNA.” *Science*, **265**:1599–1600, 1994.

[CAO09] C. J. Cyron, M. Arroyo, and M. Ortiz. “Smooth, second order, non-negative meshfree approximants selected by maximum entropy.” *International Journal for Numerical Methods in Engineering*, **79**(13):1605–1632, 2009.

[Cas48] H. B. G. Casimir. “On the attraction between two perfectly conducting plates.” *Proc. K. Ned. Adad. Wet.*, **51**:793, 1948.

[CMB13] C. J. Cyron, K. W. Müller, A. R. Bausch, and W. A. Wall. “Micromechanical simulations of biopolymer networks with finite elements.” *Journal of Computational Physics*, **244**:263–251, 2013.

[CMS13] C. J. Cyron, K. W. Müller, K. M. Schmoller, A. R. Bausch, W. A. Wall, and R. F. Bruinsma. “Equilibrium Phase Diagram of semiflexible polymer networks with linkers.” *EPL (Europhysics Letters)*, **102**:38003, 2013.

[CNG10] Christian Cyron, Keijo Nissen, Volker Gravemeier, and Wolfgang Wall. "Stable meshfree methods in fluid mechanics based on Green's functions." *Computational Mechanics*, **46**:287 – 300, 2010.

[Cri03] M. A. Crisfield. *Non-linear Finite Element Analysis of Solids and Structures, Volume 2: Advanced Topics*. Wiley, Chichester, 2003.

[DE86] M. Doi and S.F. Edwards. *The Theory of Polymer Dynamics*. Clarendon Press, Oxford, 1986.

[DLP61] I. E. Dzyaloshinskii, E. M. Lifshitz, and L. P. Pitaevskii. "Reviews of Topical Problems: General Theory of Van Der Waals' Forces." *Soviet Physics Uspekhi*, **4**:153–176, February 1961.

[DML07] Moumita Das, FC MacKintosh, and Alex J Levine. "Effective medium theory of semiflexible filamentous networks." *Physical review letters*, **99**(3):038101, 2007.

[DS93] E. D'Hoker and P. Sikivie. "Casimir forces between beads on strings." *Phys. Rev. Lett.*, **71**:1136–1139, 1993.

[DSS13] M. Dennison, M. Sheinman, C. Storm, and F. C. MacKintosh. "Fluctuation-Stabilized Marginal Networks and Anomalous Entropic Elasticity." *Phys. Rev. Lett.*, **111**:095503, Aug 2013.

[Dur95] DJ Durian. "Foam mechanics at the bubble scale." *Physical review letters*, **75**(26):4780, 1995.

[Esh59] JD Eshelby. "The elastic field outside an ellipsoidal inclusion." *Proceedings of the Royal Society of London. Series A, Mathematical and Physical Sciences*, pp. 561–569, 1959.

[FH65] R. P. Feynman and A. R. Hibbs. *Quantum Mechanics and Path Integrals*. McGraw–Hill, 1965.

[GCB10] Julie Goyon, Annie Colin, and Lydéric Bocquet. "How does a soft glassy material flow: finite size effects, non local rheology, and flow cooperativity." *Soft Matter*, **6**(12):2668–2678, 2010.

[GCO08] J Goyon, A Colin, G Ovarlez, A Ajdari, and L Bocquet. "Spatial cooperativity in soft glassy flows." *Nature*, **454**(7200):84–87, 2008.

[GR94] I. S. Gradshtein and I. M. Ryzhik. *Table of Integrals, Series, and Products*. Academic Press, 1994.

[GSM04] ML Gardel, JH Shin, FC MacKintosh, L Mahadevan, P Matsudaira, and DA Weitz. "Elastic behavior of cross-linked and bundled actin networks." *Science*, **304**(5675):1301–1305, 2004.

[HH77] P. C. Hohenberg and B. I. Halperin. "Theory of dynamic critical phenomena." *Rev. Mod. Phys.*, **49**:435–479, Jul 1977.

[HL98] Pascal Hébraud and François Lequeux. "Mode-coupling theory for the pasty rheology of soft glassy materials." *Physical Review Letters*, **81**(14):2934, 1998.

[HLM03] DA Head, AJ Levine, and FC MacKintosh. "Distinct regimes of elastic response and deformation modes of cross-linked cytoskeletal and semiflexible polymer networks." *Physical Review E*, **68**(6):061907, 2003.

[HML03] David A Head, FC MacKintosh, and Alex J Levine. "Nonuniversality of elastic exponents in random bond-bending networks." *Physical Review E*, **68**(2):025101, 2003.

[Hov50] L. van Hove. *Physica*, **16**(137), 1950.

[HVO07] EM Huisman, T Van Dillen, PR Onck, and E Van der Giessen. "Three-dimensional cross-linked F-actin networks: relation between network architecture and mechanical behavior." *Physical review letters*, **99**(20):208103, 2007.

[JC99] G. Jelenic and M. A. Crisfield. "Geometrically exact 3D beam theory: implementation of a strain-invariant finite element for statics and dynamics." *Computer Methods in Applied Mechanics and Engineering*, **171**(1-2):141–171, 1999.

[Kar07] Mehran Kardar. *Statistical physics of particles*. Cambridge University Press, 2007.

[KDN09] Gijsje H. Koenderink, Zvonimir Dogic, Fumihiko Nakamura, Poul M. Bendix, Frederick C. MacKintosh, John H. Hartwig, Thomas P. Stossel, and David A. Weitz. "An active biopolymer network controlled by molecular motors." *Proceedings of the National Academy of Sciences*, **106**(36):15192–15197, 2009.

[KG99] Mehran Kardar and Ramin Golestanian. "The "friction" of vacuum, and other fluctuation-induced forces." *Rev. Mod. Phys.*, **71**:1233–1245, 1999.

[Kit58] C. Kittel. *Elementary Statistical Physics*. Wiley, 1958.

[Kle86] H. Kleinert. "Path integral for second-derivative Lagrangian." *Journal of Mathematical Physics*, **27**(12):3003–3013, 1986.

[Kle10] H. Kleinert. *Path Integrals in Quantum Mechanics, Statistics, Polymer Physics, and Financial Markets*. World Scientific, 2010.

[Kre94] M. Krech. *The Casimir Effect in Critical Systems.* World Scientific, 1994.

[KWJ09] Hyeran Kang, Qi Wen, Paul A Janmey, Jay X Tang, Enrico Conti, and Fred C MacKintosh. "Nonlinear elasticity of stiff filament networks: Strain stiffening, negative normal stress, and filament alignment in fibrin gels?" *The Journal of Physical Chemistry B*, **113**(12):3799–3805, 2009.

[LAM14] Antoine Le Bouil, Axelle Amon, Sean McNamara, and Jérôme Crassous. "Emergence of Cooperativity in Plasticity of Soft Glassy Materials." *Physical review letters*, **112**(24):246001, 2014.

[Lan18] Irving Langmuir. "The Adsorption Of Gases On Plane Surfaces Of Glass, Mica And Platinum." *J. Am. Chem. Soc.*, **40**(9):1361–1403, 1918.

[LCB10] Oliver Lieleg, Mireille MAE Claessens, and Andreas R Bausch. "Structure and dynamics of cross-linked actin networks." *Soft Matter*, **6**(2):218–225, 2010.

[LCH07] O. Lieleg, M. M. A. E. Claessens, C. Heussinger, E. Frey, and A. R. Bausch. "Mechanics of Bundled Semiflexible Polymer Networks." *Phys. Rev. Lett.*, **99**:088102, Aug 2007.

[LL86] L.D. Landau and E.M. Lifshitz. *Theory of Elasticity.* Pergamon Press, 1986.

[LM66] Elliott H Lieb and Daniel Charles Mattis. *Mathematical Physics in One Dimension: Exactly Soluble Models of Interacting Particles, a Collection of Reprints with Introductory Text, by Elliott H. Lieb [and] Daniel C. Mattis.* Academic Press, 1966.

[LN10] Andrea J Liu and Sidney R Nagel. "The jamming transition and the marginally jammed solid." *Annu. Rev. Condens. Matter Phys.*, **1**(1):347–369, 2010.

[Max64] J. C. Maxwell. *Philos. Mag*, **27**(294), 1864.

[MCC11] Vincent Mansard, Annie Colin, Pinaki Chauduri, and Lyderic Bocquet. "A kinetic elasto-plastic model exhibiting viscosity bifurcation in soft glassy materials." *Soft Matter*, **7**(12):5524–5527, 2011.

[MKJ95] FC MacKintosh, J Käs, and PA Janmey. "Elasticity of semiflexible biopolymer networks." *Physical review letters*, **75**(24):4425, 1995.

[MT97] Vladimir Mostepanenko and N. N. Trunov. *The Casimir Effect and Its Applications.* Oxford University Press, 1997.

[MWB14] K. W. Müller, W. A. Wall, R. J. Bruinsma, and Alex J. Levine. "Universal rheology of semiflexible bundle networks.", 2014. Submitted.

[OSL03] Corey S O?Hern, Leonardo E Silbert, Andrea J Liu, and Sidney R Nagel. "Jamming at zero temperature and zero applied stress: The epitome of disorder." *Physical Review E*, **68**(1):011306, 2003.

[PAL04] Guillemette Picard, Armand Ajdari, François Lequeux, and Lydéric Bocquet. "Elastic consequences of a single plastic event: A step towards the microscopic modeling of the flow of yield stress fluids." *The European Physical Journal E: Soft Matter and Biological Physics*, **15**(4):371–381, 2004.

[PHT14] Robyn H Pritchard, Yan Yan Shery Huang, and Eugene M Terentjev. "Mechanics of biological networks: from the cell cytoskeleton to connective tissue." *Soft matter*, **10**(12):1864–1884, 2014.

[PPH03] O. Pelletier, E. Pokidysheva, L. S. Hirst, N. Bouxsein, Y. Li, and C. R. Safinya. "Structure of Actin Cross-Linked with α-Actinin: A Network of Bundles." *Phys. Rev. Lett.*, **91**:148102, Sep 2003.

[RC03] M. Rubenstein and R.H. Colby. *Polymer Physics*. Clarendon Press, Oxford, 2003.

[Ris89] H. Risken. *The Fokker-Planck Equation*. Springer-Verlag, Berlin, 2nd edition, 1989.

[Rom04] I. Romero. "The interpolation of rotations and its application to finite element models of geometrically exact rods." *Computational Mechanics*, **34**(2):121–133, 2004.

[SDB09] Homin Shin, Kirstin R. Purdy Drew, James R. Bartles, Gerard C. L. Wong, and Gregory M. Grason. "Cooperativity and Frustration in Protein-Mediated Parallel Actin Bundles." *Phys. Rev. Lett.*, **103**:238102, Nov 2009.

[SLB09] K.M. Schmoller, O. Lieleg, and A.R. Bausch. "Structural and Viscoelastic Properties of Actin/Filamin Networks: Cross-Linked versus Bundled Networks." *Biophys. J.*, **97**(1):83 – 89, 2009.

[SLH97] Peter Sollich, François Lequeux, Pascal Hébraud, and Michael E Cates. "Rheology of soft glassy materials." *Physical review letters*, **78**(10):2020, 1997.

[Sol98] Peter Sollich. "Rheological constitutive equation for a model of soft glassy materials." *Physical Review E*, **58**(1):738, 1998.

[SV10] Alexander ON Siemens and Martin Van Hecke. "Jamming: A simple introduction." *Physica A: Statistical Mechanics and its Applications*, **389**(20):4255–4264, 2010.

[SZK53] Zevi W. Salsburg, Robert W. Zwanzig, and John G. Kirkwood. "Molecular Distribution Functions in a OneDimensional Fluid." *The Journal of Chemical Physics*, **21**(6):1098–1107, 1953.

[Tig12] Brian P Tighe. "Dynamic critical response in damped random spring networks." *Physical review letters*, **109**(16):168303, 2012.

[Ton36] Lewi Tonks. "The Complete Equation of State of One, Two and Three-Dimensional Gases of Hard Elastic Spheres." *Phys. Rev.*, **50**:955–963, Nov 1936.

[WBJ12] Qi Wen, Anindita Basu, Paul A Janmey, and Arjun G Yodh. "Non-affine deformations in polymer hydrogels." *Soft matter*, **8**(31):8039–8049, 2012.

[WBW07] Qi Wen, Anindita Basu, Jessamine P Winer, Arjun Yodh, and Paul A Janmey. "Local and global deformations in a strain-stiffening fibrin gel." *New Journal of Physics*, **9**(11):428, 2007.

[Wei89] Steven Weinberg. "The cosmological constant problem." *Rev. Mod. Phys.*, **61**:1–23, 1989.

[WLK08] M Wyart, H Liang, A Kabla, and L Mahadevan. "Elasticity of floppy and stiff random networks." *Physical review letters*, **101**(21):215501, 2008.

[WSN05] Matthieu Wyart, Leonardo E Silbert, Sidney R Nagel, and Thomas A Witten. "Effects of compression on the vibrational modes of marginally jammed solids." *Physical Review E*, **72**(5):051306, 2005.

[WTH06] B. Wagner, R. Tharmann, I. Haase, M. Fischer, and A. R. Bausch. "Cytoskeletal polymer networks: The molecular structure of cross-linkers determines macroscopic properties." *Proc. Natl. Acad. Sci.*, **103**(38):13974–13978, 2006.

[ZPZ98] P. Ziherl, R. Podgornik, and S. Zumer. "Casimir force in liquid crystals close to the nematic–isotropic phase transition." *Chemical Physics Letters*, **295**(1-2):99 – 104, 1998.